Tampere University

JAN VILJANEN

Online Laser Diagnostics for High-Temperature Chemistry in Biomass Combustion

Tampere University Dissertations 42

Tampere University Dissertations 42

JAN VILJANEN

Online Laser Diagnostics for High-Temperature Chemistry in Biomass Combustion

ACADEMIC DISSERTATION
To be presented, with the permission of
the Faculty of Engineering and Natural Sciences
of Tampere University,
for public discussion in the auditorium S3
of the Sähkötalo, Korkeakoulunkatu 3, Tampere,
on 29 March 2019, at 12 o'clock.

ACADEMIC DISSERTATION
Tampere University, Faculty of Engineering and Natural Sciences
Finland

Responsible supervisor and Custos	Professor Juha Toivonen Tampere University Finland	
Pre-examiner(s)	Assistant Professor Florian Schmidt Umeå University Sweden	Chemist Research Scientist George Chan Lawrence Berkeley National Laboratory United States of America
Opponent(s)	Senior Lecturer Zhongshan Li Lund University Sweden	

The originality of this thesis has been checked using the Turnitin Originality Check service.

Cover design: Roihu Inc.

ISBN 978-952-03-1021-9 (print)
ISBN 978-952-03-1022-6 (pdf)
ISSN 2489-9860 (print)
ISSN 2490-0028 (pdf)
http://urn.fi/URN:ISBN:978-952-03-1022-6

PunaMusta Oy – Yliopistopaino
Tampere 2019

ABSTRACT

Increasing concern over environment and new energy policies are driving the thermal heat and power industry towards new CO_2 neutral fuels, such as biomass, and novel combustion schemes. Therefore new operational control and monitoring concepts are required to provide information of the combustion processes. Alkali elements and compounds have been identified to be one of the greatest challenges associated with thermal conversion of biomass as they cause severe operational problems in power plant boilers. In this Thesis, a new method to monitor temperature and O_2 concentration during thermal conversion of biomass is developed. Collinear Photofragmentation and Atomic Absorption Spectroscopy (CPFAAS) is utilized to measure potassium reaction kinetics in lean combustion conditions, which provides valuable information for high temperature reaction models and simulations. The new information on potassium reaction kinetics with O_2 enables online monitoring of temperature and O_2 concentration utilizing the CPFAAS signal.

Microwave-Assisted Laser-Induced Breakdown Spectroscopy (MW-LIBS) is demonstrated for the first time at ambient atmospheric conditions with impressive 93-fold enhancement in limit of detection (LOD). MW-LIBS is further applied for online elemental monitoring during thermal conversion of biomass fuels as it improves detection of trace elements and reduces adverse self-absorption effects in high-concentration conditions. To enable the benefits of MW-LIBS, a novel burner for flame calibration is introduced. The burner allows calibration of LIBS for extended concentration range enabling quantitative elemental release monitoring during thermal conversion of different biomass fuels with varying elemental content. The elemental release behavior of biomass fuels is paramount for thermal conversion models and simulations that provide boiler operators and manufacturers crucial information on how to optimize the thermal processes and mitigate the alkali associated problems. Furthermore, as the novel MW-LIBS approach requires no or minimal sample preparation, it has great application potential for online elemental monitoring in different fields of science where low LOD or high sensitivity is required.

The novel CPFAAS and MW-LIBS approaches provide simple and versatile methods for online high-temperature chemistry monitoring from laboratory-scale systems up to full-scale power plant boilers. Laser diagnostics will play a significant role in optimization and in process control of future thermal power generation as it enables development of online sensor networks to monitor and forecast the plant behavior.

PREFACE

This work was carried out in the Laboratory of Photonics of the Tampere University of Technology during the years 2015-2019. I gratefully acknowledge the financial support from The Graduate School of Tampere University of Technology and all the partners in Clustering Innovation Competence of Future Fuels in Power Production (CLIFF).

I would like to thank Prof. Juha Toivonen for the guidance towards this Thesis and for the understanding and support for my travels. Without your provocation and inspiration, I would not have chosen to screw around in optics laboratory this long. I would also like to thank Prof. Zeyad Alwahabi for the opportunity to collaborate and visit the University of Adelaide twice over the years. I also acknowledge Dr. Tapio Sorvajärvi who paved the road for me to combustion diagnostics.

Through the years I have spent in the Optics Lab, I have had the privilege to meet the most amazing people and the list of names I am grateful to is too long to fit into this space. Special thanks goes to Dan and all the others in my Australian family. You made Adelaide another home for me. I have said this maybe a couple of times, Mikko and Kim, I am lucky to have friends I can be happy for, and I want to thank for all the moments that we have shared in and outside the lab.

Last but not least, I thank the most important supporters in my life: my sister and my parents. I find it quite weird how you support me no matter what I come up with, for example, moving to Tampere to study, going for a PhD, or throwing myself down a waterfall. I hope I will never find the limit.

Tampere, March 2019

Jan Viljanen

Rohkeus ei oo sitä ettei pelota,
vaan et uskaltaa hypätä vaik ei
tiedä selviikö elossa

Jare Henrik Tiihonen

CONTENTS

List of symbols and abbreviations

ppb	parts-per-billion
ppm	parts-per-million
ppt	parts-per-trillion
BFB	Bubbling Fluidized Bed
CARS	Coherent anti-Stokes Scattering
CFB	Circulating Fluidized Bed
CPFAAS	Collinear Photofragmentation and Atomic Absorption Spectroscopy
CRDS	Cavity Ring Down Spectroscopy
DIAL	Differential Absorption Lidar
DOAS	Differential Optical Absorption Spectroscopy
DWFM	Degenerate Four-Wave Mixing
DP-LIBS	Double Pulse Laser-Induced Breakdown Spectroscopy
EU	European Union
FA-LIBS	Flame Assisted Laser-Induced Breakdown Spectroscopy
FRS	Filtered Rayleigh Scattering
FTIR	Fourier-Transform Infrared Spectroscopy
FWHM	Full width at half maximum
HHV	Higher Heating Value
ICP	Inductively Coupled Plasma
IR	Infrared
LIBS	Laser-Induced Breakdown Spectroscopy
LOD	Limit of Detection
LTE	Local Thermal Equilibrium
MBMS	Molecular Beam Mass Spectrometry

MW	Microwave
MW-LIBS	Microwave-Assisted Laser-Induced Breakdown Spectroscopy
NFA	Near-Field Applicator
PA	Photoacoustics
PD	Photodetector
PEARLS	Plasma Excited Alkali Resonance
PF-LIF	Photofragmentation and Laser-Induced Fluorescence
PLIF	Planar Laser-Induced Fluorescence
PS	Polarization Spectroscopy
SD-LIBS	Spark Discharge Assisted Laser-Induced Breakdown Spectroscopy
SI	Surface Ionization
TDLAS	Tunable Diode Laser Absorption Spectroscopy
TG	Thermogravimetry
TP	Thermographic Phosphors
TUT	Tampere University of Technology
UV	Ultraviolet
WMS	Wavelength Modulation Spectroscopy
XRF	X-ray Fluorescence

A	Mass loss constant
A_f	Fragmenting laser beam cross section
A_{ul}	Transition probability
b	Slope of a curve
c	Speed of light
E	Energy
h	Planck's constant
J_k	Total angular momentum
k	Boltzman's constant
k_0	Wavenumber
k_i	Reaction rate
K_{eq}	Thermodynamic equilibrium constant
L	Interaction length
L_v	Latent heat of vaporization
m	Mass
M_a	Atomic or molecular mass
n_c	Critical electron density

n_e	Electron density
p	Ambient pressure
Q	Flow rate
R	Gas constant
s_{bi}	Background standard deviation
SC	Solution concentration
SR_a	Seeding rate
t	Time
T	Ambient temperature
v	Velocity
X	Concentration
$X_p$rec	Precursor molecule concentration

αL_{max}	Maximum absorbance due fragment atoms
αL_{max}	Residue absorbance due chemical equilibrium
γ	Fragmentation efficiency
γ_H	Full width at half maximum of absorption line
Δ	Plasma slab thickness
ΔG	Gibbs' free energy
ΔH	Enthalpy
ΔS	Entropy
$\Delta\lambda_S$	Full wavelength width at half maximum
$\Delta\tau$	Transition lifetime
$\Delta\tau_p$	Laser pulse width
$\Delta\nu_H$	Full frequency width at half maximum
$\Delta\nu_V$	Frequency shift
ε	Dielectric function
$\varkappa$	Thermal diffusivity of material
λ_f	Fragmentation wavelength
ϱ	Material density
σ	Absorption cross section
σ_G	Full width at half maximum of emission line
τ	Decay time
ν	Frequency
ω	Angular frequency

List of Publications

Paper I T. Sorvajärvi, J. Viljanen, J. Toivonen, P. Marshall, and P. Glarborg, "Rate Constant and Thermochemistry for K + O_2 + N_2 = KO_2 + N_2," J. Phys. Chem. A **119**, 3329-3336 (2015).

Paper II J. Viljanen, Z. Sun, and Z. T. Alwahabi, "Microwave Assisted Laser-Induced Breakdown Spectroscopy at Ambient Conditions," Spectrochim. Acta B **118**, 29-36 (2016)

Paper III J. Viljanen, T. Sorvajärvi, and J. Toivonen, "In Situ Laser Measurement of Oxygen Concentration and Flue Gas Temperature Utilizing Chemical Reaction Kinetics," Opt. Lett. **42**, 4925-4928 (2017)

Paper IV J. Viljanen, H. Zhao, Z. Zhang, J. Toivonen, and Z. T. Alwahabi, "Real-Time Release of Na, K and Ca During Thermal Conversion of Biomass Using Quantitative Microwave-Assisted Laser-Induced Breakdown Spectroscopy," Spectrochim. Acta B **149**, 76-83 (2018)

Author's Contribution

This Thesis is a compilation of four peer-reviewed publications. In following, the subjects and the key results of the publications are presented and the Author's contribution to the research is described.

Paper I Collinear Photofragmentation and Atomic Absorption Spectroscopy (CPFAAS) is demonstrated for chemical reaction kinetics analysis. The high temperature reaction rate constant for reaction between potassium and O_2 was presented and the equilibrium constant for KO_2 formation was defined. The Author was responsible for the major part of the experimental design and carried out most of the experiments. The Author also analyzed the obtained experimental data and provided the error estimation of the results. Dr. Tapio Sorvajärvi supervised the experimental work and was the main responsible of reporting. Prof. Peter Glarborg and Prof. Paul Marshall were the main responsibles of the analysis over physical chemistry. Prof. Juha Toivonen supervised the overall work and maintained the connections between collaborative partners.

Paper II Microwave-Assisted Laser-Induced Breakdown Spectroscopy (MW-LIBS) is demonstrated for the first time in ambient conditions for solid sample. Up to 93-fold improvement in detection limit of copper is achieved. The Author had full responsibility for the method development and carried out most of the experimental work and data analysis. The Author was also the main responsible on reporting composing most of the writing. Dr. Zhiwei Sun assisted in the experimental work and in data analysis. Dr. Sun also

supported with the reporting. Prof. Zeyad Alwahabi supervised the work providing feedback on experiments and reporting.

Paper III The potassium reaction kinetics is utilized for O_2 concentration and temperature monitoring during thermal conversion of a single fuel particle. Temporal O_2 concentration and temperature curves are presented with good agreement to reference values. The Author had full responsibility over the experimental method calibration and reporting. Dr. Tapio Sorvajärvi assisted with the theoretical derivation and in part of the experimental measurements. Prof. Juha Toivonen supervised the work providing feedback on experiments and reporting.

Paper IV MW-LIBS is applied for total elemental sodium, potassium, and calcium concentration monitoring during thermal conversion of a single biomass fuel particle in a burner flame. Novel burner seeding design is presented that allowed broad calibration range for MW-LIBS and temporal quantitative elemental release curves for sodium, potassium, and calcium from poplar samples are determined. The Author designed and carried out all optical experiments and had full responsibility for data analysis and reporting. Dr. Haibo Zhao assisted with the burner in the experiments and during reporting. Dr. Zhi-Hao Zhang was responsible for the design of the new burner. Prof. Juha Toivonen and Prof. Zeyad Alwahabi supervised the work providing feedback on experiments and reporting.

1

Introduction

The European Union (EU) has set an Energy Roadmap 2050 [1] that aims to reduce the greenhouse gas emissions by 80-95 % from 1990 levels by 2050. As energy sector is a major source of greenhouse gas emissions, this means great structural changes for power and heat industry. The amount of renewable energy sources, such as wind and solar power, will be increased significantly. However, thermal heat and power production will continue to be an essential part of power production chain to provide the base load to the grid and provide energy when renewable sources are not available. To create more efficient co-operation between renewable energy sources and combustion power plants, decentralization of the power system is required. To meet the altering grid demand, the combustion units are going to be smaller and they have to be more flexible to respond varying load. Simultaneously, the fuels used for heat and power production are required to be increasingly renewable and CO_2 neutral. Fuels that meet these requirements, such as biomass and municipal waste, have the potential to improve the sustainability and decrease the carbon footprint of thermal heat and power production. However, transition from fossil fuels to biomass is not straight forward as thermal conversion of biomass includes challenges that fossil fuels do not exhibit, such as alkali induced high-temperature corrosion. [2] Therefore, the old fossil fuel fired combustion power plants are not feasible for power production through thermal conversion of CO_2 neutral fuels but new technologies are required. [3] New grid requirements and increasing concern over environmental aspects set challenging operation environment for thermal heat and power production.

Biomass fuels possess substantial benefits compared with fossil fuels as environmental aspects are considered. Growth of biomass is based on photosynthesis occurring in plants and crops. Photosynthesis absorbs CO_2 from the atmosphere binding it to the structure of the biomass. Hence, as the CO_2 is released during the thermal conversion of biomass, it is not considered to contribute to the net CO_2 balance. Therefore biomass fuels are CO_2 neutral. [4] There are multiple sources of biomass that can be used as fuel for thermal heat and power production: wood chips, agricultural waste, algae, and industrial residues to mention a few. As biomass fuels are often side products of other processes, their price is low compared with fossil fuels. However, despite the low price and good global availability, transition from fossil fuels to biomass for thermal heat and power production is problematic. Biomass in general is a low grade fuel having low heating value and high content of moisture and ash-forming elements. A low heating value directly implies that the total energy released as heat during the thermal conversion of the fuel is low, which may lead to flame stability problems. Furthermore, ignition of the fuel is hindered due the moisture and ash content. In addition, the ash forming elements phosphorus (P), potassium (K), sodium (Na), and chlorine (Cl) are known to cause operational problems in power plant boilers, i.e. bed agglomeration, corrosion, slagging, and fouling, forcing the operators to frequent maintenance shutdowns and, in worst case scenario, to a forced unplanned shutdown due to occurance of a failure. To minimize the adverse effects arising from the fuel properties, the operators are forced to compromise in process conditions which lead to reduced process efficiency. [2]

New control measures and innovations in boiler design are required to improve the biomass combustion process and, furthermore, increase the attraction of biomass fuels for thermal heat and power production. This requires detailed knowledge of combustion process chemistry and of reaction pathways of the adverse compounds from fuel to ash. The high temperature and dynamic conditions in combustion processes set a challenge for analysis technologies. Optical spectroscopy studies the interaction between light and matter. In case the optical access is provided, using the light-matter interactions, i.e. absorption, scattering, and emission, a number of matter properties can be analyzed. Optical techniques are sensitive, selective and enable spatially localized, temporal measurements without physical sampling. These properties allow authentic non-intrusive online analysis of combustion chemistry providing information on the process conditions, molecular concentrations, and reaction dynamics. Optical methods have been utilized in

combustion diagnostics extensively and multiple techniques have been introduced for analysis of molecular concentrations and combustion conditions from laboratory to power plant scale. [5–7]

1.1 Aim and Scope of This Work

Work for this Thesis was partly carried out within a project on Clustering Innovation Competence of Future Fuels in Power Production (CLIFF) 2014-2017 as part of the activities of Tampere University of Technology (TUT). CLIFF consortium was funded by the National Technology Agency of Finland (TEKES) and number of international companies to be a common platform for universities and companies aiming for future innovations in utilization of biomass and waste derived fuels for power production. The aim of this Thesis was to develop novel laser-based methods for in-situ monitoring of chemical species and their reaction dynamics in high temperature conditions during thermal conversion of biomass fuels.

Alkali species are known to be one of the main causes of slagging, fouling, and high temperature corrosion in power plant boilers. The most problematic compound has been identified to be KCl that induces high corrosion rates on steel surfaces. [2] Hence, advancement in the understanding of the reaction dynamics and pathways of potassium transformation from the fuel to the ash is crucial for mitigation of operational problems caused by KCl. There exist number of methods to analyze the alkali content of fuel and ash but the challenge has been to identify the reaction mechanisms that define the molecular form of alkali species in gas phase and, eventually, in the ash deposits. Monitoring of potassium reaction dynamics in gas phase is premised on previously developed KCl monitoring technique named Photofragmentation and Atomic Absorption Spectroscopy (CPFAAS) [8]. It is capable to follow changes in potassium concentration after the photofragmentation event with high temporal resolution. This enables direct measurement of potassium reaction dynamics with the gas species in the ambient atmosphere. On the other hand, as behavior of potassium is known in certain environments, the chemical reaction kinetics can be utilized as indicator of reaction environment. Reaction dynamics of potassium has immense impact on boiler longevity and therefore affects to profitability of thermal power production. Most solid fuels contain potassium or other alkali metals, hence, the applications of potassium kinetics are not solely limited to biomass fuels that are infamous for

their high content of alkali metals and chlorine. Thorough understanding of chemical kinetics in combustion environment will aid the models and simulations to produce more accurate picture of the complete process. This enables the plant operators to optimize the process parameters to minimize the unwanted effects inside the boiler and, more importantly, to gain higher profitability. On the other hand, knowledge of elemental reaction parameters and paths during thermal power production provides crucial information for power plant designers and manufacturers on how to produce more sustainable and reliable boiler systems for demanding thermal power production scheme.

Journey of the adverse chemical compounds to boiler surfaces starts when they are released from the fuel. It is crucial to understand the elemental release behavior of different fuels to be able to distinguish the different reaction paths available in the gas phase for compounds to evolve. The feasibility of Laser-Induced Breakdown Spectroscopy (LIBS) technique has been studied for online monitoring of elemental release during thermal conversion of biomass samples. LIBS is a method of emission spectroscopy that can be applied on solid, liquid, and gas phase samples. It allows rapid and selective elemental detection on the target sample and has been extensively applied in many areas, e.g. industrial, environmental, biomedical, and pharmaceutical analysis. [9, 10] Recently LIBS measurements have been performed also in laboratory scale flames. However, LIBS technique has been lacking the dynamic measurement range required for versatile elemental detection in combustion applications. With samples containing high concentrations of desired analyte element, LIBS measurement sensitivity suffers from optically thick conditions that leads to self-absorption deteriorating the attainable emission signal. In addition, LIBS falls behind its competing techniques in limit of detection (LOD) that hinders the detection of trace elements. Therefore the measurements in combustion applications have been so far limited to cover the few fuels and elements that fall within the LIBS measurement range. Although there are various techniques to enhance the properties of LIBS, none of those have been applied in combustion environments. In this Thesis, the possibility to use microwave radiation to mitigate the shortcomings of LIBS is studied in detail and novel burner design is presented that enable flame calibration for broad concentration range. Microwave-Assisted LIBS (MW-LIBS) can also be applied on solid, liquid, and gaseous samples of which solid and gaseous samples were demonstrated during the work aiming to this Thesis. In addition to ability to reduce self-absorption presented in the attained emission signal, MW-LIBS's potential lies in trace

element analysis as its detection limit can reach down to parts-per-billion (ppb) level.

1.2 Structure of the Thesis

This Thesis consists of six chapters that describe the frame that changing energy sector is setting for future technologies, outlines background behind the applied methods, and presents the obtained results. Chapters 1 and 2 are describing the problems that thermal heat and power production are facing due use of carbon neutral fuels. Chapter 2 also describes the current understanding of the chemistry behind alkali metal-induced operational problems in combustion environments with main focus on potassium chemistry. In Chapter 3, the state-of-the-art of high temperature chemistry monitoring is reviewed mainly concentrating on optical online methods but also non-optical and sampling measurement techniques are briefly described. Chapter 4 describes the unique CPFAAS technique for measurement of potassium reaction dynamics. The reaction kinetics of reaction between potassium and O_2 is studied in detail and the obtained results are applied for reaction environment monitoring. The development of MW-LIBS is outlined in Chapter 5, which explains the basic phenomena behind laser-induced plasma and then delineates the character of microwave penetration to the plasma and the effects that it rises. Furthermore, Chapter 5 gives detailed description of evolution of MW-LIBS from solid samples to temporal elemental monitoring during thermal conversion of biomass pellet in specifically designed laboratory scale burner. The novel MW-LIBS approach is also compared to previously reported LIBS enhancement techniques and the benefits and drawbacks are discussed. Chapter 6 concludes this Thesis connecting it to other research and suggesting future work to make use of developed methods.

The premise of this Thesis was laid by the research presented in four peer-reviewed publications that are included in the appendices.

2

High-Temperature Chemistry in Biomass Combustion

INCREASING prices of fossil fuels and growing concern for the environmental impacts associated with their consumption is causing a shift towards the use of renewable and CO_2-neutral biomass feedstocks in heat and power applications. Biomass fuels set new challenges for power plant designers and operators due to low heating value, high content of moisture, and high content ash-forming elements including adverse substances for boiler structures. In this chapter, the biomass fuels are presented and the new challenges are discussed. In addition, the role of alkali metals and their problematic nature in in high-temperature environments is described.

2.1 Biomass Fuels and Associated Challenges

Biomass is the plant material formed from synthesis of CO_2, water and sunlight. Therefore, thermal conversion of biomass fuel is not considered to produce new CO_2 into the atmosphere but it is seen as renewable and CO_2 neutral source of energy. The ideal biomass feedstock can be produced cheaply with a high mass and energy yield per unit area of land, requires little energy to produce and collect, and has low concentrations of contaminants. The clear advantage of biomass fuels over fossil fuels is that they are indigenous products available in most parts of the world

through natural processes or as an organic waste. Examples of biomass fuel sources are wood, wooden waste, agricultural residues, and industrial residues. However, to meet the increasing demand of biomass fuels, dedicated production is required. As a result, this may lead to increases in fuel prices as, in general, specialized biomass production is more expensive than use of residues and wastes. [4]

Conversion of biomass to bioenergy is mainly done via direct combustion pyrolysis, gasification, and liquefaction. [11] Traditionally, biomass has been converted to energy via direct combustion and it is the most widely used method for conversion of biomass to energy contributing 97 % of the global bioenergy production. Thermal conversion of biomass consists of three main stages: drying, devolatilization, and char conversion. These are graphically described in Fig. 2.1. Biomass fuels typically have high moisture content ranging from 40 % up to 100 % dry basis and, hence, drying has high impact on biomass combustion characteristics. Drying takes place when the fuel particle reaches 100 °C and water evaporates from its surface. [12, 13] Devolatilization does not occur until the fuel particle has dried sufficiently to allow particle temperature to further increase. Therefore, high moisture content slows down the ignition of fuel particles and decreases the burning rate. [13] High moisture content prevents the fuel to react spontaneously and, in practice, if the moisture content exceeds 55 % wet basis, supplemental fuel is required. [14] Common practice to reduce the CO_2 footprint of coal combustion is to use up to 20 % of biomass fuel mixed with the coal. In this co-combustion scenario, the problems caused by the high moisture content are suppressed and leads only to slight instability of flame and delayed ignition point. [15]

Biomass typically contains high fraction of volatile matter. Volatile matter includes all constitutes, except moisture, that are released from the fuel into the gas phase without presence of oxygen. During devolatilization stage of combustion, also known as flame burning stage, the volatile matter is vaporized into the gas phase due to the increasing fuel particle temperature. The concentration of volatile matter in coal is typically around 35 %. [17] In contrast, the concentration of volatile matter in biomass is much higher. The volatile fraction in biomass is typically around 75 % but can be as high as 90 %. [18] The high volatile matter content in biomass causes biomass to ignite at lower temperatures, e.g. at 260 °C, and burn at a higher rate than coal. [13] Different control systems are needed for biomass combustion than for coal combustion in order to account for the higher rates of combustion. As

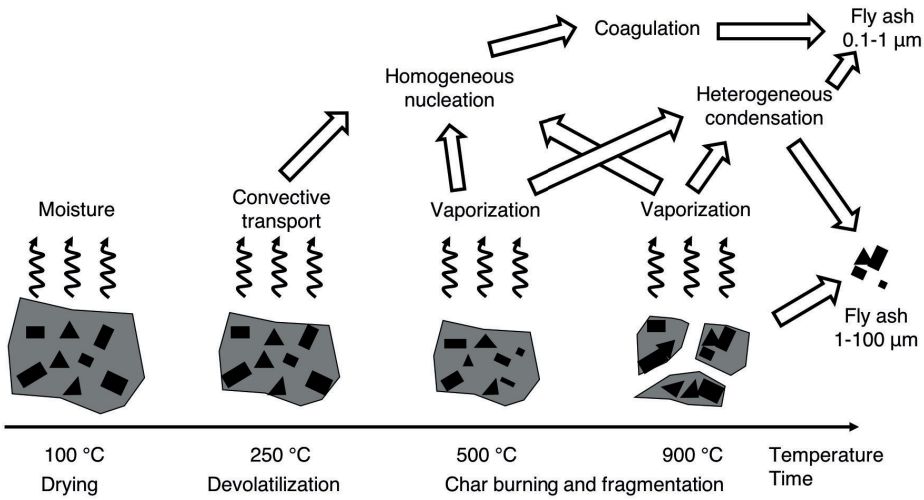

Figure 2.1 *Stages of thermal conversion of biomass and formation of fly ash. The temperature on x-axis refers to the internal particle temperature. Adapted from [16]*

large quantities of volatiles are released quickly, it is required to have longer high temperature zones to achieve complete combustion and reduce pollutant emissions. The implication of this is that the coal combustion units cannot be directly converted into biomass combustion but requires extensive modifications. [18]

The biomass char left after devolatilization is highly reactive and oxidizes easily. [19] Char oxidation reactions caused by CO_2 and H_2O are occurring already at temperatures below 800 °C. [20–22] The biomass char contains high concentration of catalytically important ash forming elements, such as potassium, sodium, and calcium that partially explains the high reactivity. [23] Another aspect of increasing the char reactivity is the high internal specific surface area. [2] The solid residue remaining after complete conversion of the organic constituents of biomass, i.e. volatile matter and char, is referred to as "ash". The main ash-forming elements in biomass fuels are Si, Al, Ti, Fe, Ca, Mg, Na, K, S, and P. [18] The composition of ash varies between different biomass fuels, hence the ash chemistry is very specific for each fuel. Generally, ash is divided into two categories: bottom ash that is left to the boiler bed and fly ash that is carried with the flue gas. These ashes are very different in chemical composition and behavior. Fly ash particle size vary from 10 nm up to 1 mm. However, the fly ash is generally very fine as the median size is dominantly below 100 µm. It has been

Table 2.1 *Properties of selected fuels. Elemental analysis was performed using chemical fractionation [25].*

Fuel	HHV (MJ/kg)	Ash (wt-%)	K (mg/kg)	Na (mg/kg)	S (mg/kg)	Cl (mg/kg)	Ca (mg/kg)
Coal	28.9	12.9	1600	270	2500	9	4500
Poplar	19.4 [26]	1.4 [26]	2910	40	196	702	4150
Straw	18.9	4.9	9100	200	810	900	3500
Algae	21.7	10.10	9250	14300	11700	19800	2600
Waste wood	22.2	1.1	330	2000	54	610	2200

found that the alkali chlorides and trace elements are normally enriched in the finest fly ash fraction. [24] Ash deposition and its effects on steel surfaces are major sources of biomass related problems of thermal heat and power production. These problems include alkali chloride induced corrosion, erosion, deposits on furnace walls (slagging), deposits on convective heat surfaces (fouling) and bed agglomeration. High rates of slagging and fouling are due to the low-melting salt mixtures present in biomass ashes. Sticky fluid or amorphous ash is very prone to stick on metallic boiler surfaces creating molten deposits. The corrosion rate on a steel surfaces is further increased due to the molten nature of the deposits. [2, 18] Ash-forming element concentrations and Higher Heating Values (HHV) of selected biomass fuels are presented in Table 2.1.

Heat and power production by thermal conversion of biomass is carried out in multiple different types of furnaces. The three most common furnace types are fixed bed, fluidized bed, and entrained flow reactor. Fixed bed furnaces include wood stoves, grate boilers, and understroker furnaces. These have been already used for number of years for biomass combustion. [27] Bubbling fluidized bed (BFB) and circulating fluidized bed (CFB) furnaces allow more efficient conversion of biomass and therefore are more suitable for large-scale applications. A schematic of a BFB boiler is shown in Fig. 2.2. The entrained flow reactor has the highest carrier gas velocity of these furnace types, hence, it can be expected to perform with the highest efficiency. [11] In entrained flow reactor, the fuel feed is ignited with natural gas burner before pneumatically injected into an externally heated tube. [28] Biomass fuel feedstocks are also used as co-fuels in coal-fired plants. Co-firing of coal and biomass can be implemented in all coal plants almost immediately. Mixing ratios up to 20 % of biomass can be used in traditional coal plant with minor alterations in fuel feeding and ash considerations. The benefits of

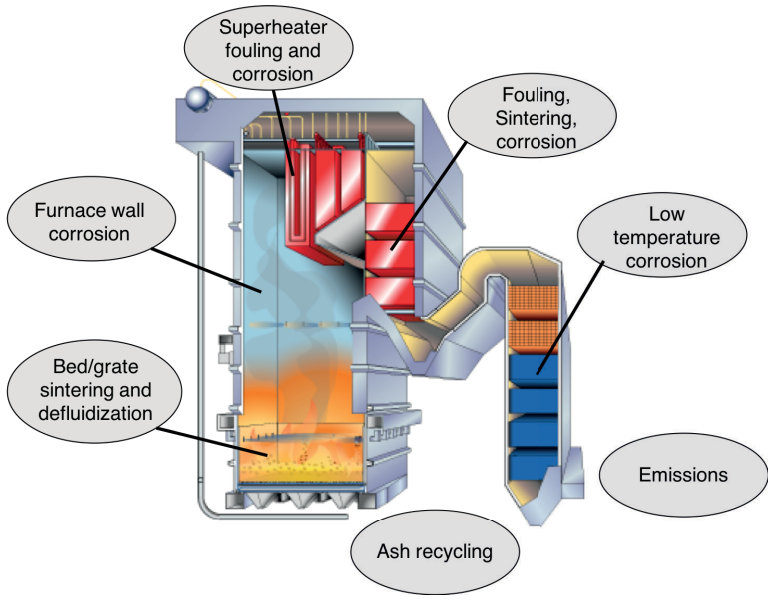

***Figure** 2.2 Schematic presentation of BFB boiler and biomass associated problems in thermal heat and power production. [2] Figure adapted from BFB boiler schematic courtesy of Valmet Technologies Oy.*

co-combustion comes as reduced fuel prices, reduced greenhouse gas emissions, and, in addition, co-firing reduces SO_x and NO_x emissions of coal combustion due to synergetic effects. [29]

Properties of biomass fuels cause several issues in the boiler operation and structures. Even though fluidized bed furnaces are generally suitable for wide range of biomass fuels, there is a concern of bed defluidization that leads to expensive shut down. [2] Defluidization occur when bed material agglomerates forming bigger particles that are not fulfilling the fluidization condition. Agglomerates are formed due to sticky melt on the bed particle surfaces created by the silicates from the fuel. This problem is the most prevalent in the case of fuels containing high levels of potassium or sodium. [30] Also, fuels containing high concentrations of P have shown a tendency to cause agglomerates. [31]. In grate furnaces, grate sintering has been found to be problematic. It occurs via similar mechanism as bed agglomeration. Grate sintering forces the furnace to be shut down for manual cleaning of the grate to maintain efficient combustion conditions. [32] The sticky ash forms deposits also on the furnace walls. Severe corrosion effects have been observed due to high concentration of

corrosive salts or corrosive salt forming elements, such as Na, K, S, Cl, Pb, and Zn. The fireside corrosion rate can be decreased with addition of sulfur to the feedstock or by co-combustion of small amounts of coal with the biomass. Also, coating the furnace walls with Ni-based alloys is shown to reduce the corrosion rate. [33]

High-temperature corrosion on superheater tubes is one of the greatest issues for practical biomass-fired boiler operation and design and, hence, it has been under great interest. High-temperature corrosion on superheater tube surfaces is the main reason for lower steam temperature in biomass combustion compared to coal combustion. [2] For example, increase in steam temperature from 400 °C to 500 °C would result 20 % increase in power generated per amount of fuel. [34] The best known reason for severe high-temperature corrosion on steel surfaces is presence of corrosive salts KCl and NaCl. [35] However, there is controversy on the detailed reaction mechanism occurring on the steel surface that leads to the steel oxidation. Corrosion effects are not limited to high-temperature locations but are present also in low-temperature locations of the biomass boiler. Utilization of pre-heaters to improve the use of flue gas heat has introduced the low-temperature corrosion problems. Main cause of low-temperature corrosion is H_2SO_4 that is formed in the flue gas at temperatures lower than 500 °C. [36, 37]

Biomass fired BFB boilers are known to suffer from fouling. Fouling can be extremely problematic for boiler operation. It decreases the plant efficiency due to stack losses and complete clogging leads to a forced shutdown. Long term effects of fouling include erosion and high-temperature corrosion due to corrosive salts in the deposits. [38] Interaction between KCl, NaCl, K_2SO_4, and Na_2SO_4 in the fly ash lowers the ash melting point and increases the adhesion efficiency of the ash particles. [39] Coarse ash particles are deposited on superheater surfaces mainly through inertial impaction. The deposition rate of coarse particles tends to be high due to the high speed and turbulent flow of their carrier gas. Luckily the larger ash particles do not have as high adhesion properties as smaller ash particles. Sub-micron size ash particles are mostly deposited on heat exchanger surfaces by thermophoresis and diffusion. The compounds from gas phase make their way to the deposits either by direct condensation on the deposit surface, or by condensation on ash particle surfaces, or by nucleation forming the fine particle mode. [40] Formation rate of deposits can be decreased e.g. by alkali capture as it usually increases the melting temperature of the ash reducing the adhesion of the ash particles. It can be performed e.g. by using sulfur-containing additives or by co-combustion. [41]

2.2 Role of Alkali Metals in Biomass Combustion

Biomass fuels contain high concentrations of corrosive salt forming elements K, Na, Cl, and S. To understand, and eventually control, the adverse effects of these elements and their compounds in combustion environments, it is crucial to know their reaction paths from fuel to ash deposits on steel surfaces. Alkali metals have been found to have multiple effects on flames and combustion in general. For example, alkali compounds can be used as flame inhibitors and suppressants. [42, 43] Also, co-combustion of biomass on coal fired plants reduces SO_x due to alkali capture of sulphuric oxides [44] and the presence of alkali compounds also improves NO_x reduction [45]. The most adverse alkali elements for power plant operation have proven to be potassium and sodium. They cause severe ash related problems in biomass fired boilers as chlorine carriers and as reactive elements. [35, 46] In this section, the alkali metal chemistry in biomass combustion processes is discussed and described from fuel to steel surfaces. Potassium is used as an example element in reaction equations as it represents alkali behavior well in high-temperature conditions.

The content and release behavior of alkali elements varies significantly between different biomass fuels. The release behavior and mechanisms during devolatilization, char burning, and ash cooking are affected by the alkali metals fractions in both the organic and the inorganic matter and by the availability of reactants, such as Cl, S, and H_2O. [47, 48] The organic fraction of alkali elements is released at lower temperatures than the inorganic fraction as the organic structure starts to decompose at 300 °C. The release rate at low temperatures is fairly slow due to the resistance of still intact organic matrix hindering the diffusion of alkali elements to the particle surface. [49, 50] Primary release of alkali elements occur at temperatures exceeding 700 °C because the sublimation of alkali chlorides is increased. Depending on availability of reactants, chlorine and silicon, sublimation, alongside with K-silicate and aluminosilicate reactions, are dominant release mechanisms of alkali metals at the temperatures prevailing during devolatilization and char burning. The alkali metals can also be released as a result of high-temperature dissociation of carbonates, silicates, and sulfates. [47, 49, 51]

Molar ratio between alkali metals and chlorine in the initial biomass fuel has a major impact on the molecular form of alkali compounds released. Major part of chlorine is released from the fuel at temperatures lower than 500 °C. [52] In case of

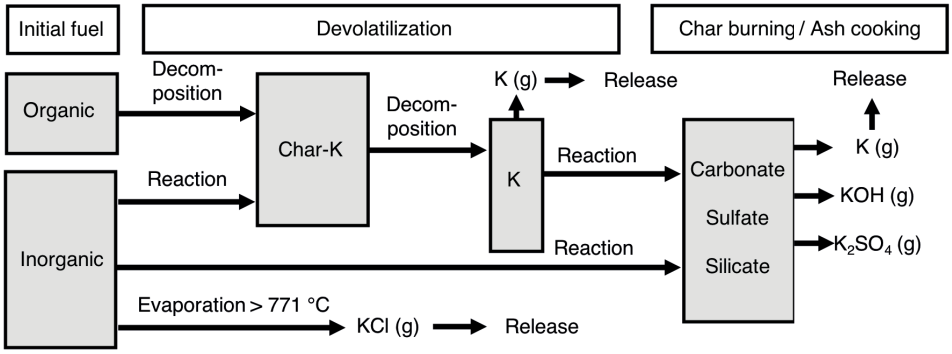

Figure 2.3 *Potassium release pathways from fuel to gas phase during thermal conversion of biomass. Adapted from [47, 48]*

alkali metal excess in the fuel, remaining fraction of chlorine is released as alkali chloride vapor when the particle temperature reaches approximately 700 °C which suggests that inorganic potassium and sodium are evaporated during devolatilization mainly as NaCl or KCl. This eventually leads to complete dechlorination of the char leaving alkali metals to react further to form other compounds. The remaining alkali metals react during devolatilization forming carboxyl-groups and during char burning further decomposes into sulfates, silicates and carbonates. [48] High-temperature dissociation of these compounds releases the alkali elements to gas phase as atomic species or as hydroxides depending on H_2O partial pressure in ambient atmosphere. [47] In the case of excess chlorine, the alkali release mostly occur in the form of alkali chlorides. Also alkali sulfates are present in oxidizing conditions if sulfur is sufficiently available. The excess chlorine is released in from of HCl throughout the combustion temperature range. [47] Coarse generalization of potassium reaction paths from fuel to gas phase are presented in Fig. 2.3. This generalization is further discussed in Section 4.3. Release of alkali metals from biomass fuels can be reduced using water washing or acid leaching techniques. Especially the washing techniques are effective for fuels with high ash content and high inorganic alkali metal fraction. After washing, up to 90 % reduction of alkali release through vaporization during combustion of straw has been observed. [53]

Alkali metals are mainly released to the gas phase as alkali chlorides. They have been observed to be the most adverse alkali compunds for boiler structures. In case of dechlorination, alkali elements are released also in atomic and hydroxide forms during the conversion. High temperature reactions of atomic alkali metals

are discussed in detail in Section 4.1. The chlorine and hydroxide compounds have natural equilibrium in the gas phase through reaction KCl + H_2O ⇌ KOH + HCl. Hence, in wet conditions, the hydroxide concentrations increases. However, high HCl concentration has an even larger impact on the reaction equilibrium and shifts the reaction to the chloride side. [54] After release to gas phase, there are multiple reaction pathways for alkali species. They may even undergo chemical reactions that relief the alkali chloride load in the ash deposits. [46, 49, 52]

Alkali chlorides that do not interact with other species in the gas phase are major contributors to aerosol formation in combustion environment. The alkali compounds are the source of sub-micron size fine particle mode. It has been observed that the particles in this mode contain almost solely alkali metals, chlorine, and sulfur that has led to a conclusion that e.g. KCl nucleation in combustion environment would require condensation nuclei from gas-to-particle conversion of K_2SO_4. [55, 56] The elemental composition and particle size distribution of fine particle mode is affected by the elemental fractions released from the fuel and by the used additives. The amount of alkali chlorides in the typical accumulation fine particle mode 0.1-1 μm is significantly reduced when using high sulfur content fuel or adding sulfur additives. This is desirable as it implies that alkali chlorides are reduced in the gas phase, much lower deposition rate, and reduced corrosion effects with almost zero chlorine in the deposits. [57] Reduction in deposition rate is due to the higher melting point of K_2SO_4 compared with KCl. Hence, aerosol particles containing K_2SO_4 are not as prone to stick to boiler surfaces as particles containing high amount of KCl. [57, 58]

Sulfation reactions of alkali chlorides are highly desirable in combustion applications as they decrease deposition and corrosion rates. [57] However, the sulfation mechanism is not thoroughly known and two different pathways have been proposed. [54, 59] Heterogeneous sulfation takes place as surface reactions under post flame conditions. Alkali precursor molecules are transported to the deposit surface where it is sulfated through reactions in condensed or in solid phase. This is supported by observations that indicates alkali sulfates to be too unstable in flame conditions. [60, 61] Homogeneous reaction pathways of alkali sulfation take place in post-flame conditions in the gas phase. Studies have concluded that solid phase reactions would be too slow to achieve observed sulfation rates. Hence, sulfation would occur in the gas phase and, once formed, alkali sulfates would condense to aerosols. This is supported by the sulfur content found in fine aerosol mode. [56, 62] Irrespective whether the reaction occur in the

solid or in the gas phase, the alkali sulfation is a two-step process and most of the sulfation happens through $KHSO_4$ intermediate $KHSO_4$ + KCl/KOH $\rightleftharpoons$ K_2SO_4 + HCl/KOH. As biomass fuels, in general, have low sulfur content, it is common that ash deposition related problems are aimed to be reduced by using additives or by co-combustion of coal. [57, 63, 64] Often additives, e.g. FeS_2 and $(NH_4)_2SO_4$, are injected into the furnace in water solutions as soluble compounds and are decomposed in wide temperature range. [58] The benefit of additive use over co-combustion of coal is the mitigation of the potential problems due to other coal contained minerals. [57, 65]

KCl is the main alkali chloride in the ash formed during thermal conversion of biomass. Hence, it is the main high-temperature corrosion inducing compound even though NaCl has been proven to be as efficient corrosion agent as KCl. [35] Corrosion in biomass refers usually to oxidation of iron or chromium. However, the detailed reaction mechanism leading to the alkali chloride-induced oxidation is still under discussion. Reaction mechanism that has the most support implies to formation of volatile iron and chromium chlorides that are evaporated away from the high-temperature steel surface and are oxidized to form the porous oxide layer. [66] This corrosion mechanism relies on chlorine cycle, in which the chlorine released in oxidation is diffused back to the steel surface to react further with iron or chromium. However, it is unclear how this cycle would occur in combustion environment and why the KCl molecule is releasing the chlorine to initiate the reaction. [2] It has been suggested that the chlorine is released from the alkali chloride through reaction with SO_2. [46] Further studies have revealed that SO_2 is not required to initiate the reaction implying that there are multiple mechanisms to launch alkali chloride-induced corrosion reaction. [67] Short-term experiments have been revealing more insight to the initiation of alkali chloride induced corrosion reaction. K_2CrO_4 has been found on steel surfaces that have been temporarily exposed to alkali chlorides. This is suggesting that alkali chlorides react first with the protective oxide layer on steel surface exposing the solid steel surface underneath for fast oxidation and simultaneously releasing the chlorine from the precursor molecule. [68] The complexity of the scheme is increased by a finding that also K_2CO_3 has shown corrosion rates comparable to KCl. This means that chlorine is not required for rapid corrosion initiation and oxidation suggesting more significant role for alkali elements in high-temperature corrosion. [69]

3

Measurement Techniques for High-Temperature Chemistry

LIGHT-BASED diagnostics allow non-intrusive online monitoring of high-temperature combustion chemistry. Multiple techniques have been introduced for combustion and flame research all aiming to provide more insight on the chemical processes present in the target system. Because of their versatility, Laser techniques have been applied from laboratory-scale flames up to full-scale power plant boilers. In this chapter, the state-of-the-art of different optical online techniques for high-temperature chemistry monitoring are presented. These methods are then compared with non-optical methods and sampling techniques.

3.1 Optical Online Measurement Techniques

Laser absorption spectroscopy (LAS) has traditionally been conducted using **tunable diode-lasers (TDLAS)**. Recent development in infrared (IR) light sources, e.g. interband- and quantum-cascade lasers, and in hyperspectral light sources, e.g. dispersed supercontinuum lasers and frequency combs, has extended the molecule portfolio and capabilities of LAS to a new level. The wavelength range covered these days by different light sources reaches from about 0.8 μm all the way up to 16 μm, allowing the freedom to design and optimize the measurement arrangement for several purposes. [70]

LAS is based on absorption of light by atoms and molecules. Absorption occurs when photon energy equals to the separation of two discrete energy levels of an atom or a molecule. In the case of an atom, the photon energy is absorbed as an electronic excitation. Molecules can be excited also ro-vibrationally, i.e. the photon energy may cause the atomic distances in the molecule to vary or put the molecule into rotation. The amount of absorbed radiation is directly proportional to the number density of absorbing states. As the states are discrete with certain energy separation that is characteristic for every atom and molecule, it allows only transitions excited by photons with certain energy, enabling recognition of the identity of atom or molecule based on what wavelength is absorbed. These transitions are, however, broadened by various mechanisms, e.g. Doppler broadening and collisional broadening. The resultant absorption line shape can be used to describe the ambient environment of the absorbing atom or molecule. The spectral-line profile is obtained by tuning the wavelength rapidly over the transition and detecting the change in the transmission of the laser light. [70, 71]

LAS methods have been extensively applied to combustion diagnostics as it enables rapid in-situ monitoring of gas phase components and conditions. TDLAS and wavelength modulation spectroscopy (WMS) have been used for fundamental combustion studies in shock tubes concerning the reaction kinetics. Methods are capable to provide simultaneous information on nascent reactants, such as H_2O, CO_2, and CO, and temperature. Uncertainty of below 1 % have been achieved in temperature measurements, which is comparable with other competing methods. [72–74] LAS methods have also been applied on laboratory-scale flames and reactors. The typical parameters of interest in flames are similar to shock tube measurements. H_2O two-line thermometry has also been introduced for these measurements. [75] Also measurements of main combustion gases, such as C_2H_2 [76], CO, and CO_2 [77], have been demonstrated. In addition, H_2O monitoring is applied to verification of global chemical reaction mechanism simulations for single fuel particles. [78]

TDLAS has been applied to alkali monitoring in laboratory-scale reactors. Simultaneous monitoring of H_2O, temperature, and gaseous atomic potassium has been carried out in an entrained-flow reactor. [79] Emission wavelength of a diode laser is rapidly tuned across the potassium D1 absorption line at 769.9 nm and the transmission is measured using photodetector to monitor potassium concnetration in the beam path. [80] The method for potassium monitoring is also applied for

release monitoring during single particle biomass conversion. [81, 82] The common problem of TDLAS is that it has upper concentration limit in which it can operate. In optically thick conditions, the transmission decreases to a level that no longer can be reliably measured and, thus, no absorption line shape can be recovered to enable evaluation of target concentration. However, when the line shape parameters are known or calibrated, truncated absorption profiles can be utilized for concentration measurement. [80] TDLAS technique is very feasible for gaseous atomic potassium monitoring, and by combining different light sources, it can provide simultaneously information on main combustion gases. However, further analysis of potassium reaction paths rely on simulations and kinetic models as TDLAS has not been able to be applied for monitoring of KCl and KOH. Therefore, thorough analysis of alkali reactions requires complimenting measurement techniques.

TDLAS methods are also suitable for full-scale combustion analysis as it enables non-intrusive gas analysis in harsh, and often corrosive, environment. The main combustion gases O_2, H_2O [83], CH_4, CO_2 [84], and CO [85] have been monitored in different boiler types using coal, waste derived, and biomass feedstocks. The TDLAS method has been developed also into commercial product for active combustion control. [86] Furthermore, TDLAS has been harnessed for trace gas monitoring. HCl [87] and NO [88] measurements have been demonstrated in full-scale processes and, in addition, atomic potassium and other alkali atoms have been successfully monitored in a coal-fired plant and in a waste incinerator [89, 90]. As TDLAS provides averaged concentration over the line-of-sight, the method has been combined with atomic emission spectroscopy (AES) to gain spatially resolved data with promising results. [91]

Molecules having absorption bands in the ultraviolet (UV) region can be monitored using **Differential Optical Absorption Spectroscopy (DOAS)**. It is based on measuring transmission of two wavelengths that are tuned to local absorption maxima and minima, i.e. the differential absorption is recorded. Successful DOAS measurement requires detailed knowledge of the absorption spectrum of the target specimen. It has been applied to monitoring of common combustion gas molecules, such as NO, NO_2, SO_2, NH_3, in flue gas. [92] DOAS can also be applied on alkali compound monitoring in UV region and great effort is put to clarify their absorption features. [93–95]. Development of DOAS for alkali chloride monitoring has produced also commercialized product that measures the

sum concentration of KCl and NaCl with ability of simultaneous measurement of SO_2. [96] The measurement of alkali chloride and SO_2 concentrations in gas phase provide essential information on alkali chloride sulfation in combustion conditions. [97] Despite the promising results, DOAS suffers from broad absorption bands that most of the aforementioned molecules have. Overlapping of molecular absorption profiles in UV region limits the applicability of the method for detailed chemical analysis and hinders e.g. distinction of NaCl and KCl.

Differential Absorption Lidar (DIAL) is based on a similar mechanism as DOAS but relies on backscattered light from short laser pulses propagating through a media. It is a single-ended technique, hence, it has great application potential in environments with limited optical access, such as full-scale furnaces. Use of laser pulses enables spatial mapping of absorbing species and, for example, with picosecond pulses spatial resolution of specimen concentration of below 1 cm is achieved. [98] Spatial mapping of gas species in combustion furnaces would provide crucial information on gas mixing ratios as it has significant impact on e.g. NO_x reduction. [99] Despite the application potential of DIAL in full-scale applications, it has been demonstrated only in laboratory-scale flames and tube reactors for KCl [98] and NH_3 [99] detection. **Scheimpflug Lidar** principle has also been demonstrated for single-ended high-temperature characterization. Scheimpflug is an optical principle that describes how large focal depth, for example for a camera, is achieved by tilting a lens in relation to the detector. The principle has been demonstrated for Rayleigh Scattering thermometry and for indium fluorescence detection in laboratory-scale flame. [100]

Cavity Ring Down Spectroscopy (CRDS) is well suited for trace element and trace molecule detection in gas phase as it offers better sensitivity than other absorption based methods. CRDS principle relies on variation in rate of absorption by the species located in an optical cavity. Measurement is typically performed with a laser pulse that experiences exponential decay when trapped inside the cavity. The presence of absorption affects this decay rate with a factor that is proportional to the concentration of absorbing species. [101, 102] CRDS has been applied in different types of flames for trace gas monitoring including combustion intermediates such as OH, HCO and $^1CH_2$. [103, 104] As it is sensitive for low molecular concentrations, CRDS has also been demonstrated for temperature monitoring, for example, in flames that have too low OH radical concentration for

TDLAS measurement. [103,105] The sensitivity of CRDS technique has also enabled monitoring of toxic heavy metal emissions in flue gas. [106]

Laser-Induced Fluorescence (LIF) is a well established technique that offers high sensitivity for atom and molecule concentration measurements as well as temperature, velocity, and pressure monitoring in gas phase. [107] **Planar Laser-Induced Fluorescence (PLIF)** imaging is used extensively in flame research as it provides rapid two, and even three dimensional, information on chemical components and reaction conditions. [108] PLIF premises on laser excitation of atoms and molecules that relaxes emitting fluorescent light characteristic to each molecule. By propagating a laser sheet through a reactive flow, two dimensional image of e.g. desired molecule concentration can be imaged using a camera focused to the laser sheet plane. [109] Many studies have focused on imaging of radicals, such as CH [110], OH [111, 112], CH_2O [113], and fuel fraction [114] that are crucial in flame applications. The obtained PLIF measurement results have also been applied to study chemical reaction kinetics and validate chemical kinetic models. [115–117] PLIF is a very feasible technique on laboratory-scale combustion studies. However, its generalization to wider range of combustion application is very challenging as it is difficult to be upscaled to larger boilers.

Photofragmentation and Laser-Induced Fluorescence (PF-LIF) techniques are commonly used in combustion environments as they are well suited for monitoring of alkali and heavy metal compounds that have luminescent fragments. [118] In PF-LIF, the precursor molecule is dissociated with a UV laser pulse into fragments. These fragments are then excited by the excess energy of the laser pulse or by another laser into a luminescent state. The former case is often referred to as Eximer Laser-Induced Fragmentation Fluorescence (ELIF) as eximer lasers are often used for this purpose. [118] The induced luminescence can be detected with the use of a photodetector or a camera. Photofragmentation techniques enable real-time monitoring of combustion chemistry in dynamic environment that is frequently the case in combustion applications. Recently, the method has been used to image CH_3 [119], alkali species [120] and O_3 [121] in a laboratory flame. Previously ELIF has been demonstrated also in small-scale reactors for monitoring of alkali metal species. [122, 123]

Two dimensional visualization of the main combustion gases, as well as some trace gases, can be obtained by **Polarization Spectroscopy (PS)**. [124, 125] It is pump-probe technique, in which a strong polarized pump beam tuned to an absorption line of the target species creates birefringence and produces a detectable change in the polarization state of the weak probe beam. The species concentration is proportional to the change in the probe beam polarization state. Furthermore, as the polarization signal reflects the distribution of molecular population, temperature at the measurement volume can be determined from obtained spectrum. [126] Measurements have been carried over using both UV and IR wavelengths that has expanded the molecule portfolio of PS technique to cover most gas species relevant for combustion processes. [125] PS have enabled monitoring trace level of gaseous HCl in high temperature conditions and it has been used to map the HCl in-flame distribution to clarify the steps of KCl sulfation. [127, 128]

Another coherent nonlinear technique combining the two dimensional mapping capability and sensitivity is **Degenerate Four-Wave Mixing (DFWM)**. [129, 130] The method is based on $\chi^{(3)}$ interaction of pump and probe beam that produce a laser-like phase conjugated signal beam. [131] UV and visible wavelengths have been used for, for example, sodium [129], NO [132], and SO_2 [133] detection. Introduction of a reliable beam alignment method for IR wavelengths [134] enabled the DFWM method to probe the fundamental ro-vibrational transitions laying in the IR region that has improved its sensitivity and applicability to trace compounds, such as HCl and C_2H_2 in laboratory flame environments. Recently, DFWM was applied to monitoring HCN release during thermal conversion of a biomass pellet. [135]

Fourier-Transform Infrared Spectroscopy (FTIR) is extensively used for molecular measurements in different fields of science. [136–138] It is based on acquisition of an interferogram from a Michelson interferometer, which can then be translated into a spectrum of the inserted light using Fourier-transform. This spectrum can then be utilized for recognition and quantification of the absorbing species present on the path of the input light. [139] Most of the thermal fuel conversion related FTIR studies have been conducted with device incorporating thermogravimetric (TG) approach with FTIR (TG-FTIR). Here FTIR is giving qualitative information on mass data obtained by thermogravimetry that can further be utilized to analysis of e.g. kinetics of pyrolysis. [140, 141] TG-FTIR

provides valuable information on fuel devolatilization temperatures, volatile releases, and interactions of biomass components during pyrolysis that have importance e.g. in formation of NOx emissions. [142–144] FTIR analyzers have also been utilized in boiler environment to study the combustion gases. [37, 145] The problem of FTIR is that it requires sampling from the high temperature reactive volume. The sampling time and cooling of gases may have an impact on the relative proportions of gas concentrations and, hence, may lead to false interpretations. Another option would be to use open path FTIR (OP-FTIR). It has been applied to the monitoring of chemical compounds in combustion emission gases in exhaust plumes. [146, 147] OP-FTIR requires retroreflector to be placed on the other end of the measurement volume to optimize light collection back to the interferometer. Hence, its use in highly scattering environments, such as combustion boilers, is challenging.

Thermographic Phosphors (TP) enable accurate measurement of gas and surface temperatures in combustion conditions with an ideal error of less than 1 %. [125, 148] They are temperature-sensitive phosphors that can be injected into the flame or flue gas using carrier crystals. TP are commonly excited with the use of UV laser pulse. The emission decay time and TP emission spectrum are temperature dependent, hence, after calibration they enable accurate determination of temperature. Spreading of the TP to the carrier gas or on the metallic surface enables 2D imaging of temperature fields. [149, 150] TP have also been used to determine surface temperatures on burning droplets. [151]

Also, scattering techniques have been employed to analyze high-temperature reactive flows. **Rayleigh Scattering** and **Filtered Rayleigh Scattering (FRS)** are extensively used for temperature field imaging [152–154] and mixture fraction mapping in turbulent flames [155, 156]. These methods reach high, up to 40 kHz, repetition rates providing detailed temporal data on highly dynamic reactive flows. [157] They are also often used to compliment other techniques, such as PLIF [158–160], to obtain simultaneous visualization of temperature and reactive species. Also **Mie Scattering** has been employed for combustion studies. It is mainly used to obtain information on particle velocities and their spatial relation to reactive areas in flames. [161–163] The most frequently used scattering technique for major gas species [164] and temperature [165] analysis in reactive flows is **Coherent anti-Stokes Raman Scattering (CARS)**. CARS is a nonlinear phenomena that relies on two pump laser induced Raman coherence in

the target molecule. It is probed with a third laser producing a laser-like signal to a direction that meets the phase matching condition of the three incoming fields. [166] It's main advantages are spectral selectivity and excellent spatial resolution reaching down to 50 μm. [167] Also conventional **Raman Scattering** has been employed to the analysis of high temperature reactions. For example, recently acetylene concentration [168] and the evolution of poly-aromatic hydrocarbons (PAH) from polymers to soot [169] have been studied using Raman Scattering.

Photoacoustic (PA) detection allows sensitive detection of gas phase species. It is based on conversion of optical energy into thermal energy that creates local expansion. This expansion is detected as pressure change using sensitive microphones. [170] Despite the thermo-sensitive components, PA has been applied to high-temperature studies using special acoustic chamber design. One approach has been to use a heat-pipe cell where the PA signal is excited in the heated center of the cell and detected in the water-cooled end of the tube. [171] Another possibility would be to connect the measurement device to the heated sample volume with a narrow signal tube that transmits the excited PA signal. [172] This approach have been demonstrated also on SO_2 and NO monitoring in full-scale CFB furnace. [173] Furthermore, a resonant cell design for high temperature gas studies has been demonstrated. [174]

3.2 Non-optical and Sampling Measurement Techniques

In addition to optical methods for high-temperature chemical analysis, several non-optical approaches have been demonstrated. The most common, and simple, method to measure flame and flue gas temperatures is the use of a **Thermocouple**. [175] It is often used as the gold standard to validate the results obtained by other more sophisticated methods. Thermocouple produces temperature dependent voltage as a result of thermoelectric effect between two dissimilar conductors forming electrical junctions at differing temperatures. However, thermocouples are prone to measurement errors due to radiation losses and conduction. Hence, the values obtained with thermocouples require careful error correction to avoid misleading results. [176] Also, thermocouples have fairly slow response to fluctuating temperatures, causing challenges for dynamic temperature measurements. [177]

Thermogravimetry (TG) is one of the most used analysis methods to investigate gas-solid interaction kinetics during combustion and pyrolysis of solid fuels. [178] The obtained kinetic information helps to describe the practical conversion reactions and design of more efficient reactors. [179] TG measures the sample mass variation over time as the temperature is changed. The mass variation gives insight on physical phenomena occurring in the sample, such as phase transitions, absorption, and adsorption. In combination with Derivative Thermogravimetry (DTG), it also enables determination of main fuel characteristics, such as heat value and moisture content. [180]

Surface ionization (SI) has been extensively applied to analysis of alkali atoms and alkali-containing compounds as alkali elements have exceptionally low ionization potentials being prone to form ions during desorption from hot surface. The produced ions can be detected in the form of electric current with high sensitivity, providing overall precursor detection sensitivity of sub-ppb level. [181] However, SI method is not very amenable for other metal species and it does not discriminate between the alkali elements or whether the detected current originates from gas phase or fine particles. SI approach has been introduced for online monitoring of alkali release in laboratory-scale reactor [182–184] and in full-scale pressurized CFB boiler [185].

Plasma Excited Alkali Resonance Line Spectrometry (PEARLS) is a form of direct current (DC) plasma spectrometry developed for alkali measurements. It is based on mixing the sampled flue gas into a nitrogen plasma jet that atomizes the alkali species. The atomic elements are further detected using atomic emission or atomic absorption spectroscopy. [186] PEARLS has been applied to alkali release studies in a BFB boiler during co-combustion of coal and forest residues. [187] Derivative technique of PEARLS is Heavy Metal Monitor (HEAMON) that has been demonstrated for toxic heavy metal monitoring in flue gases. [188] It has also been demonstrated in bench-scale BFB boiler for continuous cadmium, lead, and copper monitoring. [189]

Inductively coupled plasma (ICP) spectroscopic techniques have similar approach for elemental analysis as in PEARLS. The extracted flue gas is conducted into a nebulizer that feeds the sample droplets into a radio-frequency plasma. The plasma vaporizes the droplets and decomposes the molecules into atoms. The atomized sample can then be detected using different methods, such as

atomic emission [190] or by a mass spectrometer [191]. Attributes associated with ICP includes rapid, simultaneous multielement analysis, sub-ppb detection limits, and wide linear dynamic range. However, ICP is not feasible for fast dynamic measurements as the signal integration times are typically fairly long compared with fully optical methods and, hence, would mostly be suitable for emission monitoring of continuous processes. [192] ICP has been employed on combustion studies as an elemental analysis method for fuel and ash samples. It has provided insight on elemental release quantities during different stages of combustion. [47]

Molecular Beam Mass Spectrometry (MBMS) has been applied to online monitoring of alkali species released during thermal conversion of biomass fuels. [193] It has also been used to study how fuel leaching affects the release quantities. [194] MBMS is based on sampling and ionization of the flue gas. The induced ions, such as K^+ and KCl^+ for potassium species monitoring, are channeled to a mass spectrometer for identification. In this manner simultaneous information on e.g. K, KCl, and KOH release is obtained. [193]

4

High-Temperature Potassium Reaction Kinetics and Applications for Combustion Analysis

Potassium has been identified to be one of the most problematic elements in biomass combustion process as it is the most abundant alkali in most of biomass fuels and is associated with severe corrosion effects on high-temperature boiler surfaces. [46] Collinear Photofragmentation and Atomic Absorption Spectroscopy (CPFAAS) is recently introduced laser-based technique for monitoring of alkali species in the gas phase. [8] CPFAAS allows sensitive molecule specific measurement of alkali chlorides and alkali hydroxides in high-temperature applications and has proven to be scalable from laboratory-scale furnaces to full-scale power plant boilers [195, 196] with ability to follow fragment reaction kinetics [**Paper I**]. In this chapter, the atomic potassium reaction paths and their kinetic nature is discussed. Also, the basic principle of CPFAAS method is described and its application to study of potassium reaction kinetics in high-temperature conditions is presented. In addition, the utilization of chemical reaction kinetics for gas phase composition and condition monitoring is introduced. [**Paper III**]

4.1 Potassium Reactions in High-Temperature Conditions

Potassium plays a crucial role in high temperature chemistry that leads to multiple adverse effects in biomass fired boilers. It is surprising how an element present only in ppm quantities can have a major impact on chemical reaction kinetics from fuel oxidation to steel corrosion. Depending on reaction conditions, potassium may act as an inhibitor or a sensitizer for fuel oxidation. Alkali containing additives are long known to act as flame inhibitors. [197] Their inhibiting effect is based on ability of alkali elements to promote radical removal in flames that slows down the fuel oxidation. [198–200] However, some studies have shown opposite results in certain conditions. [201, 202] Mechanism of inhibition is still lacking consensus but most likely the reaction path is

$$\begin{aligned} &\mathrm{K + OH + M \rightleftharpoons KOH + M} \\ &\mathrm{KOH + H \rightleftharpoons K + H_2O} \\ &\mathrm{KCl + H \rightleftharpoons K + HCl,} \end{aligned} \tag{4.1}$$

where M stands for a non-reactive molecule. The radical removal reduces also NO_x emissions as it intervenes the NO_x formation mechanisms. [202] It has also been proposed that alkali metals could be used as additives in in-furnace NO_x reduction approaches, such as in re-burning, as they have been observed to enhance the reaction rate in low radical conditions. [203, 204] In addition to radical removal, presence of alkali metals in combustion process has immense impact on the chlorine and sulfur transformation, as discussed in Chapter 2. Presence of alkali species in flames has been found to affect soot formation and particle size distributions. Addition of alkali metals has shown to decrease the soot particle size whereas the number density is increased considerably. [205, 206] There is no full consensus on the interaction mechanism between soot and alkali metals, but strong indications have been towards ionic interaction as the soot removal efficiency of a given metal depends on reaction temperature and ionization potential of the element. [206] Thus, potassium has higher impact on soot formation than sodium. [207, 208]

Under reducing combustion conditions, there is consistent evidence that the flame inhibition mechanism follows Reaction 4.1. However, the inhibition mechanism is more unclear under lean conditions. It has been suggested that chain-terminating reaction

$$K + O_2 + M \rightleftharpoons KO_2 + M \tag{4.2}$$

would play an important role in flame inhibition [209, 210], but it has also been questioned whether KO_2 is stable enough to play that role in flame conditions. The reaction rate constant k_1 for Reaction 4.2 and the thermal stability of KO_2 determines its importance in combustion conditions. Provided that KO_2 is sufficiently stable in high-temperature conditions, the high-temperature effects are not limited to flame inhibition. It has also an impact on SO_2 oxidation which is a significant factor in thermal power and heat production as it affects aerosol formation, SO_2 emissions, and alkali compounds in ash deposits. [211] As K + O_2 chemistry has great impact on combustion characteristics, the detailed kinetic information is of great interest.

Previously, the reaction kinetics for KO_2 formation in combustion conditions have been determined experimentally using LIF [212], time resolved atomic resonance absorption spectroscopy [213], and PF-LIF [214]. For example, reaction rate of $k_1(T, M = N_2) = [(8.00 \pm 1.74) \times 10^{-30}](T/300)^{-(1.32 \pm 0{,}04)}$ cm^6 molecule^{-2} s^{-1} has been suggested. [214] However, the measurements have been limited to temperature range of 250 - 1100 K. The reaction rate for K + O_2 reaction has also been determined by indirect means from lean premixed flame studies and using theoretical computation. [210, 215] In addition to reaction kinetics of KO_2 formation, flame studies and theoretical computations have been applied to the study of KO_2 dissociation energy, which was determined to be approximately 172 ± 4 kJ mol^{-1}. [214, 216] [**Paper I**] However, experimental values for KO_2 dissociation energy have suggested a higher dissociation threshold than that deduced theoretical studies. [214, 217] So far, no direct method exist to measure KO_2 dissociation energy. Relief on this shortcoming can be provided with the technique called Collinear Photofragmentation and Atomic Spectroscopy (CPFAAS) which, in addition, offers the capability to provide further insight into the reaction kinetics of the K + O_2 reaction.

4.2 Collinear Photofragmentation and Atomic Absorption Spectroscopy

Multiple techniques have been introduced for alkali detection in high-temperature applications, as presented in Chapter 3. However, few of them have shown to be as versatile and adaptable as CPFAAS. This technique has been demonstrated for KCl, KOH, and $PbCl_2$ monitoring in laboratory conditions as well as in full-scale power plant environment. [195,196,218] Furthermore, it has the ability to monitor chemical reaction kinetics and reaction conditions in the gas phase. [**Paper I**, **Paper III**]

CPFAAS is based on UV photofragmentation and fragment detection using direct atomic absorption. Photofragmentation techniques are extensively used in process monitoring [118] and photofragmentation properties of multiple molecular species are well known [219]. Development of pulsed solid state lasers have made UV light sources for photofragmentation well available and affordable improving the analytical performance in multiple applications. [220] Photofragmentation, known also as photodissociation, is initiated when a molecule absorbs a photon that excites it to one of its dissociative states. On a dissociative state, electrons of the molecule are in a repulsive configuration that leads to dissociation of the bond and fragmentation of the molecule. [221] For example, in the case of KCl, a photon with energy of 4.661 eV excites the KCl molecule from ionic ground state $^1\Sigma^+$ to covalent state $^1\Sigma^+$ that is repulsive. Atomic potassium and chlorine are produced as fragments lying at atomic states $^2S_{1/2}$ and $^2P_{1/2}$ or $^2P_{3/2}$, respectively. [196]

Detection of produced fragments enables identification of the precursor molecule, as fragments and their states are often precursor specific. [220] CPFAAS relies on alkali fragment detection using atomic atomic absorption. Alkali atoms have well known, narrow, and characteristic absorption lines that allow their monitoring with high detection sensitivity, in the order of 1 ppb. [8] Fragmentation of KCl and KOH with photon with energy of 4.661 eV produces atomic potassium fragments that are in their ground state. Hence, detection of potassium fragments can be carried out using the potassium the D2 absorption line which corresponds to the electronic transition from $^2S_{1/2}$ to $^2P_{3/2}$ with an energy difference of 1.617 eV and translates to a wavelength of 766.5 nm. [8, 196] Thus, atomic potassium can be probed with a laser that is tuned to this wavelength. Variations in potassium concentration can be detected as changes in probe laser beam transmission. The transmission change can be translated into potassium concentration using the Beer-Lambert law

$$I/I_0 = \exp\{-\sigma XL\}, \tag{4.3}$$

where I_0 is the initial transmission intensity of the probe beam, I is the probe beam transmission intensity after the change in potassium concentration, σ is the absorption cross section of potassium, X is the concentration of potassium, and L is the interaction length between the probe beam and the gas sample. [222] Availability of continuous wave (CW) distributed feedback (DFB) diode lasers that emit at wavelength of 766.5 nm with a narrow wavelength distribution has made direct absorption measurement of potassium straightforward. The DFB laser is tuned to potassium D2 absorption line using external reference cell that contain atomic potassium vapor to ensure the absorptive light-matter interaction in the sample volume. [195]

The fragmenting laser pulse and the CW potassium probe beam are overlapped in the measurement volume to enable measurement of fragment potassium concentration. Traditional collinear measurement alignment of CPFAAS is presented in Fig. 4.1. Collinear alignment provides spatially averaged measurement along the overlapping beam path. When more localized measurement is required, beams can be aligned to overlap in orthogonal manner in the desired measurement volume. [**Paper I**] The temporal change in probe beam transmission is recorded with a photodetector connected to an oscilloscope. A typical CPFAAS photodetector signal is presented in Fig. 4.2. The transmission intensity I of probe beam drops at the moment when pulsed laser is launched as it produces atomic potassium into the measurement volume. This is seen as a sharp dip in the photodetector signal at time t = 0 μs. The probe beam transmission recovers back to the original intensity I_0 as the produced atomic potassium fragments react with ambient gas mixture and/or diffuse away from the probe beam volume. The temporal transmission intensity of the probe beam has been found to follow expression

$$I(t) = \begin{cases} I_0 & t < 0 \\ I_0 \exp(-\alpha L_{max} e^{-k_1 t} - \alpha L_{res} e^{-k_2 t}) & t \geq 0 \end{cases}, \tag{4.4}$$

where αL_{max} corresponds to the maximum dip in the transmission curve, k_1 and k_2 are the decay constants of the double exponential recovery curve, and αL_{res} is the

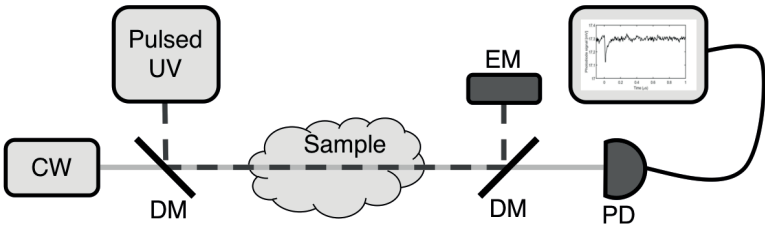

Figure 4.1 *Schematic presentation of typical CPFAAS measurement arrangement with collinear alignment: dichroic mirror, DM; energy meter, EM; photodetector, PD*

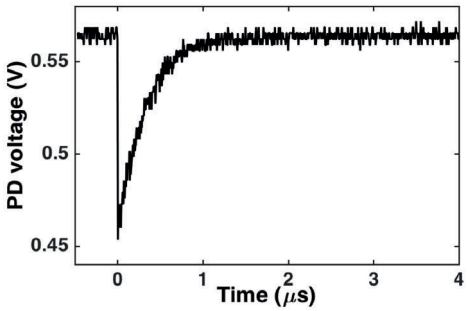

Figure 4.2 *Typical single shot CPFAAS signal obtained from photodetector. The fragmenting laser pulse is launched at time 0 μs causing rapid decrease in probe beam transmission. The transmission recovers back to the original level as atomic potassium reacts with ambient gas mixture or/and diffuses away from the probe beam volume.*

transmission level at which the first part of decay settles. Time t = 0 corresponds to the launch of the fragmenting laser pulse. [222] [**Paper 1**]

The concentration of a precursor molecule in the CPFAAS measurement volume is proportional to the minimum of the transmission curve after launch of the fragmentation laser pulse. The precursor molecule concentration X_{prec} in ppm can be calculated using

$$X_{prec} = -\ln\left(1 - \alpha L_{max}\frac{hc}{\gamma\lambda_f}\frac{1}{\sigma_{frag}}\frac{A_f}{E_{in}}\right)\frac{kT}{p}\frac{1}{\sigma_{prec}L}, \tag{4.5}$$

where h, c, γ, λ_f, σ_{frag}, A_f, E_{in}, k, T, p, σ_{prec}, and L are Planck's constant, speed of light, fragmentation efficiency, wavelength of fragmenting laser pulse, absorption

cross section of the probed fragment, area of the fragmenting laser beam, fragmenting pulse energy, Boltzmann constant, temperature, pressure, absorption cross section of the precursor molecule, and interaction length of the absorption, respectively. The fragmentation efficiency describes how many fragments an absorbed photon produces in average. For KCl and KOH $\gamma = 1$. [223] The UV absorption cross sections for alkali chlorides and hydroxides were recently measured [95] and the absorption cross section of potassium is well known. [195] As all other parameters are experiment-specific but can be easily determined, computation of precursor molecule concentration from CPFAAS signal is straight forward. However, in this Thesis the main focus is on the recovery part of the CPFAAS signal which carries the information on potassium reaction kinetics in the measurement volume.

4.3 Determination of Potassium and O_2 Reaction Kinetics Using CPFAAS

The recovery of CPFAAS probe beam transmission after photofragmentation event is associated with free potassium atom reactions with surrounding gas mixture and/or diffusion out of the probe beam volume. As shown in Section 4.2, the recovery of transmission follows double exponential curve. When the obtained photodetector intensity signal is converted into potassium concentration [K], as shown in Fig. 4.3, the transmission recovery, i.e. the potassium concentration decay, can be written as

$$[\mathrm{K}](t > 0) = [\mathrm{K}]_0 \exp(-k_1 t) + [\mathrm{K}]_0^{\mathrm{res}} \exp(-k_2 t), \tag{4.6}$$

where $[\mathrm{K}]_0$ corresponds to the maximum potassium concentration right after the photofragmentation and $[\mathrm{K}]_0^{\mathrm{res}}$ corresponds to the remaining equilibrium atomic potassium concentration of Reaction 4.2.

It has been observed that $[\mathrm{K}]_0^{\mathrm{res}} = 0$ at temperatures below 800 °C. Hence, the potassium decay curve follows single exponential curve

$$[\mathrm{K}] = [\mathrm{K}]_0 \exp(-k_1 t), \tag{4.7}$$

where k_1 is associated as with reaction rate k_a for K + O_2 addition reaction and

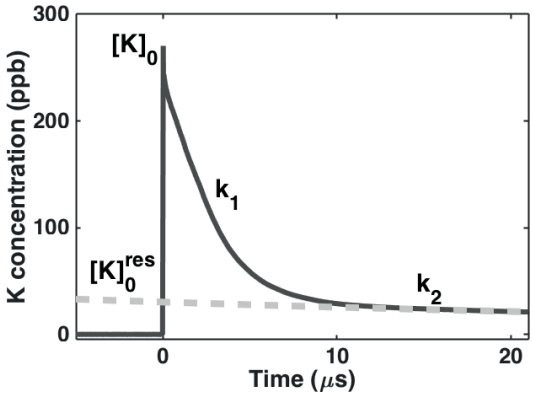

Figure 4.3 *Potassium concentration as function of time during and after photofragmentation event. The fragmenting laser shot is launched at t = 0. k_1 is the decay constant of the first phase and k_2 is the decay constant of the second phase of the decay. $[K]_0$ and $[K]_0^{res}$ corresponds to maximum potassium concentration after photofragmentation and equilibrium potassium concentration after the first decay phase.*

the rate of diffusion of atomic potassium away from the probe beam volume k_d

$$\begin{aligned} K + O_2 &\xrightarrow{k_a} KO_2 \\ K &\xrightarrow{k_d} K_{loss}. \end{aligned} \tag{4.8}$$

Therefore, decay constant k_1 can be written as $k_1 = [O_2]k_a + k_d$. However, for oxygen concentrations present in combustion conditions, the time scales of interest are so short that the diffusion rate k_d is indistinguishable from zero. Hence, $k_1 = [O_2]k_a$. This is confirmed by Fig. 4.4 that shows the expected linear behavior of k_1 against O_2 partial pressure as O_2 partial pressures over 10^{-3} are considered. At lower partial pressures, diffusion and/or other slower reaction pathways play a role in potassium decay. However, O_2 concentration is rarely that low in combustion applications.

A double exponential decay of potassium is observed after the photofragmentation event at elevated temperatures. At temperatures above 800 °C, $[K]_0^{res}$ in Eq. 4.6 has been found to deviate from zero. The first decay phase k_1 is significantly faster than the second phase k_2 having typical 1/e decay time $1/k_1$ of ∼100 ns in comparison to $1/k_2$ being ∼100 μs. The double exponential behavior can be interpreted to originate from reversible formation of an intermediate compound after which the

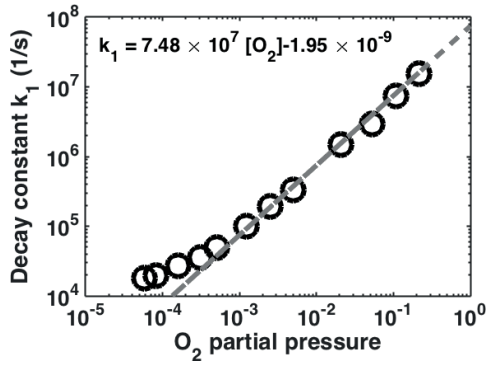

Figure 4.4 *Decay constant k_1 of induced potassium concentration as a function of O_2 partial pressure in fraction of atmospheric pressure. The relation is linear in pressures over 10^{-3}. Adapted from* ***Paper III****.*

intermediate and/or the reactants are lost irreversibly

$$\begin{aligned} K + O_2 &\xrightarrow{k_a} KO_2 \\ KO_2 &\xrightarrow{k_{-a}} K + O_2 \\ KO_2 &\xrightarrow{k_b} \text{loss.} \end{aligned} \tag{4.9}$$

Here, k_{-a} corresponds to the effective first-order dissociation rate of KO_2 and k_b is the effective loss rate of KO_2 away from the measurement volume. The obtained temperature dependency of K + O_2 reaction rate k_{R1} is plotted in Fig. 4.5. The fit on obtained results by CPFAAS measurement [**Paper I**] suggest temperature dependent reaction rate of $k_{R1} = 1.07 \times 10^{-30}(T/1000K)^{-0.733}$ cm^6 molecule^{-2} s^{-1}. However, when compared to previous results [214], it can be noticed from Fig. 4.6 that the curve derived from CPFAAS measurements does not extrapolate well to lower temperatures. Therefore, for temperature interval 250 - 1320 K it is recommended to use reaction rate $k_{R1} = 5.5 \times 10^{-26}T^{-1.55}\exp(-10/T)$ cm^6 molecule^{-2} s^{-1}.

In addition to reaction kinetics of potassium and O_2, CPFAAS measurement has the ability to provide information on the equilibrium state of Reaction 4.2. Thermodynamic equilibrium constant K_{eq}

$$\ln K_{eq} = -\frac{\Delta G}{RT} = -\frac{\Delta H}{RT} + \frac{\Delta S}{R} \tag{4.10}$$

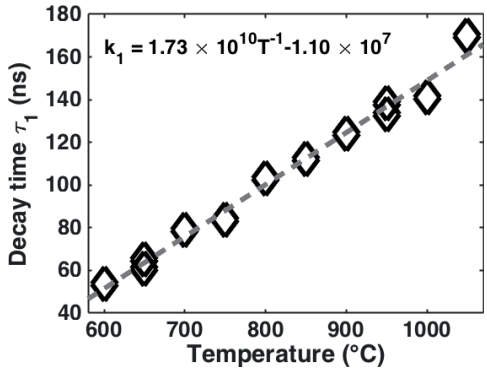

Figure 4.5 *Decay time of induced potassium concentration* $\tau_1 = 1/k_1$ *as a function of temperature measured in 21 % of* O_2*. Adapted from* ***Paper III****.*

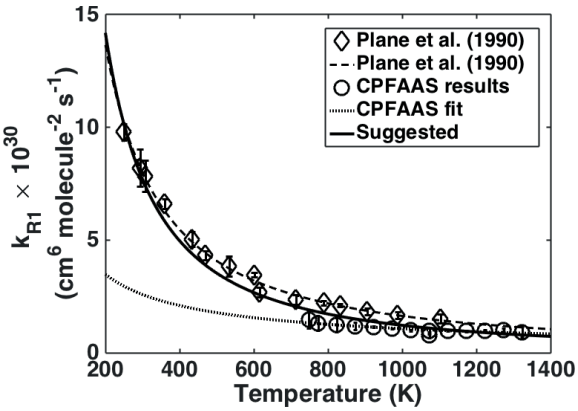

Figure 4.6 *Arrhenius plot for reaction* $K + O_2 + N_2 \rightleftharpoons KO_2 + N_2$ *showing the results from previous work [214] and from the present work* ***[Paper I]****.*

provides the thermodynamic information on the K + O_2 reaction. If the entropy S and enthalpy H would be constants, the van't Hoff plot would yield linear fit. However, temperature dependency of ΔH and ΔS may cause some complications. The information obtained from CPFAAS measurement aids in determination of K_{eq} as it can be determined as

$$K_{eq} = \frac{[KO_2]p_0}{[K]_0^{res}[O_2]}, \tag{4.11}$$

where all concentrations are in partial pressures and p_0 corresponds to atmospheric pressure. Assuming that all atomic potassium produced by photofragmentation

reacts into KO_2, [KO_2] can be written as $[K]_0$-$[K]_0^{res}$ that can be determined from potassium decay curve. Hence, values for ΔH and ΔS can be determined from obtained van't Hoff plot using third-law analysis [**Paper I**] to be ΔS_{298} = 93.6 J K^{-1} mol^{-1} and ΔH_{298} = -184.2 ± 0.5 kJ mol^{-1}. The bond dissociation energy D_0 of a molecule AB can be determined using formation enthalpies [224]

$$D_0(AB) = \Delta_f H_0(A) + \Delta_f H_0(B) - \Delta_f H_0(AB). \tag{4.12}$$

Hence, the dissociation energy of KO_2 can be determined using values $\Delta_f H_{298}(K)$ = 89.0 ± 0.8 kJ mol^{-1}, $\Delta_f H_{298}(KO_2)$ = -95.2 ± 4.1 kJ mol^{-1} and the H_{298}-H_0 values of 12.14 kJ mol^{-1}, 6.20 kJ mol^{-1}, and 8.68 kJ mol^{-1} for KO_2, atomic potassium, and O_2, respectively. The numerical computation leads to $D_0(KO_2)$ = 181.5 kJ mol^{-1} that agrees well with dissociation energy value of 177.9 kJ mol^{-1} computed using coupled cluster single double triple (CCSD(T)) level theory. [**Paper I**]

4.4 O_2 Concentration and Temperature Monitoring with CPFAAS

Localized monitoring of temperature and main combustion gases are highly desired to provide feedback and validation for simulations and models computed for different combustion systems. Conventional thermocouple probe method for temperature measurement is often unpractical as it is slow, intrusive, and is affected by the thermal radiation from the surrounding, e.g. furnace walls. [175] Also, it cannot reach as far as it would be required in full-scale applications and provides information only form wall proximity that is not representative for the whole furnace diameter. Therefore, multiple laser methods have been introduced for this task including TDLAS [72, 225], PLIF [226], thermographic phosphors [227], and scattering techniques [228]. TDLAS has been proven to be the most versatile method among these techniques as it is scalable and it can simultaneously provide information on the main combustion gases like O_2 [89], CO_2 [72], H_2O [225], and CO [229]. However, TDLAS is essentially an line-of-sight method and is usually incapable to provide localized information. PLIF has also been used for O_2 imaging in flames [230]. It is an effective but complex method and suffers from limited scalability further from laboratory-scale flames.

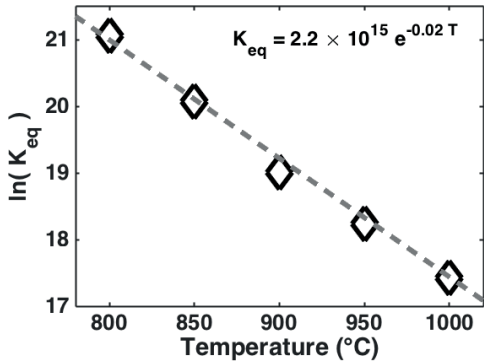

Figure 4.7 *Logarithm of the equilibrium constant K_{eq} measured in 21 % of oxygen in a temperature range of 800 °C - 1000 °C. Adapted from* ***Paper III****.*

In previous section, CPFAAS was proven to be capable to deliver crucial information on potassium reaction kinetics at high-temperature conditions. As the potassium reaction kinetics are well known, the reaction dynamics in unknown atmosphere can be used as characteristics indicator of the reaction environment. The reaction rate and equilibrium state, which both can be determined with the use of CPFAAS signal as described in previous section, are functions of temperature and initial reactant concentrations. Thus, the potassium decay rate and equilibrium concentration of potassium for Reaction 4.2 recorded with CPFAAS are indicators of temperature and O_2 concentration. The temperature and O_2 concentration monitoring is limited to environments at temperatures higher than 800 °C as the equilibrium concentration of potassium after fragmentation event cannot be evaluated at lower temperatures. However, this is sufficient for multiple combustion applications as they often operate at elevated temperatures.

Calibration measurements were conducted for CPFAAS potassium decay curve in temperature range of 800-1000 °C to obtain a pair of equations required to solve the two unknown parameters, i.e. temperature and O_2 concentration, in arbitrary environment. For K_{eq}, the factor $-\Delta G/R$ in Eq. 4.10 was determined with linear fit to temperature dependent values of $\ln(K_{eq})$. The obtained curve is presented in Fig. 4.7. The observed temperature dependency for equilibrium constant at 800-1000 °C temperature range is $K_{eq}(T) = 2.2 \times 10^{15} \exp(-0.02T)$. The O_2 dependency of K_{eq} rises directly from Eq. 4.11. [**Paper III**]

Similar temperature and O_2 concentration calibration measurements were performed for potassium decay rate k_1 in temperature range 800-1000 °C. The

resulted calibration curves for temperature and O_2 concentration dependency are presented in Fig. 4.5 and Fig. 4.4, respectively. Temperature dependency showed linear behavior with fitted curve of $k_1(T) = 1.73 \times 10^{10} T^{-1}$ - 1.10×10^7. The O_2 concentration dependency of k_1 has nonlinear relation in O_2 partial pressures lower than 10^{-3}. However, these points can be neglected as combustion applications rarely have this low O_2 concentrations. The fit to the linear part of $k_1([O_2])$ curve is 7.48×10^7 $[O_2]$ - 1.95×10^{-9}. These functions can be combined with the K_{eq} calibration functions into a pair of equations

$$\begin{cases} \frac{([K]_0 - [K]_0^{res})p^0}{[K]_0^{res}[O_2]} = 2.2 \times 10^{15} \exp(-0.02T) \\ 1.73 \times 10^{10} T^{-1} - 1.10 \times 10^7 = 7.48 \times 10^7 [O_2] \end{cases} \tag{4.13}$$

that can be used to solve the temperature and O_2 concentration in the CPFAAS measurement volume. [**Paper III**]

Due to the high sensitivity of CPFAAS technique, it has the potential for highly localized measurements. With possibility of orthogonal laser beam overlap arrangement [**Paper I**], the spatial resolution of the measurement can be reduced down to 1 mm. The requirement for successful temperature and O_2 concentration monitoring utilizing CPFAAS technique is the presence of KCl or KOH in the gas phase that can be used as precursor molecules for potassium fragments. The method has been demonstrated during combustion of a black liquor droplet in a single particle reactor. [**Paper III**] In this demonstration, the interaction path length was 1 cm that was the flame width determined from a video recording. In addition to temporal temperature and O_2 concentration measurement, CPFAAS allows simultaneous temporal monitoring of K, KCl, and KOH release during biomass combustion. [195] The obtained release curves, and temperature and O_2 concentration profiles during thermal conversion of a black liquor (570) droplet are presented in Fig. 4.8. KOH was used as precursor molecule for temperature and O_2 concentration measurement as it was better available throughout the conversion process. It can be clearly observed that the measured gas temperature rises above the calibration range during the first stages of combustion. Hence, full confidence cannot be granted for these values. However, the measured values are in good agreement with surface temperature measurements done on black liquor in excess air. [231] Towards the end of the thermal conversion of the droplet, the temperature and O_2 concentration levels to the set values of the reactor giving the

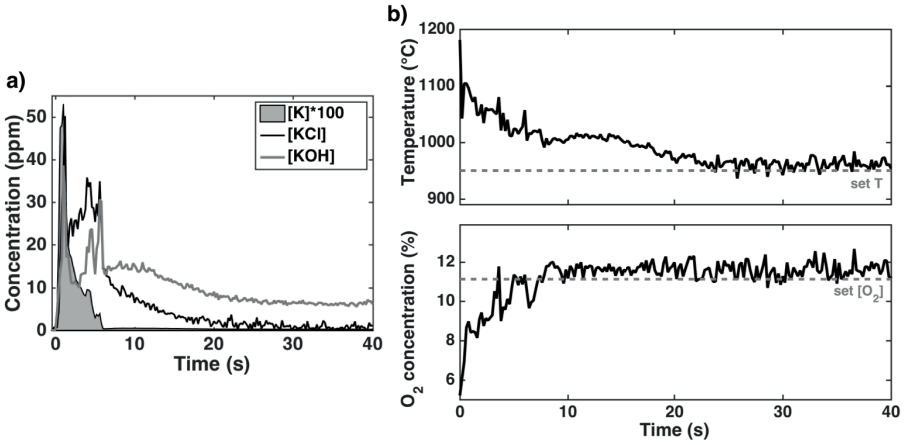

Figure 4.8 *Temporal a) release of K, KCl, and KOH during thermal conversion of black liquor (570) droplet and simultaneously measured b) temperature and O_2 concentration profiles. Reactor set temperature was 950 °C and set O_2 concentration 11.13 % that are marked with a dashed line to the figure. Adapted from* ***Paper III****.*

reference values for the measurement. The set value can be considered as good reference as the furnace temperature was controlled with a thermocouple placed close to the center volume.

The release pattern of potassium species during thermal conversion of black liquor is fairly different from release patterns previously published for wood derived biomass fuels and straw. [195, 196] Instead of sharp burst of atomic potassium in the beginning of devolatilization, it decays slowly towards char burning. This may be due typically very high content of sodium in black liquor [232] that dominates chlorine and hydroxide formation in the first stage of conversion leading to release of atomic potassium. Dechlorination of the fuel sample leads also elevated KOH release in the end of char burning stage at conversion time of about 10 s. Similar behavior has been observed in thermal conversion of torrefied wood samples that are known to have low chlorine content. [196] Surprisingly high KOH release is recorded also in the beginning of devolatilization. This is in disagreement with the proposed generalizations of potassium release during biomass combustion presented in Fig. 2.3. As the potassium species are measured 7 mm above the sample, the high KOH concentration may be explained by high moisture content of lack liquor that enables atomic potassium to react with elevated H_2O in gas phase,

as described in Reaction 4.1. However, this together with previous release patterns measured with CPFAAS [196] shows that alkali release patterns vary significantly from fuel to fuel and generalizations and simplifications may lead to false conclusions. This demonstrates well the capability of CPFAAS to produce valuable information on combustion processes giving feedback to models and simulations.

5

Microwave-Assisted Laser-Induced Breakdown Spectroscopy

TEMPORAL behavior of total elemental release during thermal conversion of biomass provides valuable information for models and simulations to characterize the conversion process. As the elemental content is distributed to multiple different molecules in the gas phase and as condensates and fractions to aerosol particles, direct measurement of e.g. KCl concentration does not provide the full picture of total amount of potassium released. Laser-Induced Breakdown Spectroscopy (LIBS) enables temporarily resolved detection of elemental species in solid, liquid, and gas phase, and, therefore, it has become a workhorse of analytical atomic spectroscopy in different disciplines of science and industry. [9, 10] However, LIBS's analytical performance is limited and does not tackle all challenges that are present in combustion related applications, such as low detection limits and broad dynamic range. Thus, the analytical performance has to be improved. In this chapter, the basic principles of LIBS are introduced and the development and application of microwave-assisted LIBS (MW-LIBS) for elemental release studies is presented.

5.1 Background and Principles of LIBS

Sensitive, fast, and reliable online elemental detection is required in multiple different disciplines of science and industry. Many of current elemental analysis techniques,

such as chemical analysis [233], x-ray fluorescence (XRF) [234], mass spectrometry [235, 236], and inductively coupled plasma (ICP) applications [237–239], are rarely fast enough to allow actual online monitoring capability as they require sample preparation, devices are bulky, and/or the signal collection is too slow. However, optical atomic emission technique named LIBS has the ability and potential to meet the requirements set in multiple online elemental detection schemes. Therefore, it has become a topic of numerous studies and target of commercialization. [9, 10, 240] LIBS's attractive qualities include no or minimal sample preparation, stand-alone capability, information richness, and ability to measure elemental compositions in solid, liquid, and gas phase samples. It is also a fairly simple technique and, in principle, elemental composition of a sample can be resolved with a single laser pulse and a spectral detector. Therefore, LIBS has found its way to multiple applications from pharmaceutic [241] and mining [242] industries to Mars rovers [10, 243].

LIBS is based on detection of atomic emission from laser-induced plasma. Plasma is the fourth fundamental state of matter. It is a local assembly of atoms, ions, and free electrons being an extremely energetic form of matter. Plasma is typically characterized based on its level of ionization. Laser-induced plasmas are usually categorized into weakly ionized plasmas where less than 10 % of the species are free electrons. [244, 245] High irradiance of light is required to induce a plasma plume on matter. Therefore, pulsed laser sources are mandatory and focusing of the laser beam is required to achieve irradiance exceeding the plasma induction threshold value that usually lies from a few GW cm^{-2} to hundreds of GW cm^{-2} range depending on sample, laser pulse wavelength and pulse temporal width. [244, 246] In air, the high electric field of the laser pulse leads to air breakdown and rapid growth of free electron density which further induce a strong absorption of the laser pulse. Initial free electrons may be produced by photoionization or by natural background radiation. The free electrons gain energy from the laser pulse through inverse bremsstrahlung and collide with atoms producing more free electrons causing cascaded increase in the electron density n_e. [247] In case of solid samples, the leading edge of the laser pulse is interacting with the sample matter and causes heating, melting, and vaporization of the sample. This process is called ablation that introduces ablation fume consisting vapor and particles from the sample. On solid samples, the required minimum irradiance can be approximated by using equation

$$I_{min} = \rho L_v \varkappa^{1/2} / \Delta\tau_p^{1/2}, \tag{5.1}$$

where ρ is the density of material, L_v is the latent heat of vaporization, $\varkappa$ is the thermal diffusivity of the sample and $\Delta\tau_p$ is the width of the laser pulse. After ablation, the remaining laser pulse starts to heat the ablated material initializing the plasma formation. Energetic laser pulses may produce plasma with such a high electron density that the plasma becomes opaque to the laser beam and laser pulse heats solely the plasma front growing it to the direction of incoming laser beam. The electron density n_e when the plasma becomes opaque for electromagnetic radiation with certain wavelength λ is called critical electron density n_c that can be estimated using

$$n_c \sim (10^{21}/\lambda^2)/\mathrm{cm}^3, \tag{5.2}$$

where the wavelength is inserted in microns. [9, 244] Formed plasma expands to the surround adiabatically like a piston compressing the ambient gas and creating a shock wave. The counter pressure from the created shock wave decelerates the plasma expansion reheating it and forming internal plasma shock wave that homogenizes the plasma transforming the most of the internal energy into thermal form. The expansion is not adiabatic anymore and the plasma temperature, particle velocity, and plume pressure decreases. Eventually the plasma loses all its thermal energy and its lifetime comes to its end. [248] The electron density and temperature in typical laser-induced plasmas exceed $n_e > 1 \times 10^{16}$ cm^{-3} and $T >$ 5000 K, respectively. [9, 249–251] At initial conditions of plasma, beginning of the expansion and close to the sample surface, and in the center of the plasma with high electron density the plasma may be considered to be in local thermal equilibrium (LTE) that is connected to the description of the plasma state and its physical parameters. In LTE condition, the following conditions hold: all species in the plasma have a Maxwellian velocity distribution, and excitation of species is due to thermal excitation or collisions. LTE is required to simplify the description of atomic emission intensities and plasma parameters; under LTE conditions, a single temperature and electron density suffices to describe the physical characteristics of the plasma. However, LIBS dynamics have extremely complex light-matter and light-plasma interactions, and complex parameter matrix causing small perturbations in experimental parameters which consequently influence the plasma characteristics significantly. Hence, absolute calibration free LIBS (CF-LIBS) is very challenging to produce due lack of complete descriptive theory. [9, 245, 252, 253]

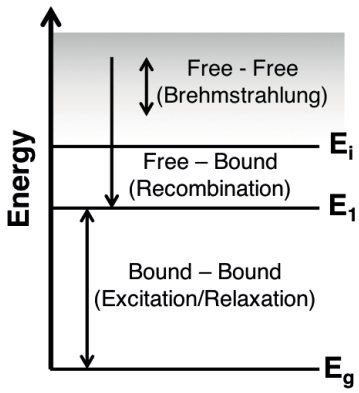

Figure 5.1 *Schematic presentation of electronic energy transitions present in laser-induced plasma.*

Laser-induced plasma emits electromagnetic radiation that can be classified into three different categories based on the radiative mechanism. In general, electromagnetic radiation is produced either through radiative decay of atomic or molecular excitation or deceleration of a charged particle. In plasmas, both of these mechanism are present and the schemes are schematically visualized in Fig. 5.1. The first category of electromagnetic radiation sources is from bound-bound transitions. The bounded electrons either in atoms or ions present in the plasma are thermally excited from a quantum state l to a quantum state u with higher internal energy. As this excitation relaxes, the excess internal energy E_ν is emitted as radiation with wavelength λ_{ul} that is assigned by the relation

$$E_\nu = E_u - E_l = h\nu_{ul} = \frac{hc}{\lambda_{ul}}, \tag{5.3}$$

where E_u and E_l are the energies of the upper and lower quantum state, respectively, h is the Planck's constant, ν_{ul} is the frequency of the radiation emitted from the transition, and c is the speed of light. Hence, the wavelength of the emitted radiation is defined by the electronic level structure of the emitting species. As the electronic structure is unique for every species, the bound-bound radiation, that typically falls into range from ultraviolet to near infrared band of the electromagnetic spectrum, can be utilized to identify the chemical elements present in the emission source. [245]

The second radiation mechanism in laser-induced plasmas is called free-bound transitions. A free-bound transition occurs when a free electron is recombined with an ion. In this case, the initial kinetic energy $E_k = 1/2 m_e v_e^2$ of the electron contributes to the wavelength of emitted radiation

$$E_\nu = E_k + E_i - \delta E - E_u = h\nu, \tag{5.4}$$

where E_i is the ionization energy of the corresponding ion, δE is its lowering and E_u is the energy of the state to which the electron is trapped. As the kinetic energy is not quantized, the free-bound emission spectrum is continuous ranging from ν_{min} corresponding to $E_k = 0$ up to high values of ν. Also the third radiation source, free-free transitions, contributes to the continuous spectrum. The free electrons in the plasma plume are colliding with other charged particles being decelerated and emitting the change in kinetic energy as continuum radiation called bremsstrahlung. This mechanism is the dominant source of radiation during approximately the first 100 ns of laser-induced plasma lifetime typically covering the spectrum from visible to near infrared frequencies. As the bound-bound transitions are the main source of information from the plasma, this continuum radiation is usually avoided in the signal acquisition by inserting a detector delay between the onset of plasma ignition and photon signal detection. Luckily the bremsstrahlung radiation decays much faster than bound-bound radiation, as shown in Fig. 5.2, enabling the collection of the characteristic bound-bound radiation with a much decayed continuum background. [244, 245]

Radiation emitted from bound-bound transition is not strictly discrete and monochromatic but has a wavelength distribution. The emission line distribution is shaped by the emitting source, by natural uncertainty principle, and by the surrounding environment properties, i.e. temperature and pressure. Hence, the line shape can be used to characterize the emission source and environment but the latter requires understanding of the mechanisms that affects the emission distribution. The emitting element or molecule can be recognized by comparing the central wavelength of the emission line or multiple emission lines to database values [254]. Natural broadening of the emission line is due uncertainty principle $\Delta E \Delta\tau \geq \hbar$, where ΔE is the width of the corresponding energy level, $\Delta\tau$ is its lifetime and $\hbar = h/2\pi$. All atomic emission lines are affected by natural broadening that is a homogeneous broadening mechanism, hence, the basic atomic emission

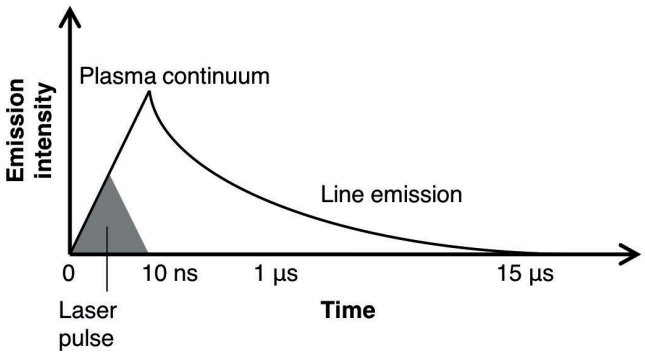

Figure 5.2 *Evolution of radiation intensity and dominating spectral features of a laser-induced plasma*

line shape is described with Lorentzian shape

$$\Gamma_{\mathrm{L}}(\nu) = \frac{1}{2\pi} \frac{\Delta\nu_{\mathrm{H}}}{(\nu - \nu_0 - \Delta\nu_{\mathrm{V}})^2 + (\Delta\nu_{\mathrm{H}}/2)}, \tag{5.5}$$

where $\Delta\nu_{\mathrm{H}}$ is the full frequency width at half maximum (FWHM), $\Delta\nu_{\mathrm{V}}$ is the frequency shift of the line in relation to unperturbed line maximum ν_0. However, in laser induced plasma emission, the dominant line broadening mechanisms are Doppler broadening and Stark broadening. [244, 245, 255] In early stage of plasma formation, electric microfields generated by the charged particles surrounding the emitting atom causes degeneration of sublevels identified by quantum number $\mathrm{m_j}$ that leads to either unresolved broadened line profile or a resolved series of sublevels. This is called Stark effect. It is homogeneous broadening mechanism that depends mainly on electron density and can be written as

$$\Delta\lambda_{\mathrm{S}} = \left[\frac{\mathrm{n_e}}{\mathrm{C(n_e, T)}}\right]^{2/3}, \tag{5.6}$$

where $\Delta\lambda_{\mathrm{S}}$ is FWHM of the spectral line and C($\mathrm{n_e}$,T) is a broadening parameter that is tabulated in literature. [256] The Stark broadening theory is well known for hydrogen, hence, it is often used to determine the electron density of a laser induced plasma. [257] As the plasma plume electron density decreases, the emitted

line shape turns more into Gaussian shape due to Doppler broadening. Doppler broadening is an inhomogeneous broadening mechanism caused by random translational (Brownian) motion that each radiating atom has along the line-of-sight of the observer. It is only dependent on temperature T and mass M_a of emitting specie. It is an inhomogeneous mechanism, and can be described with Gaussian function

$$\Gamma_D(\lambda) = \frac{1}{\Delta\lambda_p \pi^{1/2}} e^{\left[-\left(\frac{\lambda-\lambda_0}{\Delta\lambda_p}\right)\right]^2}, \tag{5.7}$$

where

$$\Delta\lambda_p = \lambda_0 \left(\frac{2kT}{mc^2}\right). \tag{5.8}$$

From the Eq. 5.7, FWHM of the line shape can be solved as

$$\Delta\lambda_D = \left(\frac{8kT \ln 2}{M_a c^2}\right)^{1/2} \lambda_0, \tag{5.9}$$

where k is the Boltzman's constant and $\lambda_0 = c/\nu_0$ is the central wavelength of corresponding emission line. Thus, Doppler broadening can be used to determine the temperature of the emitting species in the laser-induced plasma plume. [244,245,255]

LIBS measurement has the ability to provide information on multiple species due the non-selective excitation. Emitted radiation is typically collected into a spectrometer equipped with a row detector or a camera that records the emission spectrum. In addition to described Stark and Doppler broadening mechanisms, the spectral emission line shape is affected by instrumental function. This is a common problem in emission spectroscopy. The instrumental function is not neither completely Gaussian nor Lorentzian and, therefore, it has to be experimentally determined for each measurement arrangement individually. This is usually done by scanning over narrow, well known spectral line shape, such emission line shape of He-Ne laser. [9]

A typical LIBS spectrum obtained from sample containing copper is shown in Fig. 5.3(a). The recorded line shapes are not always neatly convolutions of different broadening mechanisms but the shape and relative line intensities are deteriorated by self-absorption. When self-absorption occur, the plasma is said to be optically thick for the observed wavelength. This is usually the case when samples with high concentration of analyte element are considered. In case of slight or moderate self-absorption, it is observed as deviation of relative emission line intensities from theoretical ratios. For example, in Fig. 5.3(b) the theoretical intensity ratio of the copper emission lines at 324.75 nm and 327.40 nm is approximately 2. This can be estimated via the statistical weight of $2J_k + 1$, where J_k is the total angular momentum that are collected in Table 5.1. However, it can be clearly seen that this ratio is not obeyed in the spectrum showed in Fig.5.3(b). This is due higher transition probability of the line at 324.75 nm that causes it to be more likely to go through absorption event. In case of severe self-absorption, the recorded lines are self-reversed. Self-reversal occur when emission from hot plasma center is absorbed by the atoms in cooler boundary region having narrower spectral line shape. It is observed in spectrum as division of the emission line into two peaks. [**Paper II**] Usually self-absorption is something that is aimed to avoid as it hinders the quantitative analysis by disturbing the linear relation of measured emission intensity to analytic concentration. Atomic ground state transitions are most prone for self-absorption effect. Hence, transitions originating from higher energy levels are chosen to avoid the self-absorption in optically thick plasma. [258] However, this choice may compromise the LOD as the emission from these transitions requires higher excitation energy, i.e. collision or higher temperature, than resonance transitions, i.e., those involving the ground state. [**Paper IV**]

The quantitative analytical performance of LIBS measurement is often assessed by means of limit of detection (LOD). As LIBS is not an absolute method, it requires

Table 5.1 *The transition probabilities A_{ul}, lower and upper level energies E_j and the total angular momentum J_j for copper (Cu I) transitions that are used as example lines in this Thesis. [254]*

Wavelength (nm)	A_{ul} ($s^{-}1$)	E_l (eV)	E_u (eV)	J_l	J_u
324.75	1.395×10^8	0	3.82	1/2	3/2
327.40	1.376×10^8	0	3.79	1/2	1/2
327.98		1.64	5.42	3/2	5/2

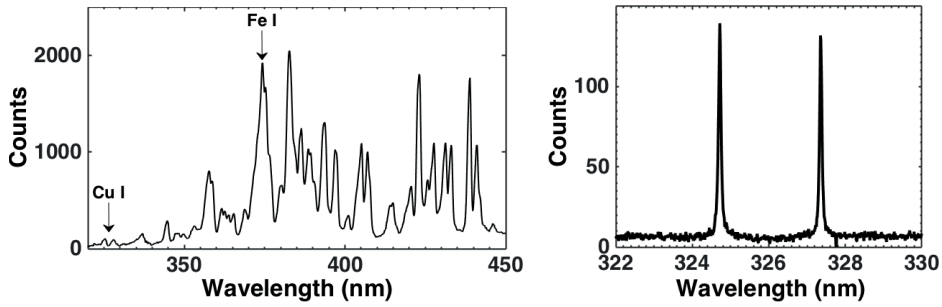

(a) (b)

Figure 5.3 *An example of (a) low resolution LIBS spectrum obtained from a sample containing copper and iron and (b) high resolution spectrum showing the copper (Cu I) emission lines.*

calibration that is obtained by analyzing the instrument response against tested calibration standards containing the desired analyte at known concentrations. Ideally the curve of growth, i.e. the calibration curve, is linear but in optically thick conditions the linearity is lost due to self-absorption compromising the sensitivity. In this Thesis, sensitivity refers to the slope of the linear part of a calibration curve. The slope of calibration curve is also related to LOD that is one of the most common figures-of-merit for a LIBS arrangement. LOD refers to the concentration when the instrument response equals to the background noise level and, thus, the atomic line emission cannot unambiguously be distinguished from the obtained spectrum. In this Thesis, the requirement for obtained atomic emission signal to be distinguishable is that it exceeds 3 times the background standard deviation s_{bi}. Hence, the LOD is defined as

$$\mathrm{LOD} = \frac{3s_{bi}}{b}, \tag{5.10}$$

where b is the slope of the linear part of calibration curve. [10,244] The importance of calibration standard and the actual sample similarity is constantly stressed as it has major impact on the reliability of the composed calibration. The sample properties gives rise to variation in plasma electron density and temperature, leading variation in collected emission intensity even though the analyte concentration would stay fixed. These variations as function of sample composition are called matrix effects. Due to the inherent randomness: laser pulse-to-pulse variation, matrix effects, and

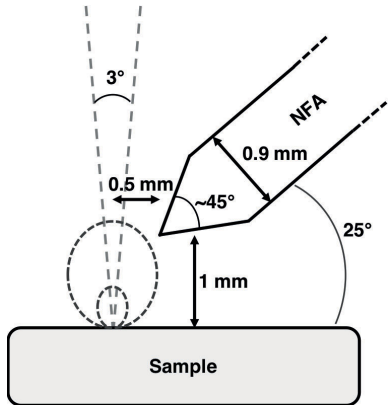

Figure 5.4 *Schematic of Near-Field Applicator (NFA) positioning on solid sample. The smaller and larger dashed circles represents approximate sizes of a laser-induced plasma and a microwave-maintained plasma, respectively. Adapted from* ***Paper II****.*

complex light-plasma interaction, LIBS signal fluctuates between successive laser pulses. Therefore LIBS signal is often acquired as an average of multiple spectra and relative standard deviation is used to describe the pulse-to-pulse repeatability of the signal formation. [10, 259]

5.2 Microwave Maintained Plasma

Despite the intriguing qualities of LIBS, simplicity, stand-off capability and information richness to mention a few, it has not become the standard for elemental analysis. This is mainly due to a lack of standard samples, requirement of calibration, and inadequate sensitivity for some applications. While other analytical techniques, such as ICP-mass spectrometry, can reach down to ppt limit of detection (LOD) [260], LIBS has been limited to LOD in ppm range. This hinders the applicability of LIBS for trace element analysis that is often under interest in different elemental detection applications. Multiple different methods have been demonstrated to improve the analytical performance of LIBS. These include double pulse LIBS (DP-LIBS) [261], spatial confinement [262], and microwave-assisted LIBS (MW-LIBS) [263]. In this section, closer look on MW-LIBS and microwave maintained laser-induced plasma plume is taken.

MW-LIBS is a fairly recent technique developed to improve the LOD and sensitivity of laser-induced plasma applications. It relies on coupling of microwave radiation to low electron density plasma. Two main methods to couple the microwave radiation to the plasma plume are microwave cavity [263–265] and microwave antenna coupling [266–269]. Microwave coupling solutions using cavity have shown extremely promising analytical performance enhancement factors reaching up to 800-fold improvement in signal levels. [264]. However, cavity solutions give away one of the main advantages of LIBS: the requirement of no or minimal sample preparation, as it requires sample placement and preparation for the cavity coupling. In that perspective, antenna coupling of microwave radiation seems more intriguing option. Previous studies using antenna coupled microwave radiation to enhance LIBS measurements have had difficulties to couple the microwave radiation at ambient conditions and have required low pressure [268, 269] or buffer gas [266] to operate. Introduction of Near-Field Applicator (NFA) [270] for microwave coupling has managed to overcome this problem. [271, 272] [**Paper II**, **Paper IV**] NFA is a tip antenna that creates high electric field to the near-field of the antenna. It is manufactured from rigid coaxial cable by removing the shielding and insulation layers for $1/4\ \lambda_{MW}$ length from the end of the cable. To increase the electric field confinement to the tip of the antenna, a grounding plate is inserted to the beginning of the shielded part of the cable. The laser pulse is focused to the proximity of the NFA tip to ignite the plasma as shown in Fig. 5.4. The microwave radiation is coupled to the charged particles in the plasma as it grows to the high electric field region of NFA. The microwave radiation can be produced by using magnetron or solid-state source. The microwave source used in the work described in this Thesis was a magnetron based system (Sairem) as high radiation power was initially desired. The microwave radiation was coupled to the NFA using a waveguide-to-coaxial adapter.

The most common microwave frequency used for MW-LIBS applications, and also used in this Thesis, is 2.45 GHz that has the corresponding critical plasma electron density n_c of 7.56×10^{10} cm^{-3}. In the initial laser-induced plasma, even at boundary areas, the ratio n_e/n_c is in order of 10^4-10^7 [249]. This leads to nearly complete reflection of microwave radiation at the plasma edge. In one dimensional case, MW reflection from air-plasma boundary with fixed electron density profile can be described with

$$R = \left| \exp\left(2ik_0 \int_{-\infty}^{Z_0} \sqrt{\varepsilon} dz \right) \right|^2, \tag{5.11}$$

where k_0 is the wavenumber of the microwave radiation and Z_0 is the the complex point where the complex dielectric function

$$\varepsilon = 1 - \frac{n_e}{n_c} \frac{1}{1 - i\nu_c/\omega} \tag{5.12}$$

equals zero. Here ν_c is the electron-neutral collision frequency defined as $\nu_c = 5 \times 10^9\ p_{torr}$. For exponential electron density profile

$$\frac{n_e}{n_c} = \exp\left(\frac{x}{l}\right), \quad l = n\left(\frac{dn}{dx}\right)^{-1} = L\frac{n_e}{n_c}, \tag{5.13}$$

the reflection of radiation energy can be written as

$$R = \exp\left[-4k_0 l \tan^{-1}\left(\frac{\nu_c}{\omega}\right) \right]. \tag{5.14}$$

As the laser-induced plasma expands rapidly and the electron density decreases, absorption of microwave radiation becomes more dominant in the microwave-plasma interaction. Absorption for fixed plasma density profile can be written as

$$A = 1 - \left| \exp\left(-ik_0 \int_0^x \sqrt{\varepsilon} dx \right) \right|^2. \tag{5.15}$$

For constant density plasma slab the absorption becomes

$$A = 1 - \exp\left(-\frac{\nu_c}{\omega} \frac{n_e}{n_c} \frac{k_0 \Delta}{\left[\left(1 + \frac{\nu_c^2}{\omega^2}\right) \left(1 + \frac{\nu_c^2}{\omega^2} - \frac{n_e}{n_c}\right) \right]^{1/2}} \right), \tag{5.16}$$

where Δ is the thickness of the slab. This shows that in case of $\nu_c/\omega \gg 1$ good absorption occurs for $(n_e/n_c)k_0 > c/\omega$. [273] The behavior of microwave-plasma

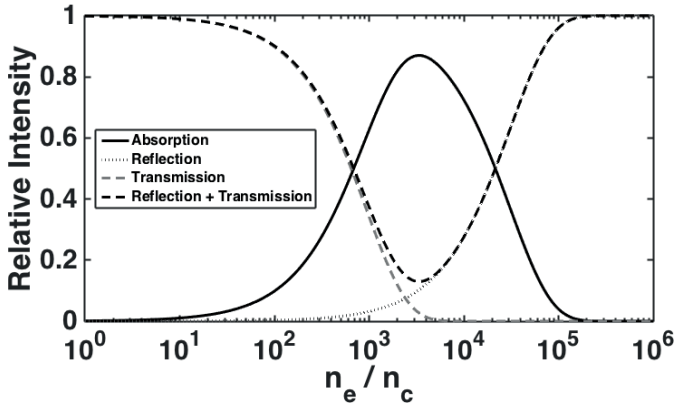

Figure 5.5 *Relative microwave-plasma interaction intensities as function of* n_e/n_c *with* $\omega = 2\pi f$, $f = 2.45$ *GHz;* $\Delta = 5$ *mm;* $L = 1 \times 10^{-7}$. *[273]*

interaction as function of n_e/n_c is plotted in Fig. 5.5. It can be seen that in this case the maximum absorption is achieved with $n_e/n_c = 3{\times}10^3$. The assumption is that this would be the state that the plasma is moving towards after microwave coupling. However, it has been shown that the electron density varies within microwave maintained plasma corresponding to the interference maximums and minimums of incoming microwave radiation and reflected microwave radiation. [274] Hence, the plasma electron density may be oscillating between reflection and absorption of the coupled microwave radiation.

Characteristics of the microwave maintained plasma properties are studied also experimentally as the detailed laser-induced plasma profile is not known well enough to provide full description based on theory. The electron density in an air-formed plasma is determined by studying the Stark broadening of hydrogen emission line at 656.27 nm. [275] The evolution of electron density in laser-induced plasma with NFA coupled microwave radiation is presented in Fig. 5.6. It can be seen that the electron density of microwave-maintained plasma plume levels on approximately 8×10^{15} cm^{-3} that corresponds to n_e/n_c value of $1{\times}10^5$. In the early stages of the laser-induced plasma, the electron density rises much higher reaching values in range of 10^{18} that are typical for laser-induced plasmas. Also the plasma temperature is unaffected in the early laser-induced plasma by the microwave radiation compared to case with no additional microwave radiation, as can be seen in Fig.5.7(a). However, as the microwave radiation is coupled to the

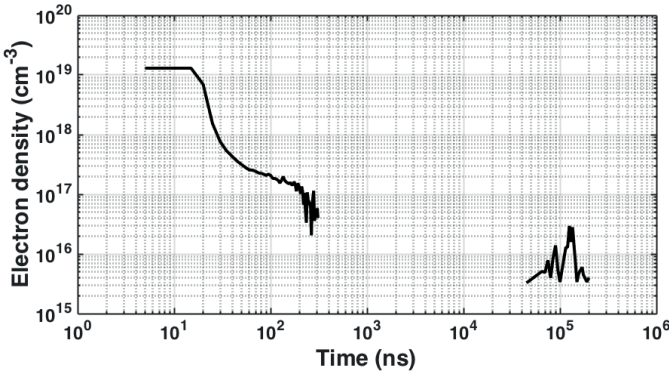

Figure 5.6 *Evolution of electron density in microwave maintained laser-induced plasma.*

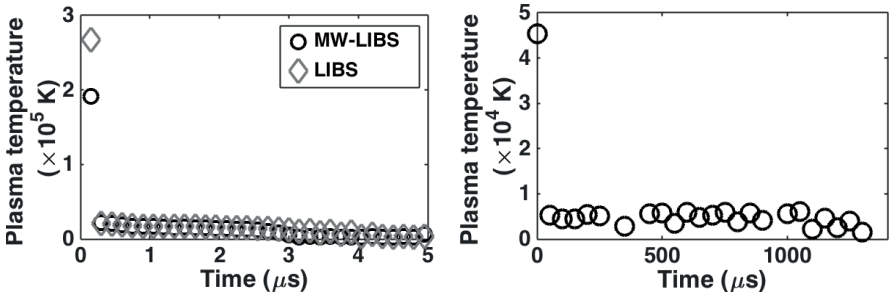

(a) (b)

Figure 5.7 *Plasma temperature (a) in the beginning of plasma evolution and (b) over the microwave maintained plasma lifetime.*

plasma plume, it provides external energy to the plasma species maintaining the temperature throughout the extended plasma lifetime, as shown in Fig.5.7(b). The plasma temperature is determined by comparing atomic oxygen emission line intensities at 777.54 nm and 822.18 nm. [276] These transitions originate from different energy levels, hence, their intensity ratio is proportional to the plasma temperature. In the work governed by this Thesis, no microwave reheating effect of the plasma is observed. Other studies have shown that the microwave radiation has the ability to reheat the plasma up to temperatures typical for early stages of laser-induced plasma. [269, 271] It would be in interest to study further what causes the reheating effect as it would be desirable to enable signal enhancement also for transitions originating from higher energy levels.

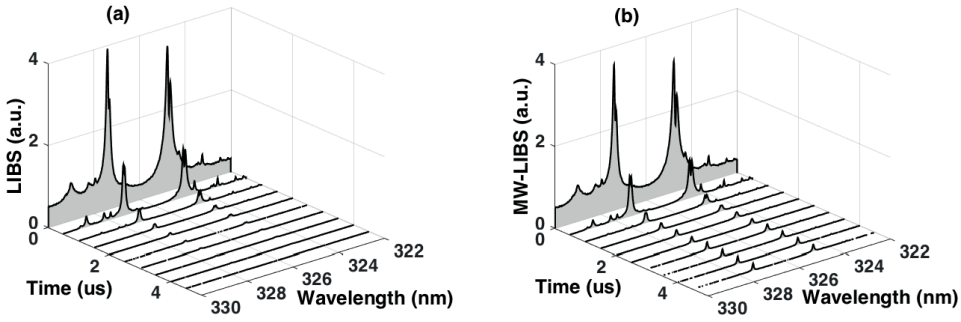

Figure 5.8 *Temporal evolution of a) LIBS and b) MW-LIBS spectral emission. Adapted from* ***Paper II****.*

Figure 5.8 shows temporal evolution of the emission intensity of plasma ignited on solid sample containing copper. The details of the copper emission lines are listed in Table 5.1. During the initiation and early stages of the plasma, the emission behavior is very similar with and without the presence of microwave radiation. However, when the microwave radiation is coupled to the plasma, it begins to provide external energy to the plasma plume and the persistence time of the atomic emission is prolonged. This is expected in perspective of the measured temperature behavior of the plasma. It is unfortunate that the microwave maintained plasma does not exhibit the reheating effect as it limits the signal enhancement effect mostly on ground state transitions. This limitation can be seen in Fig. 5.8 as the copper line at 327.98 nm, that is emitted from transition with lower energy level at 1.64 eV, is visible only in spectra collected during first 1 μs from laser pulse when the plasma has not yet cooled down.

Another interesting aspect in the copper spectrum shown in Fig. 5.8 is the line shape of the copper emission lines after the microwave coupling. The emission line shapes are affected significantly less by self-absorption effect than the spectral lines collected before the plasma reaches electron density lower than the microwave coupling threshold. And indeed, it is observed that MW-LIBS signal is less affected by self-absorption than LIBS signal as shown in Fig. 5.9. Reduced self-absorption may be due the increased size of the plasma. [270] [**Paper II**] This leads to reduced analyte number density inside the plasma that decrease the absorption probability of light emitted from inner parts of the plasma. The absence of self-reversal effect in microwave coupled plasma is an indicator of plasma temperature homogeneity as

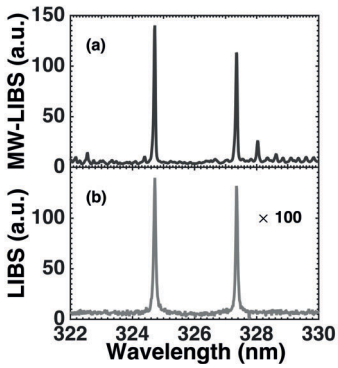

Figure 5.9 *Spectra with (a) MW-LIBS and (b) conventional LIBS of solid sample containing 0.3 % copper. The laser energy was 0.8 mJ/pulse and the microwave power was 1.2 kW. The delayed time and gate width were (a 500 ns and 800 μs, and (b 300 ns and 10 μs, respectively. The spectra were accumulated over 300 laser shots. Note that the spectrum recorded in LIBS has been multiplied with a factor of 100 to show the spectra in the same intensity scale. Adapted from* ***Paper II****.*

it originates from the temperature difference between the emitting and absorbing species. [10]

The ability of microwave radiation to prolong the lifetime of laser-induced plasma leads to extended time window for signal integration. This is the main reason for improved analytical performance of MW-LIBS in terms of LOD compared to conventional LIBS. Essentially, the plasma lifetime is determined by the duration of microwave injection. Pulsed injection of microwave radiation to the plasma is mandatory to avoid overheating of the waveguide-to-coaxial adapter and NFA tip. Hence, the signal integration time is limited only by the microwave pulse length. Typical pulse length and signal integration time have been 1.3 ms and 0.8 ms, respectively. [**Paper II**, **Paper IV**] This is well beyond the integration times in order of 10 μs that are typical for LIBS measurements. Microwave pulse is launched before the laser pulse to ensure that the microwave radiation is reaching the laser-induced plasma. The timing scheme of MW-LIBS measurement is sketched in Fig. 5.10. The microwave pulse length has further been extended to few milliseconds by optimized NFA design [270] that enabled the use of lower microwave peak power. Hopefully, the extended microwave-assisted plasma can be demonstrated in the near future.

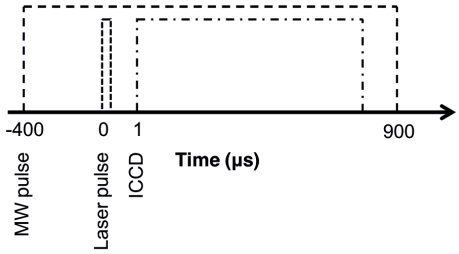

Figure 5.10 *An example of the MW-LIBS signal acquisition timing scheme. The microwave pulse is launched before the laser pulse to ensure maximal microwave radiation intensity while plasma ignition. As the plasma lifetime is limited only by the temporal width of the microwave pulse, plasma emission signal acquisition can be extended to cover whole microwave pulse duration after the plasma ignition.*

5.3 MW-LIBS Figures of Merit

LIBS is well suited for qualitative elemental monitoring scheme. However, often the elemental monitoring applications require also quantitative information. As LIBS is not an absolute method due to a lack of comprehensive understanding of light-matter interactions, light-plasma interactions, and plasma dynamics, traditionally quantitative LIBS detection requires calibration. Hence, a calibration on solid samples was carried out to clarify the MW-LIBS figures of merit. Copper (Cu I) transition $4s^2S_{1/2}$ - $4p^2P^0_{1/2}$ that emits light at 324.75 nm was chosen to determine the enhancement factor of NFA injected MW-LIBS. Copper was chosen as sample element as it is an economically important element with extensive use in consumer products and industry. Due to its economical impact, it is of interest to optimize copper mining process and ore classification. [277] Solid sample was chosen also to obtain more comparable enhancement factor with other enhancement methods, as solid target is much more commonly used than gas or liquid phase targets.

The experimental parameters: lens-to-sample distance, laser pulse energy, spectrometer camera gate delay, and gate width, were determined to obtain highest signal-to-noise ratio with LIBS measurement. [**Paper II**] The parameters were kept constant for corresponding MW-LIBS measurements except the gate width that was extended to cover the whole microwave-maintained plasma lifetime. The microwave power was chosen to be 1.2 kW as the higher microwave power

would expand the plasma too large to be collected efficiently with the signal collection arrangement. [**Paper II**]

Calibration samples for copper detection were prepared by wet impregnation diluting $Cu(NO_3)_2$ and Al_2O_3. The produced sample powder was compressed into round plastic molds and binded using spray adhesive. Blank samples were produced in a similar manner from pure Al_2O_3. The samples were placed on rotating mount to reduce pitting effect caused by the laser pulse. Each laser shot hit a new spot on the sample surface and, hence, the lens-to-sample distance remained constant and the ablation conditions were maintained homogeneous throughout the measurement.

The obtained calibration curves for conventional LIBS and for MW-LIBS for copper in Al_2O_3 matrix are presented in Fig. 5.11. The MW-LIBS curve has evidently steeper slope indicating better sensitivity and improved LOD. The LOD was determined using Eq. 5.10 for LIBS and MW-LIBS to be 760 ppm and 8.1 ppm, respectively. Hence, an enhancement factor of 93 was achieved. However, it is worth mentioning that when laser pulse energy was reduced closer to the ablation threshold, enhance factor exceeding 100 was obtained. It was found that it requires only ignition of the plasma and microwave radiation would be able to deposit external energy in it extending the plasma lifetime. This is given that the NFA was placed close enough to the ignited plasma front. [**Paper II**] The achieved enhancement factor with intriguing potential to reduce self-absorption effects presented in section 5.2 are promising demonstrations of the abilities of novel NFA injected MW-LIBS. Its clear advantages compared with other MW-LIBS approaches are that it is capable to extend the laser-induced plasma lifetime in ambient conditions and it does not require extensive sample preparation. Hence, its applicability in different disciplines is much greater than the other methods. Next section presents how NFA injected MW-LIBS benefits studies on high-temperature chemistry during thermal conversion of biomass.

5.4 Flame Calibration and MW-LIBS for Elemental Release Monitoring

LIBS technique has been widely applied also for combustion research. Recently, LIBS has been increasingly used to measure equivalence ratios in different types of flames [278–285] and in spark-ignited engines [286–288]. Equivalence ratio is an important measure describing pollution formation, combustion performance, and if

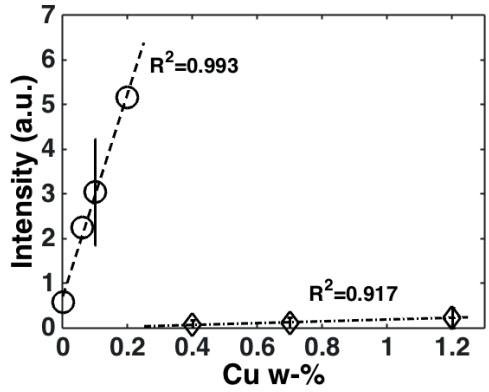

Figure 5.11 *Calibration curves of the copper (Cu I) 324.75 nm line obtained with MW-LIBS (circles) and conventional LIBS (diamonds). The laser energy was 2.5 mJ and the microwave power was 1.2 kW. The gate width was 800 μs and 10 μs in MW-LIBS and conventional LIBS, respectively, while the delay time was kept constant 1 μs. The results are averaged over 300 single-shot measurements and typical standard deviations are shown. Adapted from* ***Paper II****.*

the mixture is combustible in the first place. LIBS has also been demonstrated for temperature mapping in laboratory scale flame. The temperature measurements have been based on temperature dependency of breakdown threshold [289] or temperature dependency of acoustic emission of the laser-induced plasma. [290]

LIBS has proven to be a useful tool also to study elemental release during thermal conversion of solid fuels. As discussed in Chapter 2, most solid fuels contain alkali elements that, even in small concentrations, may cause extensive problems in power-plant operation. LIBS is capable to deliver information on total temporal release behavior of alkali elements regardless on the form they are released as from the fuel. The previous studies have been concentrating to lignite [291], woody biomass [48, 292], and coal [293] that, in general, are fairly low in alkali elements. The main reason has been the lack of reliable calibration method for higher alkali concentrations. Therefore, a novel burner and seeding design was required to extend the flame calibration range to concentrations relevant for greater number of biomass fuels.

Previous LIBS studies in flame have been carried out using laminar premixed burner with two main parts: the central jet and the annular co-flow. The central jet has been fed with a pre-mixed fuel and air that also carried the seed droplets. The droplets were produced using ultrasonic nebulizer that was placed into a salt solution bath

connected to a droplet reservoir. The air-fuel mix was flown through the droplet reservoir to the burner. The seed alkali concentration was varied through different concentrations of salt solutions. [48,291,293] This approach does not allow variation in the gas flow as it would alter the flame conditions. Also, the nebulizer does not function well with high salt content solutions. Hence, the calibration range remains limited. In the novel burner and seeding scheme presented in **Paper IV**, the seeding droplets were carried into the center of the flame through a separate seed jet as shown in Fig. 5.12. The carrier gas was pre-mixed air and fuel that had equivalence ratio of 0.78 that was the same as the main flow to the burner jet. This allowed flexible variation of flame analyte concentration by altering the seed flow without affecting the flame characteristics. The constant flame equivalence ratio is essential for successful flame calibration for alkali elements. [294] The used equivalence ratio of 0.78 lead to flame temperature of about 1500 K at the measurement height. When the carrier gas flow through the seed droplet reservoir was increased above 110 mL/min, the droplet depletion was observed to be faster than the nebulizer droplet generation. Hence, the nebulizer efficiency became the limiting factor for the flame calibration restraining the seeding flow rates to range 10 - 100 mL/min. It was also noticed that the nebulizer efficiency is salt solution dependent, therefore the calibration ranges varies from element to element. The seeding rate SR_a of an alkali to the flame is given as

$$SR_a = A \cdot Q_{neb} \cdot SC, \tag{5.17}$$

where A is the mass loss constant for the solution, Q_{neb} is the seeding flow rate (mL/min), and SC is the alkali compound solution concentration (g/mL) in the nebulizer tank. The mass loss constant was determined by weighing the nebulizer tank before and after 24 h nebulization with constant carrier gas flow. Hence, the average analyte concentration C_a (ppm) in a horizontal plane of the flat flame can be give as

$$C_a = \left(\frac{n \cdot SR_a}{M_a}\right) / \left((Q_{fuel} + Q_{air} + Q_{neb})\frac{p}{RT}\right) \times 10^6, \tag{5.18}$$

where n is the atomic number of the target atomic element in the compound, M_a (g/mmol) is the molecular weight of the analyte compound, Q_{fuel} is the flow rate of the

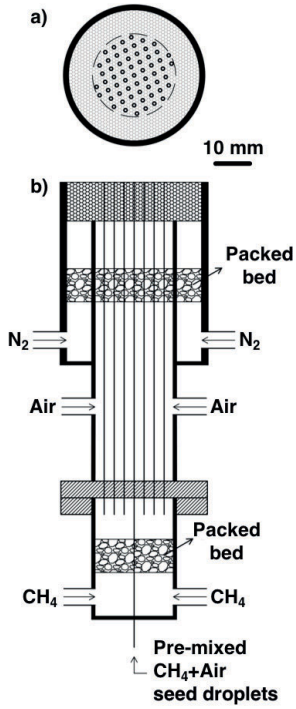

Figure 5.12 *Schematic presentation of the novel burner design. a) top view, b) side view. Adapted from* ***Paper IV****.*

fuel, in this case CH_4, Q_{air} is the flow rate of the air, p is the atmospheric pressure, R is the universal gas constant, and T is the temperature in standard condition. [**Paper IV**]

The novel seeding arrangement through a jet in the center of the burner caused the calibration flame to have analyte distribution in the horizontal plane. As the Eq. 5.18 provides the average analyte concentration in the horizontal plane, the analyte distribution had to be taken into account when delivering the calibration values. The distribution showed in Fig. 5.13 was measured using LIBS. The obtained signal intensity data points from sodium expressed a Gaussian distribution that was assumed as diffusion is the main spreading mechanism of the molecules in the flame. The obtained distributions were used to correct the calibration concentration values in the measurement point that was at the center of the flame 22 mm above the burner surface.

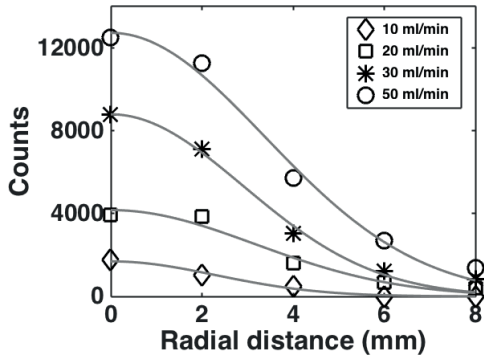

Figure 5.13 *Seed element distribution in the flame with various carrier gas flows. The distribution is measured using LIBS and sodium is used as sample element. Adapted from* ***Paper IV****.*

The ground state transitions of sodium, potassium, and calcium, that were under interest in this study, are prone to self-absorption. Self-reversal was also a major issue as the plasma emission propagated through the surrounding flame that is lower in temperature than the emitting plasma and contained the atomic analyte element. Hence, a simple spectrum post-processing scheme was employed to mitigate the adverse self-absorption effects for the quantitative measurement. The recorded spectrum $S(\omega)$ was assumed to be a product of two consecutive processes: atomic emission by the excited atoms $H(\omega)$ and atomic absorption $G(\omega)$ by the surrounding atoms on ground state

$$S(\omega) = H(\omega)G(\omega) = \frac{I}{1 + \left(\frac{2(\omega - \omega_0)}{\gamma_H}\right)^2} \exp\left(-\frac{\alpha L}{1 + \left(\frac{2(\omega - \omega_0)}{\sigma_G}\right)^2}\right), \tag{5.19}$$

where I is the intensity at the emission maximum, γ_H and σ_G are the full width at half maximum of emission and absorption profile, respectively, and αL is the absorbance. The nonlinear least squares fit of Eq. 5.19 was fitted to measured spectrum using four independent variables I, αL, γ_H, and σ_G. From the best fit, $H(\omega)$ was extracted and the integrated value of it was used for calibration. The integrated values of $H(\omega)$ exhibited extremely good linearity against the seeded analyte concentration in contrast to nonlinear behavior of integrated values of non-fitted LIBS spectra. [**Paper IV**]

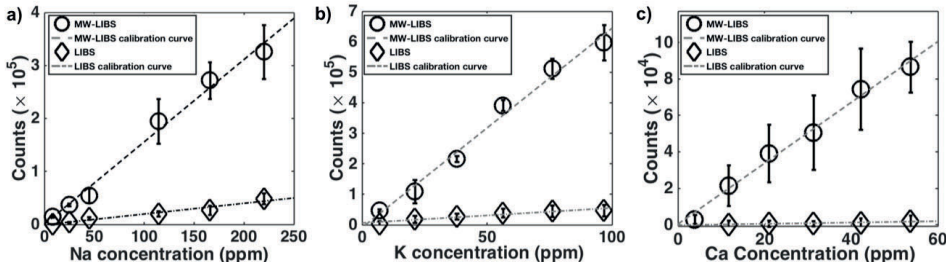

Figure 5.14 *The measured calibration curves for a) Na, b) K and c) Ca. Error bars represent the standard deviation of 200 measured laser shots. Adapted from* ***Paper IV****.*

The measurement parameters, laser pulse energy and spectrometer camera gate width and delay, were established to optimize the LIBS signal-to-noise ratio for each element. The parameters were kept constant for MW-LIBS measurement but the gate width was extended to 1 ms to cover the microwave-maintained plasma lifetime and gain the benefits of microwave enhancement. In addition, for MW-LIBS analysis, the spectrometer camera gain factor was reduced from 100 to 1 compared to LIBS measurement to avoid detector saturation in high concentration cases. The obtained sodium, potassium, and calcium calibration curves for LIBS and MW-LIBS using average of 200 laser shots are shown in Fig. 5.14. The slopes and R^2 factors of the fitted curves are collected to Table 5.2 with LODs estimated using Eq. 5.10. The MW-LIBS calibration values exhibit improved linearity compared to LIBS values. This maybe due to increased homogeneity of plasma emission [**Paper II**] that leads to more consistent self-absorption behavior in plasma and flame that is favorable for Eq. 5.19 as it consists only one absorption line profile. The system response was up to 60-fold more sensitive for MW-LIBS compared to LIBS that can be observed as improved LOD. In addition, the LODs of sodium and potassium expressed 3-fold improvement compared to previously reported values. [293]. However, it is worth reminding that the spectrometer gain value was set to minimum meaning compromised LOD and, hence, it could be significantly improved. The LOD was sufficient for all target elements to study their temporal release behavior form biomass fuels and the signal saturation was observed to be the limiting factor for the method's dynamic range. [**Paper IV**]

The obtained calibration curves were applied to monitor temporal elemental release during thermal conversion of biomass fuels. Fuels were milled and pressed to pellets with a diameter of 2.5 mm. The pellets were set to the center of the

flame 5 mm above the burner surface using platinum wire. The release measurement was conducted at 14.5 mm above the sample, that is >5 times the particle diameter, to avoid the flame disturbance caused by the particle. [292, 293] High spectral resolution was required to enable the use of emission line fitting method, hence, sodium, potassium, and calcium measurements were performed separately. It was observed that poplar samples behaved the most consistently in the flame and in terms of the release patterns, so it was chosen to be the example biomass fuel to demonstrate MW-LIBS measurement in flame.

The obtained elemental release patterns of sodium, potassium, and calcium during thermal conversion of poplar are presented in Fig. 5.15. The release patterns of sodium and potassium resemble the previously reported release behavior from woody biomass. [48, 292, 293] However, in this case the monitoring range is extended to cover also the release from higher sodium content poplar. The potassium release is significantly higher than sodium as was expected based on elemental analysis presented in Table 2.1. Towards the end of the char burning, potassium release exceeds the calibration range. Therefore, full confidence for the absolute values assigned for potassium release during char burning cannot be granted. However, the trend is clear that the end of char burning exhibits the highest release rate of potassium. This can be explained by the stoichiometric excess of potassium in comparison to chlorine, as discussed in Chapter 2. The sample is completely dechlorinated during devolatilization leaving the remaining potassium to react with the carboxyl groups. As the char temperature increases, potassium is released due to high-temperature dissociation as atomic potassium or as hydroxides providing sufficient partial pressure of H_2O. Calcium release is detected only during the devolatilization stage. Low calcium release was expected as it is known to mainly remain in the bottom ash. [24] Even during the devolatilization, calcium release rate barely exceeded the MW-LIBS LOD.

Table 5.2 *The obtained calibration curve slopes and corresponding detection limits for quantitative monitoring of sodium, potassium, and calcium.*

	LIBS				MW-LIBS		
Element	Slope (Counts/ppm)	R^2	LOD (ppb)	LOD (ppb)	Slope (Counts/ppm)	R^2	LOD (ppb)
Na	407.3	0.95	130	29 [293]	3108.8	0.98	10
K	490.8	0.91	410	72 [293]	6536.2	0.99	19
Ca	35.9	0.94	950		1668.6	0.99	16

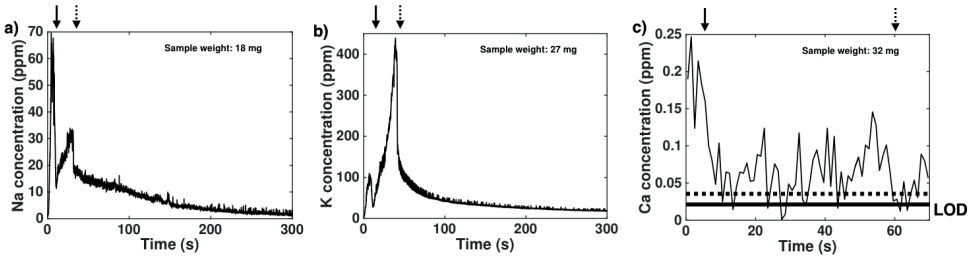

Figure 5.15 *The recorded release patterns of a) sodium, b) potassium, and c) calcium during thermal conversion of a poplar pellet. The flame equivalence ratio was 0.78. Time-traces are measured using MW-LIBS utilizing the spectral fitting method to extrapolate the calibration to higher concentrations. The time trace of Ca release is averaged over 20 shots, i.e. for 2 s, and cut to cover only the devolatilization and char burning to show the release during devolatilization. The solid arrow and dashed arrow show the end of the devolatilization stage and the end of char burning stage, respectively. Solid line in c) depicts the LOD for Ca measurement and the dashed line shows the measurement uncertainty of LOD. Adapted from* ***Paper IV****.*

5.5 Comparison of MW-LIBS to other enhancement techniques

In this section, a brief introduction over enhancement techniques applied to improve analytical performance of LIBS is given and their figures of merit are compared with NFA injected MW-LIBS. The comparison is done by means of enhancement factor that is often given in other comparisons to conventional LIBS. Enhancement factor is a more meaningful comparison parameter than e.g. absolute LOD or signal-to-noise ratio as they depend also on experimental parameters, such as laser pulse energy, lense-to-sample distance, and sample type. In literature, enhancement factor refers some times to improvement in signal-to-noise ratio, improvement in LOD, or increment in signal level. In the following review, the enhancement factors reported are the ones reported in the cited literature, hence, reader needs to check which parameter in particular is in question. However, the enhancement factor does not vary much between different definitions as they are linked to each other. Therefore, comparison can be done using the factors reported.

Generally, the enhancement techniques aim to overcome the difficulties in quantitative analysis, i.e. lack of sensitivity or accuracy. For many of them, the main goal is to enhance signal-to-noise ratio that leads to improved LOD. High LOD and low sensitivity are in many cases the limiting factors for success of LIBS.

The common factor in the enhancement methods is that, in addition to a laser pulse, external energy is applied to either the sample or the laser-induced plasma. This external energy increases the excited atomic population, leading to an increase in atomic line emission from the plasma. The increase may be a result of increased plasma temperature, increased electron density, or extended plasma lifetime.

The LIBS emission signal is collected to the spectral detector from a limited spatial volume. Hence, it is unfavorable that the plasma plume expands outside this volume as part of radiative energy is lost. **Spatial confinement** is a relatively simple and inexpensive method to improve the signal collection efficiency and, therefore, the sensitivity of LIBS. Spatial confinement can be implemented by using a physical obstacle or a magnetic field. Physical confinement has been carried out using cylindrical [295, 296] or hemispherical [297, 298] chamber geometries surrounding the plasma. Physical confinement has shown enhancement factors from 2 to 10 depending on target element. Also a slight improvement in calibration linearity has been observed that improves the reliability of quantitative analysis of unknown samples. Magnetic field confinement has shown similar enhancement factors. [299] However, combination of obstacle and magnetic field confinement achieved enhancement factor of up to 24. [262] Spatial confinement has been used also in combination with techniques presented later in this section improving the repeatability of spark discharge assisted LIBS measurement [300] and further improving double pulse LIBS sensitivity [301].

One of the most used LIBS enhancement techniques is **Double Pulse LIBS (DP-LIBS)**. DP-LIBS aims to improve coupling between ablated material and laser irradiation to increase the efficiency of atomic excitation. The geometrical alignment of the laser pulses is usually collinear or orthogonal. [10, 302] The first laser pulse is used to pre-heat or ablate the target sample and, in some cases, ignite the plasma. The second pulse, launched $\sim$1 µs after the first pulse, is absorbed to the plasma reheating it and, hence, increasing the number of excited species. The reheating effect has been found to improve the LIBS signal-to-noise ratio with enhancement factors varying from 2 to 300. [261, 302–304] In addition to signal enhancement, varying other measurement parameters, such as pulse durations, wavelengths, and energies, the plasma and ablation characteristics can be altered. For example, signal enhancement enables the use of lower pulse energies that leads to reduced damage on sample surface. [10, 302]

Spark Discharge-Assisted LIBS (SD-LIBS) is based on similar reheating effect as in DP-LIBS but, instead of another laser pulse, the external energy is deposited to the plasma by electrical spark discharge. The laser-induced plasma is created between tungsten electrodes capable to carry ∼10 kV voltage. The spark discharge is launched when the charged particles of the plasma reach the electrode gap lowering the discharge threshold. SD-LIBS has presented enhancement factors up to 400. [305, 306] High enhancement factor has enabled the use of lower laser pulse energy, reducing the damage on the sample material. Also, the use of spark discharge has reduced the shot-to-shot plasma fluctuation, improving the precision of quantitative analysis. However, despite the promising results, SD-LIBS has not become standard LIBS enhancement method. This may be due to the requirement of relatively high voltages and low repetition rate of the discharge. [10, 305]

In addition, a flame can be used to pre- and re-heat sample surfaces and the plasma as a flame is also a low ionization level plasma. In **Flame-Assisted LIBS (FA-LIBS)**, flame is set close to a sample surface and the laser-induced plasma is generated to the blue outer envelope of the flame. FA-LIBS has reported to exhibit 4-fold signal improvement and 60 % narrower spectral lines that implies improved spectral resolution and sensitivity. [307] Furthermore, use of micro-torch, instead of a pre-mixed flame, has shown 5-fold enhancement factors compared to conventional LIBS signal. [308]

MW-LIBS approach for analytical enhancement of LIBS lasts well in comparison with other introduced enhancement methods. Selected enhancement methods and corresponding enhancement factors have been collected to Table 5.3 for easy comparison. The enhancement factors obtained with NFA injected MW-LIBS are some of the highest presented in the literature. In addition to spectral detection of elements, NFA injected MW-LIBS has been demonstrated as a imaging technique called Microwave-Assisted Laser-Induced Plasma Imaging (MW-LIBEI) that further improved 14-folds the sensitivity of elemental indium detection by microwave-assisted plasma on solid sample. [272] However, due to the radiative leakage through the imaging filter, the LOD was slightly poorer than that of MW-LIBS. Despite the higher LOD, this was a powerful demonstration of sensitive and cost effective single element detection enabled by the extended laser-induced plasma lifetime. MW-LIBS in general has shown extremely effective sensitivity improvements and has been able to drag LOD's to 10 ppm range and below. MW-LIBS is also overall a fairly inexpensive method to improve LIBS analytical

Table 5.3 *Examples of enhancement factors achieved with selected LIBS signal enhancement methods*

Element	Sample	Method	Enhancement factor	LOD (ppm)	Reference
Cr I	Metal alloy	Spatial confinement	24		[262]
Al I	Metal alloy	DP-LIBS	80		[261]
Cu I	Metal alloy	DP-LIBS	30		[261]
Fe I	Ceramic	CO_2 DP-LIBS	119		[304]
Al II	Metal alloy	SD-LIBS	50-400		[305]
Al I	Metal alloy	Flame assisted	4		[307]
Na I	Ceramic	Enclosed MW cavity	33		[263]
Cu I	Soil	Enclosed MW cavity	23	30	[265]
Gd II	Gd_2O_3	Loop MW antenna	32	2	[268]
Gd II	Gd_2O_3	Loop MW antenna	50		[269]
In I	Liquid	NFA injected MW	11	10	[271]
Cu I	Cu/Al_2O_3	NFA injected MW	93	8.1	**Paper II**
K I	Flame	NFA injected MW	60	0.019	**Paper IV**

performance as microwave sources with power levels required by MW-LIBS are well available and very affordable.

6

Conclusion

Concern for environmental impacts associated with traditional methods of heat and power generation and recent changes to grid requirements provide motivation for development of novel combustion concepts and controls. High-temperature chemical reaction kinetics play a crucial role in thermal heat and power production. Knowledge and control of these kinetics are the key to improved sustainability and profitability of the combustion industry. In this Thesis, two optical methods were developed and applied to online monitor high-temperature chemistry and conditions during thermal conversion of biomass fuels. Collinear Photofragmentation and Atomic Absorption Spectroscopy (CPFAAS) enable measurement of fragment reaction kinetics after the photofragmentation event. The new insight to atomic potassium kinetics with O_2 at high-temperature conditions enabled online temperature and O_2 concentration monitoring. Also, a new approach to enhance analytical performance of Laser-Induced Breakdown Spectroscopy (LIBS) was introduced. Near-Field Applicator (NFA) injected Microwave-Assisted LIBS (MW-LIBS) was demonstrated in ambient conditions and further applied to monitor elemental release during thermal conversion of biomass fuels. Furthermore, a novel burner seeding design was presented which enables MW-LIBS flame calibration over a greater range of element concentrations.

CPFAAS has proven to be one of the most versatile techniques for monitoring high-temperature chemistry. CPFAAS enables simultaneous and quantitative monitoring of several alkali species, gas temperature, and O_2 concentration. [195]

[**Paper III**] In addition, the method is scalable from laboratory-scale reactors to full-scale power plants that only few methods described in Chapter 3 can offer. The CPFAAS drawbacks are that it relies on UV dissociation that becomes limiting factor in highly scattering media, and that the probe beam may saturate in high concentration conditions. The latter limitation could be mitigated by combining CPFAAS with Tunable Diode Laser Absorption Spectroscopy (TDLAS). As TDLAS is lacking the spatial sensitivity and ability to monitor alkali chlorides and alkali hydroxides, but can operate in higher concentrations and has broader molecule portfolio than CPFAAS, the combination of CPFAAS and TDLAS could provide a powerful method for gas phase diagnostics.

The applications of CPFAAS are not limited to combustion environments as reaction kinetics are under interest in various disciplines of science and industry. By altering the fragmentation and probe beam wavelengths, the reaction kinetics could be probed also in atmospheric chemical reactions, for example. The in-situ chemical kinetics monitoring with CPFAAS is based on observation of the reacting species after the existing chemical equilibrium has been distracted with the fragmenting laser pulse. This provides truly unique information on how the system has reached its prevailing state. [**Paper I**] Other techniques used for reaction kinetic monitoring, such as TDLAS [80] and Planar Laser-Induced Fluorescence (PLIF) [117], monitor essentially the existing state of the system without taking stand on how it has been reached and, therefore, they are lacking behind in information richness.

The work done in this Thesis was the first demonstration of antenna injected MW-LIBS at ambient conditions. The development curve of the novel approach for microwave assisted laser-induced plasma spectroscopy was presented in Chapter 5. The key element for success was the innovation of new NFA that created dense electric field to the proximity of the antenna tip. [270] Detection limit enhancement factor of 93 for copper detection was achieved in comparison to conventional LIBS. [**Paper II**] MW-LIBS showed great potential to be applied also to elemental detection in flames as it improved the detection limit of trace elements and, on the other hand, reduced adverse self-absorption effects in high concentration conditions. To harness MW-LIBS's potential for flame studies, a novel burner design for flame calibration was required. The new seeding scheme presented in Chapter 5 allowed broader calibration range than the previous seeding

methods. MW-LIBS was demonstrated with sodium, potassium, and calcium monitoring during thermal conversion of poplar. [**Paper IV**]

The demonstration of MW-LIBS at ambient atmospheric conditions in this Thesis is a major step towards more sensitive online elemental analysis. MW-LIBS enable the improvement of the analytical performance, i.e. limit of detection and sensitivity, in multiple applications. MW-LIBS has already shown to work with solid, liquid, and gas phase samples with substantial enhancement factors [**Paper II**, **Paper IV**] [271] opening the prospects on many fields of science and industry. However, more work needs to be done to understand thoroughly the nature of microwave-plasma interaction. The previously reported plasma reheating effect [269, 271] was not observed in the work done premising this Thesis. This has limited the signal enhancement effect only to transitions originating from low energy levels. Understanding and control of the plasma reheating would greatly benefit the MW-LIBS analysis as it would open prospects to measure chlorine, for example, that has remained a challenge for LIBS measurements. Longer plasma emission lifetime that MW-LIBS offers enables more affordable and compact signal acquisition approaches. [272] On the other hand, if costs are not the issue, longer signal integration time may improve the signal-to-noise ratio of high resolution measurements. These, in addition to improvement in detection limits, further increases the attractiveness of MW-LIBS.

References

[1] E. Comission, Communication from the Commission to the European Parliament, the Council, the European Economic and Social Committee and the Committee of the Regions Energy Roadmap 2050 /* COM/2011/0885 final */ (Brussels, 2014).

[2] M. Hupa, O. Karlström, and E. Vainio, "Biomass combustion technology development–it is all about chemical details," Proceedings of the Combustion Institute **36**, 113–134 (2017).

[3] S. G. Sahu, N. Chakraborty, and P. Sarkar, "Coal-biomass co-combustion: an overview," Renewable and Sustainable Energy Reviews **39**, 575–586 (2014).

[4] P. McKendry, "Energy production from biomass (part 1): overview of biomass," Bioresource technology **83**, 37–46 (2002).

[5] K. Kohse-Höinghaus, R. S. Barlow, M. Aldén, and J. Wolfrum, "Combustion at the focus: laser diagnostics and control," Proceedings of the Combustion Institute **30**, 89–123 (2005).

[6] M. Bolshov, Y. A. Kuritsyn, and Y. V. Romanovskii, "Tunable diode laser spectroscopy as a technique for combustion diagnostics," Spectrochimica Acta Part B: Atomic Spectroscopy **106**, 45–66 (2015).

[7] R. P. Lucht, "Applications of laser-induced fluorescence spectroscopy for combustion and plasma diagnostics," in "Laser Spectroscopy and Its Applications," (Routledge, 2017), pp. 623–676.

[8] T. Sorvajärvi, J. Saarela, and J. Toivonen, "Optical detection of potassium chloride vapor using collinear photofragmentation and atomic absorption spectroscopy," Optics letters **37**, 4011–4013 (2012).

[9] D. W. Hahn and N. Omenetto, "Laser-induced breakdown spectroscopy (LIBS), part I: review of basic diagnostics and plasma–particle interactions: still-challenging issues within the analytical plasma community," Applied spectroscopy **64**, 335A–366A (2010).

[10] D. W. Hahn and N. Omenetto, "Laser-induced breakdown spectroscopy (LIBS), part II: review of instrumental and methodological approaches to material analysis and applications to different fields," Applied spectroscopy **66**, 347–419 (2012).

[11] L. Zhang, C. C. Xu, and P. Champagne, "Overview of recent advances in thermo-chemical conversion of biomass," Energy Conversion and Management **51**, 969–982 (2010).

[12] J. C. Wurzenberger, S. Wallner, H. Raupenstrauch, and J. G. Khinast, "Thermal conversion of biomass: Comprehensive reactor and particle modeling," AIChE Journal **48**, 2398–2411 (2002).

[13] Y. Yang, V. Sharifi, and J. Swithenbank, "Effect of air flow rate and fuel moisture on the burning behaviours of biomass and simulated municipal solid wastes in packed beds," Fuel **83**, 1553–1562 (2004).

[14] B. Jenkins, L. Baxter, T. Miles Jr, and T. Miles, "Combustion properties of biomass," Fuel processing technology **54**, 17–46 (1998).

[15] G. Lu, Y. Yan, S. Cornwell, M. Whitehouse, and G. Riley, "Impact of co-firing coal and biomass on flame characteristics and stability," Fuel **87**, 1133–1140 (2008).

[16] R. Flagan and A. Sarofim, "Comments on the paper by WT Reid," Progress in Energy and Combustion Science **10**, 171–175 (1984).

[17] C. R. Shaddix and A. Molina, "Particle imaging of ignition and devolatilization of pulverized coal during oxy-fuel combustion," Proceedings of the Combustion Institute **32**, 2091–2098 (2009).

[18] A. Khan, W. De Jong, P. Jansens, and H. Spliethoff, "Biomass combustion in fluidized bed boilers: Potential problems and remedies," Fuel processing technology **90**, 21–50 (2009).

[19] O. Karlström, A. Brink, E. Biagini, M. Hupa, and L. Tognotti, "Comparing reaction orders of anthracite chars with bituminous coal chars at high temperature oxidation conditions," Proceedings of the Combustion Institute **34**, 2427–2434 (2013).

[20] S. Dasappa, P. Paul, H. Mukunda, and U. Shrinivasa, "Wood-char gasification: experiments and analysis on single particles and packed beds," in "Symposium (International) on combustion," (Elsevier Science, 1998), 1, pp. 1335–1342.

[21] T. Mani, N. Mahinpey, and P. Murugan, "Reaction kinetics and mass transfer studies of biomass char gasification with CO_2," Chemical Engineering Science **66**, 36–41 (2011).

[22] O. Karlström, A. Brink, and M. Hupa, "Desorption kinetics of CO in char oxidation and gasification in O_2, CO_2 and H_2O," Combustion and Flame **162**, 788–796 (2015).

[23] Y. Huang, X. Yin, C. Wu, C. Wang, J. Xie, Z. Zhou, L. Ma, and H. Li, "Effects of metal catalysts on CO_2 gasification reactivity of biomass char," Biotechnology advances **27**, 568–572 (2009).

[24] S. V. Vassilev, D. Baxter, L. K. Andersen, and C. G. Vassileva, "An overview of the composition and application of biomass ash. part 1. phase–mineral and chemical composition and classification," Fuel **105**, 40–76 (2013).

[25] M. Zevenhoven, P. Yrjas, B.-J. Skrifvars, and M. Hupa, "Characterization of ash-forming matter in various solid fuels by selective leaching and its implications for fluidized-bed combustion," Energy & Fuels **26**, 6366–6386 (2012).

[26] P. Sannigrahi, A. J. Ragauskas, and G. A. Tuskan, "Poplar as a feedstock for biofuels: a review of compositional characteristics," Biofuels, Bioproducts and Biorefining **4**, 209–226 (2010).

[27] T. Nussbaumer, "Combustion and co-combustion of biomass: fundamentals, technologies, and primary measures for emission reduction," Energy & fuels **17**, 1510–1521 (2003).

[28] S. Jiménez and J. Ballester, "Particulate matter formation and emission in the combustion of different pulverized biomass fuels," Combustion science and technology **178**, 655–683 (2006).

[29] P. Basu, J. Butler, and M. A. Leon, "Biomass co-firing options on the emission reduction and electricity generation costs in coal-fired power plants," Renewable energy **36**, 282–288 (2011).

[30] A. Ergudenler and A. Ghaly, "Agglomeration of silica sand in a fluidized bed gasifier operating on wheat straw," Biomass and bioenergy **4**, 135–147 (1993).

[31] P. Piotrowska, A. Grimm, N. Skoglund, C. Boman, M. Öhman, M. Zevenhoven, D. Boström, and M. Hupa, "Fluidized-bed combustion of mixtures of rapeseed cake and bark: The resulting bed agglomeration characteristics," Energy & Fuels **26**, 2028–2037 (2012).

[32] L. Wang, G. Skjevrak, J. E. Hustad, and Ø. Skreiberg, "Investigation of biomass ash sintering characteristics and the effect of additives," Energy & Fuels **28**, 208–218 (2013).

[33] Y. Alipour, P. Viklund, and P. Henderson, "The analysis of furnace wall deposits in a low-NOx waste wood-fired bubbling fluidised bed boiler," VGB PowerTech Journal **92**, 96–100 (2012).

[34] J.-M. Brossard, F. Lebel, C. Rapin, J.-F. Marêché, X. Chaucherie, F. Nicol, and M. Vilasi, "Lab-scale study on fireside superheaters corrosion in MSWI plants," in "17th Annual North American Waste-to-Energy Conference," (American Society of Mechanical Engineers, 2009), pp. 63–69.

[35] S. Enestam, D. Bankiewicz, J. Tuiremo, K. Mäkelä, and M. Hupa, "Are NaCl and KCl equally corrosive on superheater materials of steam boilers?" Fuel **104**, 294–306 (2013).

[36] M. Mobin, A. Malik, and M. Al-Hajri, "Investigations on the failure of economizer tubes in a high-pressure boiler," Journal of Failure Analysis and Prevention **8**, 69–74 (2008).

[37] E. Vainio, "Fate of fuel-bound nitrogen and sulfur in biomass-fired industrial boilers," (2014).

[38] A. F. Stam, K. Haasnoot, and G. Brem, "Superheater fouling in a BFB boiler firing wood-based fuel blends," Fuel **135**, 322–331 (2014).

[39] M. Theis, B.-J. Skrifvars, M. Hupa, and H. Tran, "Fouling tendency of ash resulting from burning mixtures of biofuels. part 1: Deposition rates," Fuel **85**, 1125–1130 (2006).

[40] T. Valmari, T. Lind, E. Kauppinen, G. Sfiris, K. Nilsson, and W. Maenhaut, "Field study on ash behavior during circulating fluidized-bed combustion of biomass. 2. ash deposition and alkali vapor condensation," Energy & Fuels **13**, 390–395 (1999).

[41] M. Aho, P. Yrjas, R. Taipale, M. Hupa, and J. Silvennoinen, "Reduction of superheater corrosion by co-firing risky biomass with sewage sludge," Fuel **89**, 2376–2386 (2010).

[42] B. A. Williams and J. W. Fleming, "Suppression mechanisms of alkali metal compounds," in "Proceedings," (1999), pp. 157–169.

[43] J. Birchall, "On the mechanism of flame inhibition by alkali metal salts," Combustion and Flame **14**, 85–95 (1970).

[44] L. Baxter, "Biomass-coal co-combustion: opportunity for affordable renewable energy," Fuel **84**, 1295–1302 (2005).

[45] V. Lissianski, V. Zamansky, and G. Rizeq, "Integration of direct combustion with gasification for reduction of NOx emissions," Proceedings of the Combustion Institute **29**, 2251–2258 (2002).

[46] H. Nielsen, F. Frandsen, K. Dam-Johansen, and L. Baxter, "The implications of chlorine-associated corrosion on the operation of biomass-fired boilers," Progress in energy and combustion science **26**, 283–298 (2000).

[47] J. M. Johansen, J. G. Jakobsen, F. J. Frandsen, and P. Glarborg, "Release of K, Cl, and S during pyrolysis and combustion of high-chlorine biomass," Energy & Fuels **25**, 4961–4971 (2011).

[48] H. Fatehi, Y. He, Z. Wang, Z. Li, X.-S. Bai, M. Aldén, and K. Cen, "LIBS measurements and numerical studies of potassium release during biomass gasification," Proceedings of the Combustion Institute **35**, 2389–2396 (2015).

[49] S. C. Van Lith, P. A. Jensen, F. J. Frandsen, and P. Glarborg, "Release to the gas phase of inorganic elements during wood combustion. part 2: influence of fuel composition," Energy & Fuels **22**, 1598–1609 (2008).

[50] J. N. Knudsen, "Volatilization of inorganic matter during combustion of annual biomass," Ph.D. thesis (2004).

[51] A. Novakovic, S. C. van Lith, F. J. Frandsen, P. A. Jensen, and L. B. Holgersen, "Release of potassium from the systems K- Ca- Si and K- Ca- P," Energy & Fuels **23**, 3423–3428 (2009).

[52] J. N. Knudsen, P. A. Jensen, and K. Dam-Johansen, "Transformation and release to the gas phase of Cl, K, and S during combustion of annual biomass," Energy & Fuels **18**, 1385–1399 (2004).

[53] K. Davidsson, J. Korsgren, J. Pettersson, and U. Jäglid, "The effects of fuel washing techniques on alkali release from biomass," Fuel **81**, 137–142 (2002).

[54] T. Ekvall, F. Normann, K. Andersson, and F. Johnsson, "Modeling the alkali sulfation chemistry of biomass and coal co-firing in oxy-fuel atmospheres," Energy & Fuels **28**, 3486–3494 (2014).

[55] K. A. Christensen and H. Livbjerg, "A field study of submicron particles from the combustion of straw," Aerosol science and technology **25**, 185–199 (1996).

[56] K. A. Christensen, M. Stenholm, and H. Livbjerg, "The formation of submicron aerosol particles, HCl and SO2 in straw-fired boilers," Journal of Aerosol Science **29**, 421–444 (1998).

[57] M. Broström, H. Kassman, A. Helgesson, M. Berg, C. Andersson, R. Backman, and A. Nordin, "Sulfation of corrosive alkali chlorides by ammonium sulfate in a biomass fired CFB boiler," Fuel Processing Technology **88**, 1171–1177 (2007).

[58] M. Aho, P. Vainikka, R. Taipale, and P. Yrjas, "Effective new chemicals to prevent corrosion due to chlorine in power plant superheaters," Fuel **87**, 647–654 (2008).

[59] P. Glarborg and P. Marshall, "Mechanism and modeling of the formation of gaseous alkali sulfates," Combustion and Flame **141**, 22–39 (2005).

[60] K. Schofield and M. Steinberg, "Sodium/sulfur chemical behavior in fuel-rich and-lean flames," The Journal of Physical Chemistry **96**, 715–726 (1992).

[61] M. Steinberg and K. Schofield, "The controlling chemistry of surface deposition from sodium and potassium seeded flames free of sulfur or chlorine impurities," Combustion and flame **129**, 453–470 (2002).

[62] K. Iisa, Y. Lu, and K. Salmenoja, "Sulfation of potassium chloride at combustion conditions," Energy & Fuels **13**, 1184–1190 (1999).

[63] L. Wang, J. E. Hustad, Ø. Skreiberg, G. Skjevrak, and M. Grønli, "A critical review on additives to reduce ash related operation problems in biomass combustion applications," Energy Procedia **20**, 20–29 (2012).

[64] M. Aho and E. Ferrer, "Importance of coal ash composition in protecting the boiler against chlorine deposition during combustion of chlorine-rich biomass," Fuel **84**, 201–212 (2005).

[65] T. Yang, X. Kai, Y. Sun, Y. He, and R. Li, "The effect of coal sulfur on the behavior of alkali metals during co-firing biomass and coal," Fuel **90**, 2454–2460 (2011).

[66] H. Grabke, E. Reese, and M. Spiegel, "The effects of chlorides, hydrogen chloride, and sulfur dioxide in the oxidation of steels below deposits," Corrosion science **37**, 1023–1043 (1995).

[67] B.-J. Skrifvars, R. Backman, M. Hupa, K. Salmenoja, and E. Vakkilainen, "Corrosion of superheater steel materials under alkali salt deposits part 1: The effect of salt deposit composition and temperature," Corrosion Science **50**, 1274–1282 (2008).

[68] J. Pettersson, H. Asteman, J.-E. Svensson, and L.-G. Johansson, "KCl induced corrosion of a 304-type austenitic stainless steel at 600 C; the role of potassium," Oxidation of Metals **64**, 23–41 (2005).

[69] J. Lehmusto, B.-J. Skrifvars, P. Yrjas, and M. Hupa, "Comparison of potassium chloride and potassium carbonate with respect to their tendency to cause high temperature corrosion of stainless 304L steel," Fuel processing technology **105**, 98–105 (2013).

[70] C. S. Goldenstein, R. M. Spearrin, J. B. Jeffries, and R. K. Hanson, "Infrared laser-absorption sensing for combustion gases," Progress in Energy and Combustion Science **60**, 132–176 (2017).

[71] J. M. Hollas, Modern spectroscopy (John Wiley & Sons, 2004).

[72] A. Farooq, J. B. Jeffries, and R. K. Hanson, "In situ combustion measurements of H_2O and temperature near 2.5 μm using tunable diode laser absorption," Measurement Science and Technology **19**, 075604 (2008).

[73] W. Ren, J. B. Jeffries, and R. K. Hanson, "Temperature sensing in shock-heated evaporating aerosol using wavelength-modulation absorption spectroscopy of CO_2 near 2.7 μm," Measurement Science and Technology **21**, 105603 (2010).

[74] W. Ren, A. Farooq, D. F. Davidson, and R. K. Hanson, "CO concentration and temperature sensor for combustion gases using quantum-cascade laser absorption near 4.7 μm," Applied Physics B **107**, 849–860 (2012).

[75] S. Li, A. Farooq, and R. K. Hanson, "H_2O temperature sensor for low-pressure flames using tunable diode laser absorption near 2.9 μm," Measurement Science and Technology **22**, 125301 (2011).

[76] S. Wagner, B. T. Fisher, J. W. Fleming, and V. Ebert, "TDLAS-based in situ measurement of absolute acetylene concentrations in laminar 2D diffusion flames," Proceedings of the Combustion Institute **32**, 839–846 (2009).

[77] P. Nau, J. Koppmann, A. Lackner, K. Kohse-Höinghaus, and A. Brockhinke, "Quantum cascade laser-based mir spectrometer for the determination of CO and CO_2 concentrations and temperature in flames," Applied Physics B **118**, 361–368 (2015).

[78] H. Fatehi, F. M. Schmidt, and X.-S. Bai, "Gas phase combustion in the vicinity of a biomass particle during devolatilization-model development and experimental verification," Combustion and Flame **196**, 351–363 (2018).

[79] Z. Qu, P. Holmgren, N. Skoglund, D. R. Wagner, M. Broström, and F. M. Schmidt, "Distribution of temperature, H_2O and atomic potassium during entrained flow biomass combustion–coupling in situ tdlas with modeling approaches and ash chemistry," Combustion and Flame **188**, 488–497 (2018).

[80] Z. Qu, E. Steinvall, R. Ghorbani, and F. M. Schmidt, "Tunable diode laser atomic absorption spectroscopy for detection of potassium under optically thick conditions," Analytical chemistry **88**, 3754–3760 (2016).

[81] W. Weng, Q. Gao, Z. Wang, R. Whiddon, Y. He, Z. Li, M. Aldén, and K. Cen, "Quantitative measurement of atomic potassium in plumes over burning solid fuels using infrared-diode laser spectroscopy," Energy & Fuels **31**, 2831–2837 (2017).

[82] Z. Qu, J. Fagerström, E. Steinvall, M. Broström, C. Boman, and F. Schmidt, "Real-time in-situ detection of potassium release during combustion of pelletized biomass using tunable diode laser absorption spectroscopy," Proceedings: Impacts of Fuel Quality on Power Production and Environment pp. 26–31 (2014).

[83] V. Ebert, J. Fitzer, I. Gerstenberg, K.-U. Pleban, H. Pitz, J. Wolfrum, M. Jochem, and J. Martin, "Simultaneous laser-based in situ detection of oxygen and water in a waste incinerator for active combustion control purposes," in "Symposium (International) on Combustion," (Elsevier, 1998), 1, pp. 1301–1308.

[84] V. Ebert, T. Fernholz, C. Giesemann, H. Pitz, H. Teichert, J. Wolfrum, and H. Jaritz, "Simultaneous diode-laser-based in situ detection of multiple species and temperature in a gas-fired power plant," Proceedings of the Combustion Institute **28**, 423–430 (2000).

[85] V. Ebert, H. Teichert, P. Strauch, T. Kolb, H. Seifert, and J. Wolfrum, "Sensitive in situ detection of CO and O_2 in a rotary kiln-based hazardous waste incinerator using 760 nm and new 2.3 μm diode lasers," Proceedings of the Combustion Institute **30**, 1611–1618 (2005).

[86] A. D. Sappey, P. Masterson, E. Huelson, J. Howell, M. Estes, H. Hofvander, and A. Jobson, "Results of closed-loop coal-fired boiler operation using a TDLAS sensor and smart process control software," Combustion Science and Technology **183**, 1282–1295 (2011).

[87] P. Ortwein, W. Woiwode, S. Fleck, M. Eberhard, T. Kolb, S. Wagner, M. Gisi, and V. Ebert, "Absolute diode laser-based in situ detection of HCl in gasification processes," Experiments in fluids **49**, 961–968 (2010).

[88] X. Chao, J. B. Jeffries, and R. K. Hanson, "In situ absorption sensor for NO in combustion gases with a 5.2 μm quantum-cascade laser," Proceedings of the Combustion Institute **33**, 725–733 (2011).

[89] E. Schlosser, T. Fernholz, H. Teichert, and V. Ebert, "In situ detection of potassium atoms in high-temperature coal-combustion systems using near-infrared-diode lasers," Spectrochimica Acta Part A: Molecular and Biomolecular Spectroscopy **58**, 2347–2359 (2002).

[90] E. Schlosser, J. Wolfrum, L. Hildebrandt, H. Seifert, B. Oser, and V. Ebert, "Diode laser based in situ detection of alkali atoms: development of a new method for determination of residence-time distribution in combustion plants," Applied Physics B **75**, 237–247 (2002).

[91] Q. Gao, W.-B. Weng, B. Li, and Z.-S. Li, "Quantitative and spatially resolved measurement of atomic potassium in combustion using diode laser," Chinese Physics Letters **35**, 024202 (2018).

[92] J. Mellqvist and A. Rosen, "DOAS for flue gas monitoring - I. temperature effects in the UV/visible absorption spectra of NO, NO_2, SO_2 and NH_3," Journal of Quantitative Spectroscopy and Radiative Transfer **56**, 187–208 (1996).

[93] T. Leffler, C. Brackmann, M. Berg, M. Aldén, and Z. Li, "Online alkali measurement during oxy-fuel combustion," Energy Procedia **120**, 365–372 (2017).

[94] T. Leffler, C. Brackmann, M. Berg, M. Aldén, and Z. Li, "Development of an alkali chloride vapour-generating apparatus for calibration of ultraviolet absorption measurements," Review of Scientific Instruments **88**, 023112 (2017).

[95] W. Weng, T. Leffler, C. Brackmann, M. Aldén, and Z. Li, "Spectrally resolved UV absorption cross-sections of alkali hydroxides and chlorides measured in hot flue gases," Applied spectroscopy pp. 1388–1395 (2018).

[96] C. Forsberg, M. Broström, R. Backman, E. Edvardsson, S. Badiei, M. Berg, and H. Kassman, "Principle, calibration, and application of the in situ alkali chloride monitor," Review of Scientific Instruments **80**, 023104 (2009).

[97] T. Ekvall, K. Andersson, T. Leffler, and M. Berg, "K-Cl-S chemistry in air and oxy-combustion atmospheres," Proceedings of the Combustion Institute **36**, 4011–4018 (2017).

[98] T. Leffler, C. Brackmann, A. Ehn, B. Kaldvee, M. Aldén, M. Berg, and J. Bood, "Range-resolved detection of potassium chloride using picosecond differential absorption light detection and ranging," Applied optics **54**, 1058–1064 (2015).

[99] B. Kaldvee, C. Brackmann, M. Aldén, and J. Bood, "Highly range-resolved ammonia detection using near-field picosecond differential absorption lidar," Optics express **20**, 20688–20697 (2012).

[100] E. Malmqvist, M. Brydegaard, M. Aldén, and J. Bood, "Scheimpflug Lidar for combustion diagnostics," Optics Express **26**, 14842–14858 (2018).

[101] P. Zalicki and R. N. Zare, "Cavity ring-down spectroscopy for quantitative absorption measurements," The Journal of chemical physics **102**, 2708–2717 (1995).

[102] M. D. Wheeler, S. M. Newman, A. J. Orr-Ewing, and M. N. Ashfold, "Cavity ring-down spectroscopy," Journal of the Chemical Society, Faraday Transactions **94**, 337–351 (1998).

[103] A. Schocker, K. Kohse-Höinghaus, and A. Brockhinke, "Quantitative determination of combustion intermediates with cavity ring-down spectroscopy: systematic study in propene flames near the soot-formation limit," Applied optics **44**, 6660–6672 (2005).

[104] C. Moreau, E. Therssen, P. Desgroux, J. Pauwels, A. Chapput, and M. Barj, "Quantitative measurements of the CH radical in sooting diffusion flames at atmospheric pressure," Applied Physics B **76**, 597–602 (2003).

[105] K. Kohse-Höinghaus, A. Schocker, T. Kasper, M. Kamphus, and A. Brockhinke, "Combination of laser-and mass-spectroscopic techniques for the investigation of fuel-rich flames," Zeitschrift für Physikalische Chemie **219**, 583–599 (2005).

[106] C. C. Carter, "A cavity ring-down spectroscopy mercury continuous emission monitor," Tech. rep., Sensor Research and Development Corporation (2004).

[107] R. K. Hanson, J. M. Seitzman, and P. H. Paul, "Planar laser-fluorescence imaging of combustion gases," Applied Physics B **50**, 441–454 (1990).

[108] L. Ma, Q. Lei, T. Capil, S. D. Hammack, and C. D. Carter, "Direct comparison of two-dimensional and three-dimensional laser-induced fluorescence measurements on highly turbulent flames," Optics letters **42**, 267–270 (2017).

[109] I. Van Cruyningen, A. Lozano, and R. Hanson, "Quantitative imaging of concentration by planar laser-induced fluorescence," Experiments in Fluids **10**, 41–49 (1990).

[110] Z. Li, J. Kiefer, J. Zetterberg, M. Linvin, A. Leipertz, X.-S. Bai, and M. Aldén, "Development of improved PLIF CH detection using an alexandrite laser for single-shot investigation of turbulent and lean flames," Proceedings of the Combustion Institute **31**, 727–735 (2007).

[111] J. M. Donbar, J. F. Driscoll, and C. D. Carter, "Reaction zone structure in turbulent nonpremixed jet flames from CH-OH PLIF images," Combustion and Flame **122**, 1–19 (2000).

[112] C. Kaminski, J. Hult, and M. Aldén, "High repetition rate planar laser induced fluorescence of OH in a turbulent non-premixed flame," Applied Physics B: Lasers and Optics **68**, 757–760 (1999).

[113] Z. Li, B. Li, Z. Sun, X.-S. Bai, and M. Aldén, "Turbulence and combustion interaction: High resolution local flame front structure visualization using simultaneous single-shot PLIF imaging of CH, OH, and CH_2O in a piloted premixed jet flame," Combustion and Flame **157**, 1087–1096 (2010).

[114] N. P. Tait and D. A. Greenhalgh, "PLIF imaging of fuel fraction in practical devices and LII imaging of soot," Berichte der Bunsengesellschaft fuer Physikalische Chemie **97**, 1619–1624 (1993).

[115] S.-Y. Lee, S. Seo, J. Broda, S. Pal, and R. Santoro, "An experimental estimation of mean reaction rate and flame structure during combustion instability in a lean premixed gas turbine combustor," Proceedings of the Combustion Institute **28**, 775–782 (2000).

[116] J. Köser, L. G. Becker, A.-K. Goßmann, B. Böhm, and A. Dreizler, "Investigation of ignition and volatile combustion of single coal particles within

oxygen-enriched atmospheres using high-speed OH-PLIF," Proceedings of the Combustion Institute **36**, 2103–2111 (2017).

[117] J. R. Osborne, S. A. Ramji, C. D. Carter, and A. M. Steinberg, "Relationship between local reaction rate and flame structure in turbulent premixed flames from simultaneous 10 kHz TPIV, OH PLIF, and CH_2O PLIF," Proceedings of the Combustion Institute **36**, 1835–1841 (2017).

[118] P. Monkhouse, "On-line spectroscopic and spectrometric methods for the determination of metal species in industrial processes," Progress in Energy and Combustion Science **37**, 125–171 (2011).

[119] B. Li, D. Zhang, M. Yao, and Z. Li, "Strategy for single-shot CH_3 imaging in premixed methane/air flames using photofragmentation laser-induced fluorescence," Proceedings of the Combustion Institute **36**, 4487–4495 (2017).

[120] T. Leffler, C. Brackmann, M. Aldén, and Z. Li, "Laser-induced photofragmentation fluorescence imaging of alkali compounds in flames," Applied spectroscopy **71**, 1289–1299 (2017).

[121] K. Larsson, D. Hot, A. Ehn, A. Lantz, W. Weng, M. Aldén, and J. Bood, "Quantitative imaging of ozone vapor using photofragmentation laser-induced fluorescence (LIF)," Applied spectroscopy **71**, 1578–1585 (2017).

[122] F. Greger, K. Hartinger, P. Monkhouse, J. Wolfrum, H. Baumann, and B. Bonn, "In situ alkali concentration measurements in a pressuried, fluidized-bed coal combustor by excimer laser induced fragmentation fluorescence," in "Symposium (International) on Combustion," (Elsevier, 1996), 2, pp. 3301–3307.

[123] M. P. Glazer, N. A. Khan, W. de Jong, H. Spliethoff, H. Schürmann, and P. Monkhouse, "Alkali metals in circulating fluidized bed combustion of biomass and coal: measurements and chemical equilibrium analysis," Energy & fuels **19**, 1889–1897 (2005).

[124] K. Nyholm, R. Fritzon, and M. Aldén, "Two-dimensional imaging of oh in flames by use of polarization spectroscopy," Optics letters **18**, 1672–1674 (1993).

[125] M. Aldén, J. Bood, Z. Li, and M. Richter, "Visualization and understanding of combustion processes using spatially and temporally resolved laser diagnostic techniques," Proceedings of the Combustion Institute **33**, 69–97 (2011).

[126] K. Nyholm, R. Maier, C. Aminoff, and M. Kaivola, "Detection of OH in flames by using polarization spectroscopy," Applied optics **32**, 919–924 (1993).

[127] Z. Li, Z. Sun, B. Li, M. Aldén, and M. Försth, "Spatially resolved trace detection of HCl in flames with mid-infrared polarization spectroscopy," Optics letters **33**, 1836–1838 (2008).

[128] B. Li, Z. Sun, Z. Li, M. Aldén, J. G. Jakobsen, S. Hansen, and P. Glarborg, "Post-flame gas-phase sulfation of potassium chloride," Combustion and flame **160**, 959–969 (2013).

[129] J. Pender and L. Hesselink, "Phase conjugation in a flame," Optics letters **10**, 264–266 (1985).

[130] K. Nyholm, R. Fritzon, and M. Aldén, "Single-pulse two-dimensional temperature imaging in flames by degenerate four-wave mixing and polarization spectroscopy," Applied Physics B **59**, 37–43 (1994).

[131] P. Ewart and S. O'Leary, "Detection of OH in a flame by degenerate four-wave mixing," Optics letters **11**, 279–281 (1986).

[132] A. Grant, P. Ewart, and C. Stone, "Detection of NO in a spark-ignition research engine using degenerate four-wave mixing," Applied Physics B **74**, 105–110 (2002).

[133] C. De-Ying, F. Rong-Wei, Y. Xin-Ju, Z. Qi-Ke, and Q. Qi-Zong, "Degenerate four-wave mixing in SO_2 in free jets," Chinese Physics Letters **21**, 295 (2004).

[134] Z. Sun, Z. Li, B. Li, M. Aldén, and P. Ewart, "Detection of C_2H_2 and HCl using mid-infrared degenerate four-wave mixing with stable beam alignment: towards practical in situ sensing of trace molecular species," Applied Physics B **98**, 593–600 (2010).

[135] D. Hot, R. L. Pedersen, W. Weng, Y. Zhang, M. Aldén, and Z. Li, "Spatially and temporally resolved ir-dfwm measurement of HCN released from gasification of biomass pellets," Proceedings of the Combustion Institute (2018).

[136] Y. Chen, C. Zou, M. Mastalerz, S. Hu, C. Gasaway, and X. Tao, "Applications of micro-fourier transform infrared spectroscopy (FTIR) in the geological sciences - a review," International journal of molecular sciences **16**, 30223–30250 (2015).

[137] A. Bouyanfif, S. Liyanage, E. Hequet, N. Moustaid-Moussa, and N. Abidi, "Review of FTIR microspectroscopy applications to investigate biochemical changes in C. elegans," Vibrational Spectroscopy (2018).

[138] R. Mukhopadhyay, "Product review: portable FTIR spectrometers get moving," (2004).

[139] P. R. Griffiths and J. A. De Haseth, Fourier transform infrared spectrometry, vol. 171 (John Wiley & Sons, 2007).

[140] R. Bassilakis, R. Carangelo, and M. Wojtowicz, "TG-FTIR analysis of biomass pyrolysis," Fuel **80**, 1765–1786 (2001).

[141] M. Fang, D. Shen, Y. Li, C. Yu, Z. Luo, and K. Cen, "Kinetic study on pyrolysis and combustion of wood under different oxygen concentrations by using TG-FTIR analysis," Journal of analytical and applied pyrolysis **77**, 22–27 (2006).

[142] E. Biagini, F. Barontini, and L. Tognotti, "Devolatilization of biomass fuels and biomass components studied by TG/FTIR technique," Industrial & Engineering Chemistry Research **45**, 4486–4493 (2006).

[143] Q. Liu, Z. Zhong, S. Wang, and Z. Luo, "Interactions of biomass components during pyrolysis: A TG-FTIR study," Journal of Analytical and Applied Pyrolysis **90**, 213–218 (2011).

[144] W. De Jong, G. Di Nola, B. Venneker, H. Spliethoff, and M. Wójtowicz, "TG-FTIR pyrolysis of coal and secondary biomass fuels: Determination of pyrolysis kinetic parameters for main species and NOx precursors," Fuel **86**, 2367–2376 (2007).

[145] E. Vainio, A. Brink, M. Hupa, H. Vesala, and T. Kajolinna, "Fate of fuel nitrogen in the furnace of an industrial bubbling fluidized bed boiler during combustion of biomass fuel mixtures," Energy & Fuels **26**, 94–101 (2011).

[146] D. W. Griffith, W. G. Mankin, M. T. Coffey, D. E. Ward, and A. Riebau, "FTIR remote sensing of biomass burning emissions of CO_2, CO, CH_4, CH_2O, NO, NO_2, NH_3, and N_2O," in "Global Biomass Burning - Atmospheric, Climatic, and Biospheric Implications," (1991).

[147] C. Stockwell, R. Yokelson, S. Kreidenweis, A. Robinson, P. DeMott, R. Sullivan, J. Reardon, K. Ryan, D. W. Griffith, and L. Stevens, "Trace gas emissions from combustion of peat, crop residue, domestic biofuels, grasses, and other fuels: configuration and fourier transform infrared (FTIR) component of the fourth Fire Lab at Missoula Experiment (FLAME-4)," (2014).

[148] J. Feist, A. Heyes, K. Choy, and B. Su, "Phosphor thermometry for high temperature gas turbine applications," in "Instrumentation in Aerospace Simulation Facilities, 1999. ICIASF 99. 18th International Congress on," (IEEE, 1999), pp. 6–1.

[149] S. Alaruri, T. Bonsett, A. Brewington, E. McPheeters, and M. Wilson, "Mapping the surface temperature of ceramic and superalloy turbine engine components using laser-induced fluorescence of thermographic phosphor," Optics and lasers in engineering **31**, 345–351 (1999).

[150] A. C. Edge, G. Laufer, and R. H. Krauss, "Surface temperature-field imaging with laser-induced thermographic phosphorescence," Applied optics **39**, 546–553 (2000).

[151] G. Särner, M. Richter, and M. Aldén, "Two-dimensional thermometry using temperature-induced line shifts of ZnO: Zn and ZnO: Ga fluorescence," Optics letters **33**, 1327–1329 (2008).

[152] R. Dibble and R. Hollenbach, "Laser Rayleigh thermometry in turbulent flames," NASA STI/Recon Technical Report N **81** (1981).

[153] D. Hoffman, K.-U. Münch, and A. Leipertz, "Two-dimensional temperature determination in sooting flames by filtered Rayleigh scattering," Optics letters **21**, 525–527 (1996).

[154] G. S. Elliott, N. Glumac, and C. D. Carter, "Molecular filtered Rayleigh scattering applied to combustion," Measurement Science and Technology **12**, 452 (2001).

[155] J. Fielding, J. H. Frank, S. A. Kaiser, M. D. Smooke, and M. B. Long, "Polarized/depolarized Rayleigh scattering for determining fuel concentrations in flames," Proceedings of the Combustion Institute **29**, 2703–2709 (2002).

[156] C. A. Idicheria and L. M. Pickett, "Quantitative mixing measurements in a vaporizing diesel spray by Rayleigh imaging," Tech. rep., SAE Technical Paper (2007).

[157] M. J. Papageorge, T. A. McManus, F. Fuest, and J. A. Sutton, "Recent advances in high-speed planar Rayleigh scattering in turbulent jets and flames: increased record lengths, acquisition rates, and image quality," Applied Physics B **115**, 197–213 (2014).

[158] O. Degardin, B. Renou, and A. Boukhalfa, "Simultaneous measurement of temperature and fuel mole fraction using acetone planar induced fluorescence and Rayleigh scattering in stratified flames," Experiments in Fluids **40**, 452–463 (2006).

[159] J. A. Sutton and J. F. Driscoll, "Scalar dissipation rate measurements in flames: a method to improve spatial resolution by using nitric oxide PLIF," Proceedings of the combustion institute **29**, 2727–2734 (2002).

[160] B. Zhou, C. Brackmann, Z. Li, M. Aldén, and X.-S. Bai, "Simultaneous multi-species and temperature visualization of premixed flames in the distributed reaction zone regime," Proceedings of the Combustion Institute **35**, 1409–1416 (2015).

[161] L. K. Su, D. Han, and M. Mungal, "Measurements of velocity and fuel concentration in the stabilization region of lifted jet diffusion flames," Proceedings of the Combustion Institute **28**, 327–334 (2000).

[162] S. m. Hwang, R. Kurose, F. Akamatsu, H. Tsuji, H. Makino, and M. Katsuki, "Application of optical diagnostics techniques to a laboratory-scale turbulent pulverized coal flame," Energy & Fuels **19**, 382–392 (2005).

[163] J. Hayashi, N. Hashimoto, N. Nakatsuka, K. Tainaka, H. Tsuji, K. Tanno, H. Watanabe, H. Makino, and F. Akamatsu, "Simultaneous imaging of mie scattering, pahs laser induced fluorescence and soot laser induced incandescence to a lab-scale turbulent jet pulverized coal flame," Proceedings of the Combustion Institute **37**, 3045–3052 (2019).

[164] A. C. Eckbreth and T. J. Anderson, "Dual broadband CARS for simultaneous, multiple species measurements," Applied optics **24**, 2731–2736 (1985).

[165] A. Bohlin, M. Mann, B. D. Patterson, A. Dreizler, and C. J. Kliewer, "Development of two-beam femtosecond/picosecond one-dimensional rotational coherent anti-Stokes Raman spectroscopy: time-resolved probing of flame wall interactions," Proceedings of the Combustion Institute **35**, 3723–3730 (2015).

[166] S. Roy, J. R. Gord, and A. K. Patnaik, "Recent advances in coherent anti-Stokes Raman scattering spectroscopy: Fundamental developments and applications in reacting flows," Progress in Energy and Combustion Science **36**, 280–306 (2010).

[167] A. Bohlin, B. D. Patterson, and C. J. Kliewer, "Communication: Simplified two-beam rotational CARS signal generation demonstrated in 1D," The Journal of Chemical Physics **138** (2013).

[168] F. Fuest, R. S. Barlow, G. Magnotti, A. Dreizler, I. W. Ekoto, and J. A. Sutton, "Quantitative acetylene measurements in laminar and turbulent flames using 1D Raman/Rayleigh scattering," Combustion and Flame **162**, 2248–2255 (2015).

[169] Y. Kobayashi, S. Tanaka, and M. Arai, "PAHs behavior and graphitization degree of soot in a hexane diffusion flame," J Nanosci Nanotechnol **2**, 1–12 (2018).

[170] C. Haisch, "Photoacoustic spectroscopy for analytical measurements," Measurement Science and Technology **23**, 012001 (2011).

[171] H. Jalink and D. Bicanic, "Concept, design, and use of the photoacoustic heat pipe cell," Applied physics letters **55**, 1507–1509 (1989).

[172] J. Stenberg, R. Hernberg, and J. Vattulainen, "Analysis of pollutant chemistry in combustion by in situ pulsed photoacoustic laser diagnostics," Applied optics **34**, 8400–8408 (1995).

[173] J. Stenberg, L.-E. Åmand, R. Hernberg, and B. Leckner, "Measurements of gas concentrations in a fluidized bed combustor using laser-induced photoacoustic spectroscopy and zirconia cell probes," Combustion and flame **113**, 477–486 (1998).

[174] T. Sorvajärvi, A. Manninen, J. Toivonen, J. Saarela, and R. Hernberg, "Resonant photoacoustic cell for pulsed laser analysis of gases at high temperature," Review of Scientific Instruments **80**, 123103 (2009).

[175] D. Bradley and K. Matthews, "Measurement of high gas temperatures with fine wire thermocouples," Journal of Mechanical Engineering Science **10**, 299–305 (1968).

[176] V. Hindasageri, R. Vedula, and S. Prabhu, "Thermocouple error correction for measuring the flame temperature with determination of emissivity and heat transfer coefficient," Review of Scientific Instruments **84**, 024902 (2013).

[177] M. Tagawa and Y. Ohta, "Two-thermocouple probe for fluctuating temperature measurement in combustion - rational estimation of mean and fluctuating time constants," Combustion and flame **109**, 549–560 (1997).

[178] M. Gil, J. Riaza, L. Álvarez, C. Pevida, J. Pis, and F. Rubiera, "Oxy-fuel combustion kinetics and morphology of coal chars obtained in N_2 and CO_2 atmospheres in an entrained flow reactor," Applied Energy **91**, 67–74 (2012).

[179] Z. Chen, M. Hu, X. Zhu, D. Guo, S. Liu, Z. Hu, B. Xiao, J. Wang, and M. Laghari, "Characteristics and kinetic study on pyrolysis of five lignocellulosic biomass via thermogravimetric analysis," Bioresource technology **192**, 441–450 (2015).

[180] J. F. Saldarriaga, R. Aguado, A. Pablos, M. Amutio, M. Olazar, and J. Bilbao, "Fast characterization of biomass fuels by thermogravimetric analysis (TGA)," Fuel **140**, 744–751 (2015).

[181] P. Monkhouse, "On-line diagnostic methods for metal species in industrial process gas," Progress in energy and combustion science **28**, 331–381 (2002).

[182] J. G. Olsson, U. Jäglid, J. B. Pettersson, and P. Hald, "Alkali metal emission during pyrolysis of biomass," Energy & Fuels **11**, 779–784 (1997).

[183] K. Davidsson, B. Stojkova, and J. Pettersson, "Alkali emission from birchwood particles during rapid pyrolysis," Energy & Fuels **16**, 1033–1039 (2002).

[184] M. Wellinger, S. Biollaz, J. Wochele, and C. Ludwig, "Sampling and online analysis of alkalis in thermal process gases with a novel surface ionization detector," Energy & Fuels **25**, 4163–4171 (2011).

[185] K. O. Davidsson, K. Engvall, M. Hagström, J. G. Korsgren, B. Lönn, and J. B. Pettersson, "A surface ionization instrument for on-line measurements of alkali metal components in combustion: Instrument description and applications," Energy & fuels **16**, 1369–1377 (2002).

[186] V. Häyrinen, R. Hernberg, R. Oikari, U. Gottwald, P. Monkhouse, K. Davidsson, B. Lönn, K. Engvall, J. Pettersson, P. Lehtonen, and R. Kuivalainen, "On-line determination of alkali concentrations in pressurized fluidised-bed coal combustion by combined measurement techniques," in "6th Conference on Circulating Fluidized Bed Combustion," (1999).

[187] V. Häyrinen, R. Hernberg, and M. Aho, "Demonstration of plasma excited atomic resonance line spectroscopy for on-line measurement of alkali metals in a 20 kW bubbling fluidized bed," Fuel **83**, 791–797 (2004).

[188] R. Oikari, V. Häyrinen, T. Parviainen, and R. Hernberg, "Continuous monitoring of toxic metals in gas flows using direct-current plasma excited atomic absorption spectroscopy," Applied Spectroscopy **55**, 1469–1477 (2001).

[189] R. Oikari, M. Aho, and R. Hernberg, "Demonstration of a new on-line analyzer for the measurement of vaporized toxic metal compounds in a fluidized bed combustor," Energy & fuels **17**, 87–94 (2003).

[190] S. Abanades, G. Flamant, and D. Gauthier, "The kinetics of vaporization of a heavy metal from a fluidized waste by an inverse method," Combustion and flame **134**, 315–326 (2003).

[191] K. Nishiguchi, K. Utani, D. Gunther, and M. Ohata, "Gas to particle conversion-gas exchange technique for direct analysis of metal carbonyl gas by inductively coupled plasma mass spectrometry," Analytical chemistry **86**, 10025–10029 (2014).

[192] K. Nishiguchi, K. Utani, and E. Fujimori, "Real-time multielement monitoring of airborne particulate matter using ICP-MS instrument equipped with gas converter apparatus," Journal of Analytical Atomic Spectrometry **23**, 1125–1129 (2008).

[193] D. C. Dayton, R. J. French, and T. A. Milne, "Direct observation of alkali vapor release during biomass combustion and gasification. 1. application of molecular beam/mass spectrometry to switchgrass combustion," Energy & Fuels **9**, 855–865 (1995).

[194] D. Dayton, B. Jenkins, S. Turn, R. Bakker, R. Williams, D. Belle-Oudry, and L. Hill, "Release of inorganic constituents from leached biomass during thermal conversion," Energy & Fuels **13**, 860–870 (1999).

[195] T. Sorvajärvi, N. DeMartini, J. Rossi, and J. Toivonen, "In situ measurement technique for simultaneous detection of K, KCl, and KOH vapors released during combustion of solid biomass fuel in a single particle reactor," Applied spectroscopy **68**, 179–184 (2014).

[196] T. Sorvajärvi, "Advanced optical diagnostic techniques for detection of alkali vapors in high-temperature gases," Tampereen teknillinen yliopisto. Julkaisu-Tampere University of Technology. Publication; 1177 (2013).

[197] H. Dautriche, "The effect of alkaline salts with a fixed base on the combustion of gases and the combustible thrust," Compt. Rend **146**, 535 (1908).

[198] M. Steinberg and K. Schofield, "The chemistry of sodium with sulfur in flames," Prog. Energy Combust. Sci **16**, 311–317 (1990).

[199] K. S. Iya, S. Wollowitz, and W. E. Kaskan, "The mechanism of flame inhibition by sodium salts," in "Symposium (International) on Combustion," (Elsevier, 1975), 1, pp. 329–336.

[200] L. Hindiyarti, F. Frandsen, H. Livbjerg, and P. Glarborg, "Influence of potassium chloride on moist CO oxidation under reducing conditions: Experimental and kinetic modeling study," Fuel **85**, 978–988 (2006).

[201] R. A. Perry and J. A. Miller, "An exploratory investigation of the use of alkali metals in nitrous oxide control," International journal of chemical kinetics **28**, 217–234 (1996).

[202] V. V. Lissianski, V. M. Zamansky, and P. M. Maly, "Effect of metal-containing additives on NOx reduction in combustion and reburning," Combustion and flame **125**, 1118–1127 (2001).

[203] V. M. Zamansky, M. S. Sheldon, and P. M. Maly, "Enhanced NOx reduction by interaction of nitrogen and sodium compounds in the reburning zone," in "Symposium (International) on combustion," (Elsevier, 1998), 2, pp. 3001–3008.

[204] P. Glarborg, "Hidden interactions - trace species governing combustion and emissions," Proceedings of the combustion institute **31**, 77–98 (2007).

[205] A. Hayhurst and H. Jones, "The effect of metallic additives on ionization and soot formation in oxy acetylene flames," Combustion and flame **78**, 339–356 (1989).

[206] P. Bonczyk, "Effects of metal additives on soot precursors and particulates in a $C_2H_4/O_2/N_2$/Ar premixed flame," Fuel **70**, 1403–1411 (1991).

[207] B. Haynes, H. Jander, and H. G. Wagner, "The effect of metal additives on the formation of soot in premixed flames," in "Symposium (international) on Combustion," (Elsevier, 1979), 1, pp. 1365–1374.

[208] M. Tappe, B. Haynes, and J. Kent, "The effect of alkali metals on a laminar ethylene diffusion flame," Combustion and flame **92**, 266–273 (1993).

[209] A. Hynes, M. Steinberg, and K. Schofield, "The chemical kinetics and thermodynamics of sodium species in oxygen-rich hydrogen flames," The Journal of chemical physics **80**, 2585–2597 (1984).

[210] W. E. Kaskan, "The reaction of alkali atoms in lean flames," in "Symposium (International) on Combustion," (Elsevier, 1965), 1, pp. 41–46.

[211] L. Hindiyarti, F. Frandsen, H. Livbjerg, P. Glarborg, and P. Marshall, "An exploratory study of alkali sulfate aerosol formation during biomass combustion," Fuel **87**, 1591–1600 (2008).

[212] J. Silver, M. Zahniser, A. Stanton, and C. Kolb, "Temperature dependent termolecular reaction rate constants for potassium and sodium superoxide formation," in "Symposium (International) on Combustion," (Elsevier, 1985), 1, pp. 605–612.

[213] D. Husain and J. M. Plane, "Kinetic investigation of the third-order rate processes between $K+O_2+M$ by time-resolved atomic resonance absorption spectroscopy," Journal of the Chemical Society, Faraday Transactions 2: Molecular and Chemical Physics **78**, 1175–1194 (1982).

[214] J. M. Plane, B. Rajasekhar, and L. Bartolotti, "Kinetic study of the reaction potassium+ oxygen+ M (M= nitrogen, helium) from 250 to 1103 K," Journal of Physical Chemistry **94**, 4161–4167 (1990).

[215] R. Patrick and D. M. Golden, "Termolecular reactions of alkali metal atoms with O_2 and OH," International journal of chemical kinetics **16**, 1567–1574 (1984).

[216] M. Vasiliu, S. Li, K. A. Peterson, D. Feller, J. L. Gole, and D. A. Dixon, "Structures and heats of formation of simple alkali metal compounds: Hydrides, chlorides, fluorides, hydroxides, and oxides for Li, Na, and K," The Journal of Physical Chemistry A **114**, 4272–4281 (2010).

[217] H. Figger, W. Schrepp, and X.-h. Zhu, "Chemiluminescent reaction between alkali dimers and oxygen molecules," The Journal of chemical physics **79**, 1320–1325 (1983).

[218] T. Sorvajärvi and J. Toivonen, "Detection of $PbCl_2$ using collinear photofragmentation and atomic absorption spectroscopy," in "Lasers and Electro-Optics (CLEO), 2014 Conference on," (IEEE, 2014), pp. 1–2.

[219] A. Heays, v. Bosman, AD, and E. van Dishoeck, "Photodissociation and photoionisation of atoms and molecules of astrophysical interest," Astronomy & Astrophysics **602**, A105 (2017).

[220] J. Simeonsson and R. Sausa, "A critical review of laser photofragmentation/fragment detection techniques for gas-phase chemical analysis," Applied Spectroscopy Reviews **31**, 1–72 (1996).

[221] R. Schinke, Photodissociation dynamics: spectroscopy and fragmentation of small polyatomic molecules, 1 (Cambridge University Press, 1995).

[222] T. Sorvajärvi and J. Toivonen, "Principles and calibration of collinear photofragmentation and atomic absorption spectroscopy," Applied Physics B **115**, 533–539 (2014).

[223] P. Davidovits and D. Brodhead, "Ultraviolet absorption cross sections for the alkali halide vapors," The Journal of Chemical Physics **46**, 2968–2973 (1967).

[224] J. Kerr, "Bond dissociation energies by kinetic methods," Chemical reviews **66**, 465–500 (1966).

[225] Z. Qu, R. Ghorbani, D. Valiev, and F. M. Schmidt, "Calibration-free scanned wavelength modulation spectroscopy-application to H_2O and temperature sensing in flames," Optics Express **23**, 16492–16499 (2015).

[226] J. M. Seitzman, G. Kychakoff, and R. K. Hanson, "Instantaneous temperature field measurements using planar laser-induced fluorescence," Optics letters **10**, 439–441 (1985).

[227] A. Omrane, P. Petersson, M. Aldén, and M. Linne, "Simultaneous 2D flow velocity and gas temperature measurements using thermographic phosphors," Applied Physics B **92**, 99–102 (2008).

[228] P. Nooren, M. Versluis, T. H. van der Meer, R. Barlow, and J. Frank, "Raman-Rayleigh-LIF measurements of temperature and species concentrations in the Delft piloted turbulent jet diffusion flame," Applied Physics B **71**, 95–111 (2000).

[229] R. M. Mihalcea, D. S. Baer, and R. K. Hanson, "A diode-laser absorption sensor system for combustion emission measurements," Measurement Science and Technology **9**, 327 (1998).

[230] W. Koban, J. Schorr, and C. Schulz, "Oxygen-distribution imaging with a novel two-tracer laser-induced fluorescence technique," Applied Physics B **74**, 111–114 (2002).

[231] W. L. Saw, G. J. Nathan, P. J. Ashman, Z. T. Alwahabi, and M. Hupa, "Simultaneous measurement of the surface temperature and the release of atomic sodium from a burning black liquor droplet," Combustion and Flame **157**, 769–777 (2010).

[232] M. Cardoso, É. D. de Oliveira, and M. L. Passos, "Chemical composition and physical properties of black liquors and their effects on liquor recovery operation in Brazilian pulp mills," Fuel **88**, 756–763 (2009).

[233] A. Pettersson, M. Zevenhoven, B.-M. Steenari, and L.-E. Åmand, "Application of chemical fractionation methods for characterisation of biofuels, waste derived fuels and CFB co-combustion fly ashes," Fuel **87**, 3183–3193 (2008).

[234] Z. Yan, Z. XinLei, J. WenBao, S. Qing, L. YongSheng, H. DaQian, and C. Da, "Online X-ray fluorescence (XRF) analysis of heavy metals in pulverized coal on a conveyor belt," Applied spectroscopy **70**, 272–278 (2016).

[235] A. C. Aiken, P. F. DeCarlo, and J. L. Jimenez, "Elemental analysis of organic species with electron ionization high-resolution mass spectrometry," Analytical Chemistry **79**, 8350–8358 (2007).

[236] J. D. Fassett and P. J. Paulsen, "Isotope dilution mass spectrometry for accurate elemental analysis," Analytical chemistry **61**, 643A–649A (1989).

[237] Y. Liu, Z. Hu, S. Gao, D. Günther, J. Xu, C. Gao, and H. Chen, "In situ analysis of major and trace elements of anhydrous minerals by LA-ICP-MS without applying an internal standard," Chemical Geology **257**, 34–43 (2008).

[238] D. J. Douglas, E. S. Quan, and R. Smith, "Elemental analysis with an atmospheric pressure plasma (MIP, ICP)/quadrupole mass spectrometer system," Spectrochimica Acta Part B: Atomic Spectroscopy **38**, 39–48 (1983).

[239] J. W. Olesik, "Elemental analysis using ICP-OES and ICP/MS," Analytical Chemistry **63**, 12A–21A (1991).

[240] D. Day, B. Connors, M. Jennings, J. Egan, K. Derman, P. Soucy, S. Moller, and D. Sackett, "A full featured handheld LIBS analyzer with early results for defense and security," in "Next-Generation Spectroscopic Technologies VIII," (International Society for Optics and Photonics, 2015), p. 948206.

[241] L. St-Onge, E. Kwong, M. Sabsabi, and E. Vadas, "Quantitative analysis of pharmaceutical products by laser-induced breakdown spectroscopy," Spectrochimica Acta Part B: Atomic Spectroscopy **57**, 1131–1140 (2002).

[242] S. Rosenwasser, G. Asimellis, B. Bromley, R. Hazlett, J. Martin, T. Pearce, and A. Zigler, "Development of a method for automated quantitative analysis of ores using LIBS," Spectrochimica Acta Part B: Atomic Spectroscopy **56**, 707–714 (2001).

[243] W. Wang, S. Li, H. Qi, B. Ayhan, C. Kwan, and S. Vance, "Revisiting the preprocessing procedures for elemental concentration estimation based on CHEMCAM LIBS on MARS rover," in "Hyperspectral Image and Signal Processing: Evolution in Remote Sensing (WHISPERS), 2014 6th Workshop on," (IEEE, 2014), pp. 1–4.

[244] L. J. Radziemski and D. A. Cremers, Handbook of laser induced breakdown spectroscopy (John Wiley & Sons, 2006).

[245] M. I. Boulos, P. Fauchais, and E. Pfender, Thermal plasmas: fundamentals and applications (Springer Science & Business Media, 2013).

[246] L. Cabalin and J. Laserna, "Experimental determination of laser induced breakdown thresholds of metals under nanosecond Q-switched laser operation," Spectrochimica Acta Part B: Atomic Spectroscopy **53**, 723–730 (1998).

[247] D. Hahn and U. Panne, "LIBS for aerosol analysis," in "Laser-Induced Breakdown Spectroscopy," (Elsevier, 2007), pp. 381–417.

[248] N. Arnold, J. Gruber, and J. Heitz, "Spherical expansion of the vapor plume into ambient gas: an analytical model," Applied Physics A **69**, S87–S93 (1999).

[249] M. Corsi, G. Cristoforetti, M. Giuffrida, M. Hidalgo, S. Legnaioli, V. Palleschi, A. Salvetti, E. Tognoni, and C. Vallebona, "Three-dimensional analysis of laser induced plasmas in single and double pulse configuration," Spectrochimica Acta Part B: Atomic Spectroscopy **59**, 723–735 (2004).

[250] M. Sabsabi and P. Cielo, "Quantitative analysis of aluminum alloys by laser-induced breakdown spectroscopy and plasma characterization," Applied Spectroscopy **49**, 499–507 (1995).

[251] C. Aragon, F. Penalba, and J. Aguilera, "Spatial characterization of laser-induced plasmas: distributions of neutral atom and ion densities," Applied Physics A **79**, 1145–1148 (2004).

[252] M. Capitelli, A. Casavola, G. Colonna, and A. De Giacomo, "Laser-induced plasma expansion: theoretical and experimental aspects," Spectrochimica Acta Part B: Atomic Spectroscopy **59**, 271–289 (2004).

[253] G. Cristoforetti, E. Tognoni, and L. Gizzi, "Thermodynamic equilibrium states in laser-induced plasmas: from the general case to laser-induced breakdown spectroscopy plasmas," Spectrochimica Acta Part B: Atomic Spectroscopy **90**, 1–22 (2013).

[254] A. Kramida, Y. Ralchenko, J. Reader, and N. A. Team, "NIST atomic spectra database (ver. 5.6.1)," (2018).

[255] R. Noll, "Laser-induced breakdown spectroscopy," in "Laser-Induced Breakdown Spectroscopy," (Springer, 2012), pp. 7–15.

[256] H. R. Griem, Plasma Spectroscopy (McGraw-Hill, 1964).

[257] J. Cooper, "Plasma spectroscopy," Reports on Progress in Physics **29**, 35 (1966).

[258] B. Le Drogoff, J. Margot, M. Chaker, M. Sabsabi, O. Barthelemy, T. Johnston, S. Laville, F. Vidal, and Y. Von Kaenel, "Temporal characterization of femtosecond laser pulses induced plasma for spectrochemical analysis of aluminum alloys," Spectrochimica acta part B: Atomic spectroscopy **56**, 987–1002 (2001).

[259] E. Tognoni and G. Cristoforetti, "Signal and noise in laser induced breakdown spectroscopy: An introductory review," Optics & Laser Technology **79**, 164–172 (2016).

[260] A. Filipiak-Szok, M. Kurzawa, and E. Szłyk, "Determination of toxic metals by ICP-MS in Asiatic and European medicinal plants and dietary supplements," Journal of Trace Elements in Medicine and Biology **30**, 54–58 (2015).

[261] J. Scaffidi, J. Pender, W. Pearman, S. R. Goode, B. W. Colston, J. C. Carter, and S. M. Angel, "Dual-pulse laser-induced breakdown spectroscopy with combinations of femtosecond and nanosecond laser pulses," Applied optics **42**, 6099–6106 (2003).

[262] L. Guo, W. Hu, B. Zhang, X. He, C. Li, Y. Zhou, Z. Cai, X. Zeng, and Y. Lu, "Enhancement of optical emission from laser-induced plasmas by combined spatial and magnetic confinement," Optics express **19**, 14067–14075 (2011).

[263] Y. Liu, M. Baudelet, and M. Richardson, "Elemental analysis by microwave-assisted laser-induced breakdown spectroscopy: Evaluation on ceramics," Journal of Analytical Atomic Spectrometry **25**, 1316–1323 (2010).

[264] B. Kearton and Y. Mattley, "Laser-induced breakdown spectroscopy: Sparking new applications," Nature photonics **2**, 537 (2008).

[265] Y. Liu, B. Bousquet, M. Baudelet, and M. Richardson, "Improvement of the sensitivity for the measurement of copper concentrations in soil by microwave-assisted laser-induced breakdown spectroscopy," Spectrochimica Acta Part B: Atomic Spectroscopy **73**, 89–92 (2012).

[266] Y. Ikeda and R. Tsuruoka, "Characteristics of microwave plasma induced by lasers and sparks," Applied optics **51**, B183–B191 (2012).

[267] Y. Ikeda and R. Tsuruoka, "Microwave-enhanced emission intensity and plasma lifetime in laser-induced breakdown spectroscopy," in "50th AIAA Aerospace Sciences Meeting including the New Horizons Forum and Aerospace Exposition," (2015), p. 993.

[268] A. Khumaeni, T. Motonobu, A. Katsuaki, M. Masabumi, and W. Ikuo, "Enhancement of LIBS emission using antenna-coupled microwave," Optics express **21**, 29755–29768 (2013).

[269] M. Tampo, M. Miyabe, K. Akaoka, M. Oba, H. Ohba, Y. Maruyama, and I. Wakaida, "Enhancement of intensity in microwave-assisted laser-induced breakdown spectroscopy for remote analysis of nuclear fuel recycling," Journal of Analytical Atomic Spectrometry **29**, 886–892 (2014).

[270] S. J. Chen, A. Iqbal, M. Wall, C. Fumeaux, and Z. T. Alwahabi, "Design and application of near-field applicators for efficient microwave-assisted laser-induced breakdown spectroscopy," Journal of Analytical Atomic Spectrometry **32**, 1508–1518 (2017).

[271] M. Wall, Z. Sun, and Z. T. Alwahabi, "Quantitative detection of metallic traces in water-based liquids by microwave-assisted laser-induced breakdown spectroscopy," Optics Express **24**, 1507–1517 (2016).

[272] A. Iqbal, Z. Sun, M. Wall, and Z. T. Alwahabi, "Sensitive elemental detection using microwave-assisted laser-induced breakdown imaging," Spectrochimica Acta Part B: Atomic Spectroscopy **136**, 16–22 (2017).

[273] W. Woo and J. DeGroot, "Microwave absorption and plasma heating due to microwave breakdown in the atmosphere," The Physics of Fluids **27**, 475–487 (1984).

[274] W. Bollen, C. Yee, A. Ali, M. Nagurney, and M. Read, "High-power microwave energy coupling to nitrogen during breakdown," Journal of applied physics **54**, 101–106 (1983).

[275] M. A. Gigosos, M. Á. González, and V. Cardeñoso, "Computer simulated Balmer-alpha,-beta and-gamma Stark line profiles for non-equilibrium plasmas diagnostics," Spectrochimica Acta Part B: Atomic Spectroscopy **58**, 1489–1504 (2003).

[276] N. Kawahara, J. Beduneau, T. Nakayama, E. Tomita, and Y. Ikeda, "Spatially, temporally, and spectrally resolved measurement of laser-induced plasma in air," Applied Physics B **86**, 605–614 (2007).

[277] W. Baum, "Ore characterization, process mineralogy and lab automation a roadmap for future mining," Minerals Engineering **60**, 69–73 (2014).

[278] A. Michalakou, P. Stavropoulos, and S. Couris, "Laser-induced breakdown spectroscopy in reactive flows of hydrocarbon-air mixtures," Applied Physics Letters **92**, 081501 (2008).

[279] J. Kiefer, J. Tröger, Z. Li, and M. Aldén, "Laser-induced plasma in methane and dimethyl ether for flame ignition and combustion diagnostics," Applied Physics B **103**, 229–236 (2011).

[280] A. E. Majd, A. S. Arabanian, R. Massudi, and M. Nazeri, "Spatially resolved laser - induced breakdown spectroscopy in methane-air diffusion flames," Applied spectroscopy **65**, 36–42 (2011).

[281] M. S. Mansour, H. Imam, K. A. Elsayed, and W. Abbass, "Local equivalence ratio measurements in turbulent partially premixed flames using laser-induced breakdown spectroscopy," Spectrochimica Acta Part B: Atomic Spectroscopy **64**, 1079–1084 (2009).

[282] T. Badawy, M. Hamza, M. S. Mansour, A.-H. H. Abdel-Hafez, H. Imam, M. A. Abdel-Raheem, C. Wang, and T. Lattimore, "Lean partially premixed turbulent flame equivalence ratio measurements using laser-induced breakdown spectroscopy," Fuel **237**, 320–334 (2019).

[283] L. Merotto, M. Sirignano, M. Commodo, A. D'Anna, R. Dondé, and S. De Iuliis, "Experimental characterization and modeling for equivalence ratio sensing in non-premixed flames using chemiluminescence and laser-induced breakdown spectroscopy techniques," Energy & Fuels **31**, 3227–3233 (2017).

[284] H. M. Jun, J. H. Kim, S. H. Lee, and J. J. Yoh, "Towards simplified monitoring of instantaneous fuel concentration in both liquid and gas fueled flames using a combustor injectable LIBS plug," Energy **160**, 225–232 (2018).

[285] Z. Shi, Y. Hardalupas, and A. Taylor, "Local equivalence ratio measurement in opposed jet flames of premixed and non-premixed methane-air using laser-induced breakdown spectroscopy," in "Proceedings of 18th International

Symposium on the Application of Laser and Imaging Techniques to Fluid Mechanics," (2016).

[286] F. Ferioli, P. V. Puzinauskas, and S. G. Buckley, "Laser-induced breakdown spectroscopy for on-line engine equivalence ratio measurements," Applied spectroscopy **57**, 1183–1189 (2003).

[287] S. H. Lee, H. Do, and J. J. Yoh, "Simultaneous optical ignition and spectroscopy of a two-phase spray flame," Combustion and flame **165**, 334–345 (2016).

[288] K. M. Rahman, N. Kawahara, D. Matsunaga, E. Tomita, Y. Takagi, and Y. Mihara, "Local fuel concentration measurement through spark-induced breakdown spectroscopy in a direct-injection hydrogen spark-ignition engine," International Journal of Hydrogen Energy **41**, 14283–14292 (2016).

[289] J. Kiefer, J. W. Tröger, Z. Li, T. Seeger, M. Alden, and A. Leipertz, "Laser-induced breakdown flame thermometry," Combustion and flame **159**, 3576–3582 (2012).

[290] W. Wu, A. Adeosun, and R. L. Axelbaum, "A new method of flame temperature measurement utilizing the acoustic emissions from laser-induced plasmas," Proceedings of the Combustion Institute (2018).

[291] Y. He, J. Zhu, B. Li, Z. Wang, Z. Li, M. Aldén, and K. Cen, "In-situ measurement of sodium and potassium release during oxy-fuel combustion of lignite using laser-induced breakdown spectroscopy: effects of O_2 and CO_2 concentration," Energy & Fuels **27**, 1123–1130 (2013).

[292] Z.-h. Zhang, Q. Song, Z. T. Alwahabi, Q. Yao, and G. J. Nathan, "Temporal release of potassium from pinewood particles during combustion," Combustion and Flame **162**, 496–505 (2015).

[293] L.-J. Hsu, Z. T. Alwahabi, G. J. Nathan, Y. Li, Z. Li, and M. Aldén, "Sodium and potassium released from burning particles of brown coal and pine wood in a laminar premixed methane flame using quantitative laser-induced breakdown spectroscopy," Applied spectroscopy **65**, 684–691 (2011).

[294] A. Molina, P. M. Walsh, C. R. Shaddix, S. M. Sickafoose, and L. G. Blevins, "Laser-induced breakdown spectroscopy of alkali metals in high-temperature gas," Applied optics **45**, 4411–4423 (2006).

[295] A. M. Popov, F. Colao, and R. Fantoni, "Enhancement of LIBS signal by spatially confining the laser-induced plasma," Journal of Analytical Atomic Spectrometry **24**, 602–604 (2009).

[296] A. M. Popov, F. Colao, and R. Fantoni, "Spatial confinement of laser-induced plasma to enhance LIBS sensitivity for trace elements determination in soils," Journal of Analytical Atomic Spectrometry **25**, 837–848 (2010).

[297] L. Guo, C. Li, W. Hu, Y. Zhou, B. Zhang, Z. Cai, X. Zeng, and Y. Lu, "Plasma confinement by hemispherical cavity in laser-induced breakdown spectroscopy," Applied Physics Letters **98**, 131501 (2011).

[298] L. Guo, Z. Hao, M. Shen, W. Xiong, X. He, Z. Xie, M. Gao, X. Li, X. Zeng, and Y. Lu, "Accuracy improvement of quantitative analysis by spatial confinement in laser-induced breakdown spectroscopy," Optics express **21**, 18188–18195 (2013).

[299] X. Shen, Y. Lu, a. T. Gebre, H. Ling, and Y. Han, "Optical emission in magnetically confined laser-induced breakdown spectroscopy," Journal of applied physics **100**, 053303 (2006).

[300] Z. Hou, Z. Wang, J. Liu, W. Ni, and Z. Li, "Combination of cylindrical confinement and spark discharge for signal improvement using laser induced breakdown spectroscopy," Optics express **22**, 12909–12914 (2014).

[301] L. Guo, B. Zhang, X. He, C. Li, Y. Zhou, T. Wu, J. Park, X. Zeng, and Y. Lu, "Optimally enhanced optical emission in laser-induced breakdown spectroscopy by combining spatial confinement and dual-pulse irradiation," Optics express **20**, 1436–1443 (2012).

[302] V. Babushok, F. DeLucia Jr, J. Gottfried, C. Munson, and A. Miziolek, "Double pulse laser ablation and plasma: Laser induced breakdown spectroscopy signal enhancement," Spectrochimica Acta Part B: Atomic Spectroscopy **61**, 999–1014 (2006).

[303] D. N. Stratis, K. L. Eland, and S. M. Angel, "Dual-pulse LIBS using a pre-ablation spark for enhanced ablation and emission," Applied Spectroscopy **54**, 1270–1274 (2000).

[304] D. K. Killinger, S. D. Allen, R. D. Waterbury, C. Stefano, and E. L. Dottery, "Enhancement of Nd:YAG LIBS emission of a remote target using a simultaneous CO_2 laser pulse," Optics Express **15**, 12905–12915 (2007).

[305] O. A. Nassef and H. E. Elsayed-Ali, "Spark discharge assisted laser induced breakdown spectroscopy," Spectrochimica Acta Part B: Atomic Spectroscopy **60**, 1564–1572 (2005).

[306] W. Zhou, K. Li, Q. Shen, Q. Chen, and J. Long, "Optical emission enhancement using laser ablation combined with fast pulse discharge," Optics express **18**, 2573–2578 (2010).

[307] L. Liu, S. Li, X. N. He, X. Huang, C. F. Zhang, L. S. Fan, M. X. Wang, Y. S. Zhou, K. Chen, L. Jiang, J.-F. Silvain, and Y. F. Lu, "Flame-enhanced laser-induced breakdown spectroscopy," Optics express **22**, 7686–7693 (2014).

[308] L. Liu, X. Huang, S. Li, Y. Lu, K. Chen, L. Jiang, J.-F. Silvain, and Y. F. Lu, "Laser-induced breakdown spectroscopy enhanced by a micro torch," Optics express **23**, 15047–15056 (2015).

ORIGINAL PAPERS

Paper I

Rate Constant and Thermochemistry for K+ O_2+ N_2= KO_2+ N_2

by
Tapio Sorvajärvi, Jan Viljanen, Juha Toivonen,
Paul Marshall, and Peter Glarborg
The Journal of Physical Chemistry A 119(14), 3329-3336 (2015)

THE JOURNAL OF PHYSICAL CHEMISTRY A

Article

pubs.acs.org/JPCA

Rate Constant and Thermochemistry for K + O_2 + N_2 = KO_2 + N_2

Tapio Sorvajärvi,[†] Jan Viljanen,[†] Juha Toivonen,[†] Paul Marshall,*[,‡] and Peter Glarborg[§]

[†]Optics Laboratory, Department of Physics, Tampere University of Technology, P.O. Box 692, FI-33101 Tampere, Finland

[‡]Department of Chemistry and Center for Advanced Scientific Computing and Modeling (CASCaM), University of North Texas, 1155 Union Circle #305070, Denton, Texas 76203−5017, United States

[§]Department of Chemical and Biochemical Engineering, Technical University of Denmark, DK-2800 Kgs. Lyngby, Denmark

Supporting Information

ABSTRACT: The addition reaction of potassium atoms with oxygen has been studied using the collinear photofragmentation and atomic absorption spectroscopy (CPFAAS) method. KCl vapor was photolyzed with 266 nm pulses and the absorbance by K atoms at 766.5 nm was measured at various delay times with a narrow line width diode laser. Experiments were carried out with O_2/N_2 mixtures at a total pressure of 1 bar, over 748−1323 K. At the lower temperatures single exponential decays of [K] yielded the third-order rate constant for addition, k_{R1}, whereas at higher temperatures equilibration was observed in the form of double exponential decays of [K], which yielded both k_{R1} and the equilibrium constant for KO_2 formation. k_{R1} can be summarized as $1.07 \times 10^{-30}(T/1000\ \mathrm{K})^{-0.733}$ cm^6 molecule^{-2} s^{-1}. Combination with literature values leads to a recommended k_{R1} of $5.5 \times 10^{-26} T^{-1.55} \exp(-10/T)$ cm^6 molecule^{-2} s^{-1} over 250−1320 K, with an error limit of a factor of 1.5. A van't Hoff analysis constrained to fit the computed ΔS_{298} yields a K−O_2 bond dissociation enthalpy of 184.2 ± 4.0 kJ mol^{-1} at 298 K and $\Delta_f H_{298}(KO_2) = -95.2 \pm 4.1$ kJ mol^{-1}. The corresponding D_0 is 181.5 ± 4.0 kJ mol^{-1}. This value compares well with a CCSD(T) extrapolation to the complete basis set limit, with all electrons correlated, of 177.9 kJ mol^{-1}.

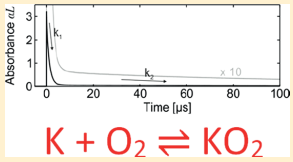

INTRODUCTION

The high-temperature chemistry of alkali metal species has important implications for combustion. It is well established that the presence of alkali metal species may result in flame inhibition[1,2] and alkali-based flame inhibitors are of interest.[3,4] Potassium additives are also known to have an impact on gun muzzle flash.[5] Furthermore, most solid fuels contain alkali metals in minor quantities. Biomass such as wood and annual crops releases potassium to the vapor phase during pyrolysis and combustion,[6−8] mainly in the form of KCl. Once released, the alkali metal chlorides may be partially converted to alkali metal hydroxide or alkali metal sulfates.[9] During cooling, the alkali metal components will condense, contributing to aerosol formation and/or cause operational problems, such as deposit formation and corrosion in boilers.[10,11] The fate of the alkali metal will depend on interactions with the sulfur and chlorine species of the gas.

Formation of potassium superoxide, KO_2, is potentially important for both flame inhibition and the high-temperature K/S/Cl transformation in combustion. The ability of alkali metals to catalyze radical removal is well documented by data from laminar premixed flames[12−25] and flow reactor experiments.[26] Alkali-metal-based flame inhibitors are typically added as particulates[3,4] and heterogeneous effects have been proposed; however, the inhibiting effect of alkali metals is attributed mostly to gas phase radical removal reactions. The mechanism of inhibition is still in discussion. Under reducing conditions, results from flames[16,17,21] and from flow reactors[26] are consistent with the sequence (for K): KOH/KCl + H → K + H_2O/HCl, K + OH + M → KOH + M. In combustion systems, alkali metal chlorides and alkali metal hydroxides are rapidly equilibrated through the fast reaction KCl + H_2O ⇌ KOH + HCl.[9] Under lean conditions, the inhibition mechanism is more uncertain. The chain-terminating recombination reaction,

$$\mathrm{K} + \mathrm{O_2} + \mathrm{M} \rightleftharpoons \mathrm{KO_2} + \mathrm{M} \qquad \text{(R1)}$$

has been suggested to be important.[18,27−29] However, it has been questioned whether potassium superoxide was sufficiently stable to play an important role under flame conditions.[2,26]

Formation of alkali metal superoxides (mainly KO_2) may also play a role in the gas-phase transformation of alkali metal, sulfur, and chlorine species in solid fuel combustion. Provided KO_2 is sufficiently stable, it could promote oxidation of SO_2 to SO_3 through the reaction $SO_2 + KO_2 \rightarrow SO_3 + KO$, which has been estimated to be fast.[30]

The importance of KO_2 in combustion depends on the rate constant for K + O_2 + M (R1) and on the thermal stability of KO_2. Values of k_{R1} have been measured directly in the temperature range 250−1100 K,[31−34] inferred from studies of lean premixed flames,[27−29] and calculated theoretically.[35] The direct measurements are in reasonably good agreement but deviate significantly from the values derived at high temperatures from flames. Also the thermochemistry of KO_2 is in

Received: January 24, 2015
Revised: March 14, 2015
Published: March 16, 2015

DOI: 10.1021/acs.jpca.5b00755
J. Phys. Chem. A 2015, 119, 3329−3336

discussion. Values for the bond dissociation energy D_0 of KO_2 have been inferred from flame studies,[18,36] a molecular beam study,[37] time-resolved decay of atomic potassium,[34] and from theory.[34,38−40] Although recent theoretical studies imply a value of the BDE of approximately 172 ± 4 kJ mol^{-1},[38−40] some data inferred from experiment indicate a substantially larger value.[34,37]

The objective of the present work is to extend the measurement range for the rate constant for K + O_2 + N_2 to higher temperatures compared to previous direct studies, and to provide the first direct measurements of the bond dissociation energy of KO_2. For this purpose we use the recently developed optical technique called collinear photofragmentation and atomic absorption spectroscopy (CPFAAS). This technique is based on the fragmentation of a precursor molecule and the detection of the fragment atoms via absorption spectroscopy.[41,42] It has been applied to monitor concentrations of the precursors KCl and KOH in combustion during combustion of solid biomass fuels,[43] but to our knowledge the present work is its first application to chemical kinetics. Previous CPFAAS studies have focused on the maximum absorbance right after the photofragmentation that is proportional to the precursor molecule concentration. The decay process of the induced K atoms has been assumed to be exponential and was not studied in detail. In the present work, measurements analogous to CPFAAS experiments are performed to study the decay process of [K] in the temperature range of 748−1323 K and in atmospheres containing O_2 from 40 ppm to 21.4%.

EXPERIMENTAL SECTION

Potassium atoms were produced and detected using a measurement setup presented in Figure 1. The K atoms were formed through photofragmentation of KCl molecules in an 80 cm long quartz sample tube having an inner diameter of 35 mm. The KCl powder was brought into the middle of the cell in a 10 cm long glazed combustion boat. The temperature of the sample tube was adjusted with a 50 cm long and 30 cm wide tube oven. The gas atmosphere in the tube was adjusted by flushing the tube for 5 min before each experiment with a gas mixture prepared by diluting dry synthetic air with nitrogen using a mass flow controller (5850S, Brooks Instruments). A gas flow of 2 standard liters per minute (L min^{-1}) was brought to the tube from the entrance side of the probe laser and 0.2 L min^{-1} from the exhaust side of the tube. The small flow at the exhaust side prevented the deposition of the KCl vapor on the inner surface of the exit window of the cell. The gas flows were closed 2 min before recording the decay of the K atoms. The sample was at atmospheric pressure during the measurement.

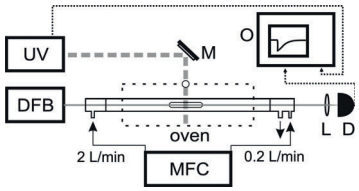

Figure 1. Experimental setup for the time-resolved detection of photoinduced potassium atoms: photofragmentation laser (UV); probe laser (DFB); mirror (M); lens (L); detector (D); oscilloscope (O); mass flow controller (MFC).

The dissociation of the KCl molecules was performed by applying a fragmentation laser (FQSS 266-200, Crylas GmbH). It emitted 1 ns long pulses with a 20 Hz repetition rate at a wavelength of 266 nm. The laser pulses entered the sample tube through an 18 mm hole at the side of the oven and through the wall of the tube. The transmission of the wall material for the fragmentation wavelength was measured to be approximately 80%. The pulse energies of the fragmentation laser in the sample tube were adjusted to between 1 and 80 μJ, and the cross sectional 1/e diameter of the pulses was adjusted over the range of 3−10 mm, such that detected probe beam transmission did not drop to zero. The energy densities of the UV pulses in the tube were smaller than the saturation intensity of KCl.[44] The pulses were slightly focused with a lens prior to the entrance hole to increase the concentration of the released K atoms at the lower temperatures (<873 K) when the vapor pressure of KCl was small. The pulses traveled 10 mm above the top of the combustion boat and were dumped to the back wall of the oven.

The relative concentration of the K atoms was measured by applying a narrow line width distributed feedback diode laser (Nanoplus GmbH), which emitted light at a wavelength of 766.5 nm (in air). The wavelength of the diode laser was locked to the absorption line of K atoms in a reference cell (SC-K-19 × 75-Q-W, Photonics Technologies).[42] The probe beam having a 1/e diameter of 1 mm was aligned to travel through the tube and to cross the volume affected by the fragmentation pulses. The optical path of the probe laser beam and the fragmentation pulses were perpendicular to each other in the tube. The short interaction region meant that the temperature was constant across it, despite any overall temperature gradients along the entire sample tube. The induced K atoms decreased the transmission intensity of the probe beam temporarily. The transmission waveform caused by the photofragmentation was detected using an amplified photodiode (PDA10A, Thorlabs) and a 12-bit oscilloscope (HDO6054, LeCroy).

An example waveform measured at a temperature of 1173 K in 2.67% of O_2 is presented in Figure 2a. The photofragmentation of KCl molecules took place at t = 0, and it is seen as a fast dip in the photodiode (PD) voltage due to the temporarily increased absorption by the K atoms. The fragmentation was followed by recovery of the transmission as the induced K atoms reacted with ambient gas molecules and the distorted gas volume approached equilibrium.

To study the recovery process of the concentration of K atoms, the PD voltage was converted to the absorbance αL by applying the Beer−Lambert law,

$$\alpha L = -\ln[I(t)/I(t<0)] \quad (1)$$

Figure 2b shows the corresponding absorbance curve calculated using eq 1. The absorbance is directly proportional to the sample concentration and the conversion can be done when absorption length and absorption cross section are known. The effective absorption length in this measurement was 1 cm (UV beam diameter) and the absorption cross section of K atoms at the wavelength in question is 1.25×10^{-16} m^2,[43] which converts an absorbance equal to 1 to a K concentration of 130 ppb. At the lower end of the temperature range studied, the absorbance was observed to follow a single exponential decay,

$$\alpha L(t>0) = A_1 \exp(-k_1 t) \quad (2)$$

DOI: 10.1021/acs.jpca.5b00755
J. Phys. Chem. A 2015, 119, 3329−3336

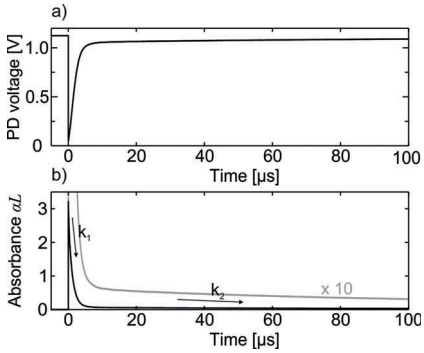

Figure 2. (a) Probe laser transmission curve. The dip is caused by the photofragmentation of KCl molecules. (b) Corresponding absorbance curve calculated from the transmission curve. The induced absorbance decays with two rate constants k_1 and k_2. The second phase decay is emphasized in (b) by magnifying the decay curve by a factor of 10. The experiment was done at a temperature of 1173 K in 2.67% of O_2 in N_2.

whereas at higher temperatures a double exponential decay process was observed,

$$\alpha L(t>0) = A_1 \exp(-k_1 t) + A_2 \exp(-k_2 t) \quad (3)$$

RESULTS AND DISCUSSION

At 1073 K and below simple exponential kinetics were observed, in the form of eq 2, which may be interpreted in terms of the scheme

$$K + O_2 \xrightarrow{k_a} KO_2 \quad (a)$$

$$K \xrightarrow{k_d} \text{loss} \quad (d)$$

k_a represents the effective second-order forward rate constant for reaction R1 and k_d accounts for loss of K atoms by processes that do not involve oxygen, such as diffusion. One would therefore expect the variation of potassium concentration with time t to follow eq 4,

$$[K] = [K]_0 \exp(-k_1 t) \quad (4)$$

where $k_1 = k_a[O_2] + k_d$. Figure 3 shows a plot of k_1 vs $[O_2]$, from which it may be seen that the expected linear dependence on $[O_2]$ from reaction (a) is exhibited, and that the intercept is negligible, so that on the short time scale of these experiments k_d is indistinguishable from zero. Details of k_1 and $[O_2]$ measurements are provided in the Supporting Information (Table S1), and the results for the third-order rate constant k_{R1} derived as the slope k_a divided by $[O_2] + [N_2]$ (corresponding to 1 bar total pressure) for 873−1073 K are listed in Table 1. Approximate, purely statistical, error limits were assessed via twice the standard deviation of the slopes of plots like Figure 3. At 748, 773, and 823 K single measurements of k_1 were made, and divided by $[O_2]$ and $[O_2] + [N_2]$ to obtain k_{R1}. We allow 25% error limits for these points, and also for a single measurement at 1323 K where black liquor (alkali-metal-rich waste product from pulp and paper processing) rather than KCl was the source of K atoms.

We now turn to the measurements made at the higher temperatures where double-exponential decays of absorbance

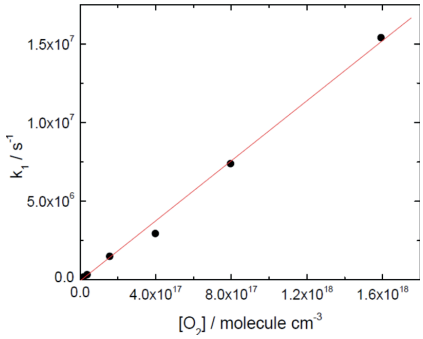

Figure 3. Exponential decay coefficient for potassium atoms as a function of oxygen concentration at 923 K and a total pressure of 1 bar made up with nitrogen.

Table 1. Summary of Measurements for K + O_2 + N_2

T/°C	T/K	$(k_{R1} \pm 2\sigma)/10^{-30}$ cm^6 molecule^{-2} s^{-1}	comment
475	748	1.47 ± 0.37	single point
500	773	1.31 ± 0.33	single point
550	823	1.24 ± 0.31	single point
600	873	1.18 ± 0.16	exponential decays
650	923	1.15 ± 0.04	exponential decays
700	973	1.07 ± 0.02	exponential decays
750	1023	0.998 ± 0.027	exponential decays
800	1073	0.789 ± 0.140	exponential decays
800	1073	0.978 ± 0.152	equilibrium mechanism
850	1123	0.982 ± 0.024	equilibrium mechanism
900	1173	0.969 ± 0.032	equilibrium mechanism
950	1223	0.973 ± 0.063	equilibrium mechanism
1000	1273	1.01 ± 0.07	equilibrium mechanism
1050	1323	0.919 ± 0.230	single point, black liquor

were seen. Figure 4 shows a temporal K concentration profile upon photofragmentation of the KCl molecules at a temperature of 1223 K in 10.7% O_2. In agreement with the results of Figure 2, [K] is observed to recover to its original level in two steps. In the first phase [K] decreases fast and the 1/e relaxation time constant $1/k_1$ is found to be 270 ns (Figure 4a). Figure 4b shows how [K] does not recover fully in the first phase and saturates to a nonzero level. Figure 4c presents how the second phase relaxation takes place on a time scale of the order of 100 μs. The 1/e decay time constant for the second phase relaxation was, in the example signal, $1/k_2 = 40$ μs.

This double-exponential behavior, quantified in the form of eq 3, can be observed when reactants reversibly form an intermediate, and a reactant and/or intermediate is also lost irreversibly.[45] In the absence of oxygen the lifetime of K was observed to be of the order of 1 ms, where K atoms are lost presumably mainly by diffusion out of the probe laser beam. This lifetime is too long to be significant on the time scale of the K atom profiles when O_2 is present. Accordingly, we have interpreted the results in terms of a simple mechanism

$$K + O_2 \xrightarrow{k_a} KO_2 \quad (a)$$

$$KO_2 \xrightarrow{k_{-a}} K + O_2 \quad (-a)$$

DOI: 10.1021/acs.jpca.5b00755
J. Phys. Chem. A 2015, 119, 3329−3336

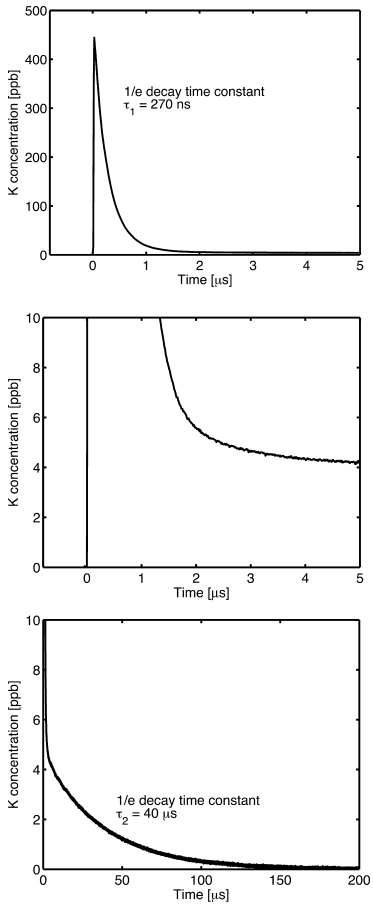

Figure 4. K relaxation after KCl photofragmentation at a temperature of 1223 K in 10.7% O_2: (a) first phase relaxation; (b) The concentration of K does not reach the original background level within first 5 μs. (c) The thermodynamic equilibrium [K] is reached 200 μs after the fragmentation. $[K]_0$ is the potassium concentration right after the photofragmentation, and $[K]_0^{res}$ is the concentration of the residual potassium atoms. This value is calculated by extrapolating the second phase recovery to $t = 0$. $\tau_1 = 1/k_1$ and $\tau_2 = 1/k_2$ are the recovery time constants in the fitting equation $[K]_t = ([K]_0 - [K]_0^{res}) \exp(-t/\tau_1) + [K]_0^{res} \exp(-t/\tau_2)$.

$$KO_2 \xrightarrow{k_b} \text{loss} \quad \text{(b)}$$

k_a represents the effective second-order rate constant for K atom addition to O_2 at a given total pressure, k_{-a} is the effective first-order dissociation rate of KO_2, and k_b is the effective first-order rate of loss of KO_2 by pathways that do not regenerate K atoms. These include diffusive loss of KO_2 although presumably this is even slower than the neglected diffusive loss of K atoms. Assuming $[O_2] \gg [K]_0$, the integrated rate law may be written as[45]

$$[K] = \frac{[K]_0}{\lambda_1 - \lambda_2}((Q + \lambda_1)e^{\lambda_1 t} - (Q + \lambda_2)e^{\lambda_2 t}) \quad (5)$$

with

$$Q = k_{-a} + k_b \quad (6)$$

$$\lambda_1 + \lambda_2 = -Q - k_a[O_2] \quad (7)$$

$$\lambda_1\lambda_2 = k_b k_a[O_2] \quad (8)$$

By comparing terms with the empirical eq 3, we see that the three rate constants may be derived via

$$[K]_0 = A_1 + A_2 \quad (9)$$

$$Q = k_1 + \frac{A_1(k_2 - k_1)}{[K]_0} \quad (10)$$

$$k_a[O_2] = k_1 + k_2 - Q \quad (11)$$

$$k_b = \frac{k_1 k_2}{k_a[O_2]} \quad (12)$$

$$k_{-a} = Q - k_b \quad (13)$$

This analysis was applied to the double exponential data obtained over 1073−1273 K. A check on the consistency of the analysis is that the $k_a[O_2]$ term should vary linearly with $[O_2]$ and k_{-a} should be independent of $[O_2]$. Figure 5 shows the

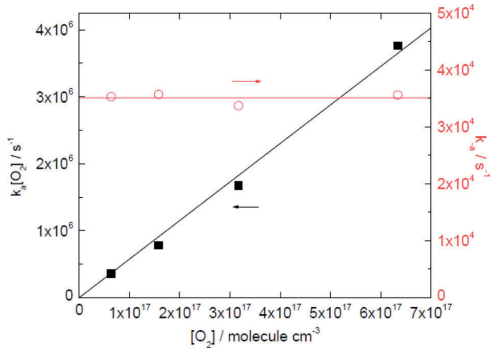

Figure 5. Effective first-order rate constants at 1223 K for K addition to O_2 (solid black squares, left axis, linear fit constrained to pass through the origin) and for KO_2 dissociation (open red circles, right axis, linear fit constrained to have zero slope).

results at 1223 K, and it may be seen that these conditions are met. A second check is that at 1073 K, low $[O_2]$ led to double-exponential behavior whereas at high $[O_2]$ the equilibrium is shifted sufficiently toward products that the back-reaction is negligible, leading to single exponential decays of [K]. Data obtained both ways are tabulated for comparison, but unfortunately, at this temperature neither method works very well because $k_a[O_2]$ and k_{-a} are not well-separated. The results are given in Table S1 (Supporting Information) where we report the slope of $k_a[O_2]$ vs $[O_2]$ plots constrained to pass through the origin, and the mean of the k_{-a} values. Again, k_{R1} is obtained by dividing k_a by $[N_2] + [O_2] \approx [N_2]$ and is listed in Table 1.

The present rate constants can be summarized as $k_{R1} = 1.07 \times 10^{-30}(T/1000\ \text{K})^{-0.733}$ cm^6 molecule^{-2} s^{-1} over 750−1320 K. They are in reasonable accord with the prior determinations up to 1100 K plotted on Figure 6 but the rate coefficients do not

DOI: 10.1021/acs.jpca.5b00755
J. Phys. Chem. A 2015, 119, 3329−3336

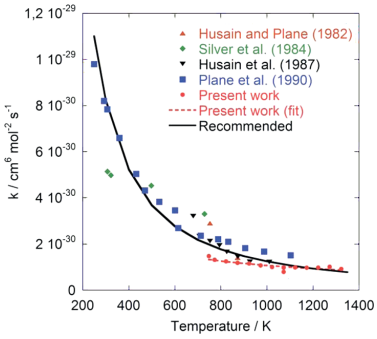

Figure 6. Arrhenius plot for the reaction K + O_2 + N_2 ⇌ KO_2 + N_2. The symbols denote the experimental data from Husain and Plane,[32] Silver et al.,[31] Husain et al.,[33] Plane et al.[34] and from the present work. The dashed line shows a best fit to the present data (k_{R1} = 1.07 × $10^{-30}(T/1000\ K)^{-0.733}$ cm^6 $molecule^{-2}$ s^{-1} (750−1320 K), and the solid line shows the recommended k_{R1} of 5.5 × $10^{-26}T^{-1.55}$ exp(−10/T) cm^6 $molecule^{-2}$ s^{-1} over 250−1320 K.

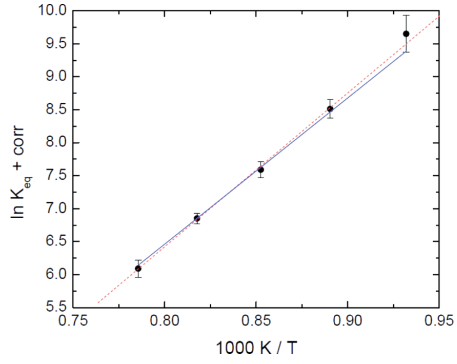

Figure 7. van't Hoff plot of K_{eq} for K + O_2 ⇌ KO_2. A second-law fit is shown as the dashed red line and a third-law fit is shown as the solid blue line.

extrapolate well to lower temperatures. An overall fit to the data of the present work together with those of Husain and Plane,[32] Husain et al.,[33] and Plane et al.[34] leads to a recommended k_{R1} of 5.5 × $10^{-26}T^{-1.55}$ exp(−10/T) cm^6 $molecule^{-2}$ s^{-1} over 250−1320 K. An error limit of a factor of 1.5 includes most of the present and past measurements.

The ratio k_a/k_{-a} equals the concentration equilibrium constant K_c, which is listed in Table 2, along with the thermodynamic equilibrium constant K_{eq} based on unit activity for a standard pressure of 1 bar. A van't Hoff plot for K_{eq} yields thermodynamic information for reaction R1. A potential complication is the temperature dependence of ΔH and ΔS. A correction term to ln K_{eq} of $(\Delta H_T - \Delta H_{298})/RT - (\Delta S_T - \Delta S_{298})/R$ was added so that the slope and intercept of the van't Hoff plot in Figure 7 correspond to $-\Delta H_{298}/R$ and $\Delta S_{298}/R$, respectively. This small correction was derived via statistical mechanics from the experimental properties of K and O_2,[46] the KO_2 vibrational frequencies of 1109, 307, and 304 cm^{-1} [47] and the ab initio C_{2v} geometry of Vasiliu et al.,[40] a K−O distance of 2.40 × 10^{-10} m, and a OKO angle of 32.5°. The correction varied from −0.016 at 1073 K to −0.031 at 1323 K. The unconstrained linear fit corresponds to a second-law analysis and yields ΔS_{298} = −101.7 ± 9.9 J K^{-1} mol^{-1} and ΔH_{298} = −193.8 ± 11.9 kJ mol^{-1}. The error limits are 2σ and are purely the statistical uncertainty of the fit. A third-law analysis constrains the intercept to the separately estimated ΔS_{298} = 93.6 J K^{-1} mol^{-1} and yields ΔH_{298} = −184.2 ± 0.5 kJ mol^{-1}.

Table 2. Equilibrium Constants Derived from Forward and Reverse Kinetics (See Text)

T/K	$K_c/10^{-16}$ cm^3 $molecule^{-1}$	K_{eq} std state 1 bar	correction[a]	ln(K_{eq}) + corr	σ[b]
1073	23.5	1.59 × 10^4	−0.016	9.65	0.28
1123	7.87	5.08 × 10^3	−0.017	8.51	0.14
1173	3.28	2.03 × 10^3	−0.021	7.59	0.12
1223	1.64	971	−0.027	6.85	0.08
1273	0.799	455	−0.031	6.09	0.13

[a]Equal to $(\Delta H_T - \Delta H_{298})/RT - (\Delta S_T - \Delta S_{298})/R$. [b]Statistical uncertainty in ln(K_{eq}).

The thermodynamic parameters agree between both methods, but as expected, the third-law method is more precise. Combined with $\Delta_f H_{298}$ = 89.0 ± 0.8 kJ mol^{-1} for atomic potassium,[46] the corresponding heat of formation of KO_2 is $\Delta_f H_{298}$ = −95.2 ± 4.1 kJ mol^{-1}. The experimental vibrational frequencies for KO_2 yield $H_{298} - H_0$ = 12.14 kJ mol^{-1}, and together with $H_{298} - H_0$ of 6.20 and 8.68 kJ mol^{-1} for K and O_2, respectively,[46] we obtain the 0 K bond strength D_0(K−O_2) as 181.5 kJ mol^{-1}. This value is compared with experimental and theoretical results from the literature in Table 3.

Table 3. Reported Bond Dissociation Energies for KO_2 and Comparison with the Present Values

reference	D_0/kJ mol^{-1}	method
Jensen[36]	170 ± 30	flame study
Figger et al.[37]	188 ± 10	molecular beam study
Hynes et al.[18]	174 ± 20	flame study
Plane et al.[34]	≥203	time resolved decay (LIF)
Plane et al.[34]	154	theory
Partridge et al.[38]	170 ± 8	theory
Lee and Wright[39]	168 ± 3	theory
Vasiliu et al.[40]	173	theory
Present work	181.5 ± 4	CPFAAS
Present work	177.9	theory

There remains the issue of systematic error. A rough-and-ready approach is based on the ca. factor of 1.5 differences between literature determinations of k_a which, if propagated as a factor of 1.5 variation in K_{eq}, imply a variation of ±4 kJ mol^{-1} in ΔH_{298}. With this as an uncertainty limit, the 298 K bond strength is 8.7 kJ mol^{-1} above that calculated by Vasiliu et al.[40] and is therefore significantly different.

AB INITIO ANALYSIS

It is common to exclude core electrons from the correlation treatment in ab initio analysis. For a potassium atom, these would be the 1s, 2s, 2p, 3s, and 3p orbitals. However, in an ionic compound like KO_2 the potassium loses its only valence 4s electron so the remaining interactions involve the core electrons. Indeed, the 3s and 3p atomic orbitals may be higher in energy than the oxygen orbitals. For this reason it has become standard practice in calculations on alkali metals to

DOI: 10.1021/acs.jpca.5b00755
J. Phys. Chem. A 2015, 119, 3329−3336

Table 4. Computed Reaction Enthalpies at 0 K in the KO_2 System, with Contributions from Each Term, in kJ mol^{-1}

reaction	Δ(CCSD(T)/aug-cc-pwCVQZ)	Δ(CCSD(T)/aug-cc-pwCV5Z)	ΔE_{inf}	ΔE_{zpe}	ΔE_{rel}	ΔE_{final}
D_0(ions)	555.32	556.27	557.27	−3.92	0.91	553.35[a]
D_0	175.64	177.96	180.39	−1.11	−1.36	177.92
IP(K)	416.58	416.67	416.76	0.00	1.39	418.15
−EA(O_2)	−36.91	−38.36	−39.88	−2.81	0.88	−42.73[a]

[a]Includes empirical −0.91 kJ mol^{-1} correction to the energy of O_2^- for splitting in its $^2\Pi$ ground state.[53]

incorporate some of these inner orbitals in the correlation space[48] and, in particular, Vasilu et al.[40] included the 3s and 3p electrons in their correlation treatment at the coupled cluster level, CCSD(T), for potassium compounds.

In this work the geometries of O_2, O_2^-, and KO_2 were obtained using coupled cluster theory and the large aug-cc-pwCVQZ atomic basis set for oxygen[49] and specially constructed for potassium by Peterson and co-workers,[50] with all the electrons correlated. The optimized O−O distances in the three molecules are 0.121, 0.135, and 0.135 nm, consistent with a $K^+O_2^-$ species where there is charge transfer to the oxygen. In KO_2 the computed K−O distance is 0.240 nm. Then single-point energies were derived with CCSD(T)/aug-cc-pwCV5Z theory,[50] again with all electrons correlated, followed by a scalar relativistic correction Erel (mass-velocity plus Darwin terms) performed at the CISD/aug-cc-pwCVQZ level of theory. These calculations were made with the Molpro 2010 program,[51] and the results are listed in Table S2 (Supporting Information). The CCSD(T) results with ζ = 4 and 5 were extrapolated to the infinite basis set limit via the relation:[52]

$$E_{inf} = (125 \cdot E_5 - 64 \cdot E_4)/61 \quad (14)$$

Vibrational zero-point energies E_{zpe} were derived from experimental data (KO_2;[47] O_2 and O_2^- [53]). The final energies (E_{inf} + E_{rel} + E_{zpe}) were employed to derive 0 K enthalpy changes for the reactions in Table 4, which are coupled via the Hess cycle

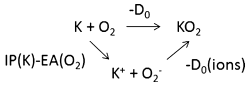

It may be seen that that the ionization potential of K is close to converged with the aug-cc-pwCVQZ basis set and that the final extrapolation is very small, only 0.09 kJ mol^{-1}, and with the relativistic correction we compute IP(K) = 418.15 kJ mol^{-1}, which is 0.66 kJ mol^{-1} below the experimental value of 418.81 kJ mol^{-1}.[56] Similarly, the dissociation enthalpy of KO_2 to ions is nearly converged with the ζ = 4 basis set. The other two processes involve extrapolations of only ca. 2 kJ mol^{-1} so application of different extrapolation strategies would have little impact on ΔE_{final}. The direct calculation of D_0 yields 177.9 kJ mol^{-1}, which is somewhat larger than the 172.8 kJ mol^{-1} derived by Vasiliu et al.[40] using a similar computational method. The critical difference may be the use of a frozen inner core of electrons in the prior work vs the all-electron calculations here. The 5 kJ mol^{-1} increase in D_0 more closely brings theory and experiment, 184.2 ± 4.0 kJ mol^{-1}, into accord. The electron affinity of oxygen is reproduced well at the present level of theory, which yields EA(O_2) about 0.7 kJ mol^{-1} too low when compared to the experimental value of 43.38 ± 0.18 kJ mol^{-1}.[54,55] A similar modest error might exist in KO_2 where a superoxide moiety is present. An alternative assessment of D_0 is thus equal to D_0(ions) − IP(K) + EA(O_2). With experimental values for the latter two items, this also yields D_0 = 177.9 kJ mol^{-1}, confirming the calculation via neutrals. The errors in IP(K) and EA(O_2) have canceled.

CONCLUSIONS

The collinear photofragmentation and atomic absorption spectroscopy (CPFAAS) method has been applied to generate and monitor atomic potassium in the presence of oxygen. Rate constants for the third-order addition process were determined over 748−1323 K, which compare well with prior data obtained at up to 1100 K. The short time scale of the detection method permits direct observation of equilibration in the K + O_2 = KO_2 system for the first time. A third-law analysis yields the K−O_2 bond dissociation enthalpy, which is 9 kJ mol^{-1} greater than the most recent ab initio calculations in the literature. We find that correlating all the electrons in coupled cluster/infinite basis set calculations roughly halves the discrepancy.

ASSOCIATED CONTENT

Supporting Information

Supplementary Table S1 reports the results of the kinetic analyses for K atom loss in the presence of oxygen in a nitrogen bath gas. Supplementary Table S2 summarizes ab initio energies of K, O_2, KO_2, K^+, and O_2^-. This material is available free of charge via the Internet at http://pubs.acs.org.

AUTHOR INFORMATION

Notes

The authors declare no competing financial interest.

ACKNOWLEDGMENTS

We thank Prof. K. A. Peterson (Washington State University) for providing the potassium basis sets. This work has been partly carried out within CLIFF (2014-2017) as part of the activities of Tampere University of Technology. Other research partners are Åbo Akademi University, VTT Technical Research Centre of Finland, Lappeenranta University of Technology, and Aalto University. Support from the National Technology Agency of Finland (Tekes), Andritz Oy, Valmet Technologies Oy, Foster Wheeler Energia Oy, UPM-Kymmene Oyj, Clyde Bergemann GmbH, International Paper Inc., and Top Analytica Oy Ab is gratefully acknowledged. P.M. thanks the Robert A. Welch Foundation (Grant B-1174) for support. P.G. acknowledges financial support by the Danish Strategic Research Council (GREEN).

REFERENCES

(1) Dautriche, H. The Effect of Alkaline Salts with a Fixed Base on the Combustion of Gases and the Combustible Thrust. *Compt. Rend.* **1908**, *146*, 535.

(2) Glarborg, P. Hidden Interactions - Trace Species Governing Combustion and Emissions. *Proc. Combust. Inst.* **2007**, *31*, 77−98.

(3) Mitani, T.; Niioka, T. Extinction Phenomenon of Premixed Flames with Alkali Metal Compounds. *Combust. Flame* **1984**, *55*, 13−21.

DOI: 10.1021/acs.jpca.5b00755
J. Phys. Chem. A 2015, 119, 3329−3336

(4) Kim, H.-T. Inhibition Effectiveness of Dry Chemical in Methane/Air Flames. *Korean J. Chem. Eng.* **1992**, *9*, 1−7.
(5) Klingenberg, G.; Heimerl, J. M. Gun Muzzle Blast and Flash. *Prog. Astronaut. Aeronaut* **1992**, *139*, 241−260.
(6) van Lith, S. C.; Ramirez, V. A.; Jensen, P. A.; Frandsen, F. J.; Glarborg, P. Release to the Gas Phase of Inorganic Elements during Wood Combustion. Part 1: Development and Evaluation of Quantification Methods. *Energy Fuels* **2006**, *20*, 964−978.
(7) van Lith, S. C.; Jensen, P. A.; Frandsen, F. J.; Glarborg, P. Release to the Gas Phase of Inorganic Elements during Wood Combustion. Part 2: Influence of Fuel Composition. *Energy Fuels* **2008**, *22*, 1598−1609.
(8) Knudsen, J. N.; Jensen, P. A.; Dam-Johansen, K. Transformation and Release to the Gas Phase of Cl, K, and S during Combustion of Annual Biomass. *Energy Fuels* **2004**, *18*, 1385−1399.
(9) Glarborg, P.; Marshall, P. Mechanism and Modeling of Gaseous Alkali Sulfate Formation. *Combust. Flame* **2005**, *141*, 22−39.
(10) Christensen, K. A.; Livbjerg, H. A Field Study of Submicron Particles from the Combustion of Straw. *J. Aerosol Sci.* **1996**, *25*, 185−199.
(11) Christensen, K. A.; Stenholm, M.; Livbjerg, H. The Formation of Submicron Aerosol Particles, HCl and SO_2 in Straw-Fired Boilers. *J. Aerosol Sci.* **1998**, *29*, 421−444.
(12) Rosser, W. A., Jr.; Inami, S. H.; Wise, H. The Effect of Metal Salts on Premixed Hydrocarbon-Air Flames. *Combust. Flame* **1963**, *7*, 107−119.
(13) Dewitte, M.; Vrebosch, M.; van Tiggelen, J. A. Inhibition and Extinction of Premixed Flames by Dust Particles. *Combust. Flame* **1964**, *8*, 257.
(14) Hoffmann, W. Influence of Alkali Metal Salts on Laminar Flame Velocity. *Chem. Ing. Tech.* **1971**, *43*, 556−560.
(15) Iya, K. S.; Wollowitz, S.; Kaskan, W. E. The Mechanism of Flame Inhibition by Sodium Salts. *Proc. Combust. Inst.* **1975**, *15*, 329−336.
(16) Jensen, D. E.; Jones, G. A.; Mace, A. C. H. Flame Inhibition by Potassium. *J. Chem. Soc., Faraday Trans 1* **1979**, *75*, 2377−2385.
(17) Jensen, D. E.; Jones, G. A. Kinetics of Flame Inhibition by Sodium. *J. Chem. Soc., Faraday Trans. 1* **1982**, *78*, 2843−2850.
(18) Hynes, A. J.; Steinberg, M.; Schofield, K. The Chemical Kinetics and Thermodynamics of Sodium Species in Oxygen-rich Hydrogen Flames. *J. Chem. Phys.* **1984**, *80*, 2585−2597.
(19) Kim, H. T.; Reuther, J. J. Temperature Dependence of Dry Chemical Premixed Flame Inhibition Effectiveness. *Combust. Flame* **1984**, *57*, 313−317.
(20) Bulewicz, E. M.; Kucnerowicz-Polak, B. J. The Action of Sodium-Bicarbonate and of Silica Powder on Upward Propagating Flame in a Vertical Duct. *Combust. Flame* **1987**, *70*, 127−135.
(21) Slack, M.; Cox, J. W.; Grillo, A.; Ryan, R.; Smith, O. Potassium Kinetics in Heavily Seeded Atmospheric-Pressure Laminar Methane Flames. *Combust. Flame* **1989**, *77*, 311−320.
(22) Steinberg, M.; Schofield, K. The Chemistry of Sodium with Sulfur in Flames. *Prog. Energy Combust. Sci.* **1990**, *16*, 311−317.
(23) Schofield, K.; Steinberg, M. Sodium Sulfur Chemical Behavior in Fuel-Rich and Fuel-Lean Flames. *J. Chem. Phys.* **1992**, *96*, 715−726.
(24) Babushok, V.; Tsang, W.; Linteris, G. T.; Reinelt, D. Chemical Limits to Flame Inhibition. *Combust. Flame* **1998**, *115*, 551.
(25) Williams, B. A.; Fleming, J. W. CF_3Br and Other Suppressants: Differences in Effects on Flame Structure. *Proc. Combust. Inst.* **2002**, *29*, 345−351.
(26) Hindiyarti, L.; Frandsen, F.; Livbjerg, H.; Glarborg, P. Influence of Potassium Chloride on Moist CO Oxidation under Reducing Conditions: Experimental and Kinetic Modeling Study. *Fuel* **2006**, *85*, 978−988.
(27) Kaskan, W. E. The Reaction of Alkali Atoms in Lean Flames. *Proc. Combust. Inst.* **1965**, *10*, 41−46.
(28) McEwan, M. J.; Phillips, L. F. Dissociation Energy of NaO_2*. *Trans. Faraday Soc.* **1966**, *62*, 1717−1720.
(29) Carabetta, R.; Kaskan, W. E. The Oxidation of Sodium, Potassium, and Cesium in Flames. *J. Phys. Chem.* **1968**, *72*, 2483−2489.
(30) Hindiyarti, L.; Frandsen, F.; Livbjerg, H.; Glarborg, P.; Marshall, P. An Exploratory Study of Alkali Sulfate Aerosol Formation during Biomass Combustion. *Fuel* **2008**, *87*, 1591−1600.
(31) Silver, J. A.; Zahniser, M. S.; Stanton, A. C.; Kolb, C. E. Temperature Dependent Termolecular Reaction Rate Constants for Potassium and Sodium Superoxide. *Proc. Combust. Inst.* **1984**, *20*, 605−612.
(32) Husain, D.; Plane, J. M. C. Kinetic Investigation of the Third-order Rate Process between K + O_2 + M by Time-Resolved Atomic Resonance Absorption Spectroscopy. *J. Chem. Soc., Faraday Trans. 2* **1982**, *78*, 1175−1194.
(33) Husain, D.; Lee, Y. H.; Marshall, P. Temperature Dependence of the Absolute Third-Order Rate Constant for the Reaction between K + O_2 + M over the Range 680−1010 K Studied by Time-Resolved Atomic Resonance Absorption Spectroscopy. *Combust. Flame* **1987**, *68*, 143−154.
(34) Plane, J. M. C.; Rajasekhar, B.; Bartolotti, L. Kinetic Study of the Reaction K + O_2 + M (M = N_2, He) from 250 to 1103 K. *J. Phys. Chem.* **1990**, *94*, 4161−4167.
(35) Patrick, R.; Golden, D. M. Termolecular Reactions of Alkali Metal Atoms with O_2 and OH. *Int. J. Chem. Kinet.* **1984**, *16*, 1567−1574.
(36) Jensen, D. E. Alkali Metal Compounds in Oxygen-Rich Flames - A Reinterpretation of Experimental Results. *J. Chem. Soc., Faraday Trans.* **1982**, *178*, 2835−2842.
(37) Figger, H.; Schrepp, W.; Zhu, X. Chemiluminescent Reaction between Alkali Dimers and Oxygen Molecules. *J. Chem. Phys.* **1983**, *79*, 1320.
(38) Partridge, H.; Bauschlicher, C. W., Jr.; Sodupe, M.; Langhoff, S. R. Theoretical Determination of the Alkali-metal Superoxide Bond Energies. *Chem. Phys. Lett.* **1992**, *195*, 200−206.
(39) Lee, E. P. F.; Wright, T. G. The Ionization Energy of KO_2 (X^2A_2) and Dissociation Energies of KO_2 and KO_2^+. *Chem. Phys. Lett.* **2002**, *363*, 139−144.
(40) Vasiliu, M.; Li, S.; Peterson, K. A.; Feller, D.; Gole, J. L.; Dixon, D. A. Structures and Heats of Formation of Simple Alkali Metal Compounds: Hydrides, Chlorides, Fluorides, Hydroxides, and Oxides for Li, Na, and K. *J. Phys. Chem. A* **2010**, *114*, 4272−4281.
(41) Sorvajärvi, T.; Saarela, J.; Toivonen, J. Optical Detection of Potassium Chloride Vapor using Collinear Photofragmentation and Atomic Absorption Spectroscopy. *Opt. Lett.* **2012**, *37*, 4011−4013.
(42) Sorvajärvi, T.; Toivonen, J. Principles and Calibration of Collinear Photofragmentation and Atomic Absorption Spectroscopy. *Appl. Phys. B: Laser Opt.* **2014**, *115*, 533−539.
(43) Sorvajärvi, T.; DeMartini, N.; Rossi, J.; Toivonen, J. In Situ Measurement Technique for Simultaneous Detection of K, KCI, and KOH Vapors Released During Combustion of Solid Biomass Fuel in a Single Particle Reactor. *Appl. Spectrosc.* **2014**, *68*, 179−187.
(44) Sorvajärvi, T.; Manninen, A.; Toivonen, J.; Saarela, J.; Hernberg, R. Resonant Photoacoustic Cell for Pulsed Laser Analysis of Gases at High Temperature. *Rev. Sci. Instrum.* **2009**, *80*, 123103.
(45) Ayhens, Y. V.; Nicovich, J. M.; McKee, M. L.; Wine, P. H. Kinetic and Mechanistic Study of the Reaction of Atomic Chlorine with Methyl Iodide over the Temperature Range 218−694 K. *J. Phys. Chem. A* **1997**, *101*, 9382−9390.
(46) The Computational Chemistry Comparison and Benchmark Database (CCCBDB), Web site http://cccbdb.nist.gov/.
(47) Tremblay, B.; Manceron, L.; Roy, P.; LeQuéré, A.-M.; Roy, D. Vibrational Spectra and Structure of the KO_2 Complex in Solid Argon - A Far-Infrared Study. *Chem. Phys. Lett.* **1994**, *228*, 410−416.
(48) Iron, M. A.; Oren, M.; Martin, J. M. L. Alkali and Alkaline Earth Metal Compounds: Core-Valence Basis Sets and Importance of Subvalence Correlation. *Mol. Phys.* **2003**, *101*, 1345−1361.
(49) Dunning, T. H., Jr. Gaussian-Basis Sets for Use in Correlated Molecular Calculations. 1. The Atoms Boron through Neon and Hydrogen. *J. Chem. Phys.* **1989**, *90*, 1007.

DOI: 10.1021/acs.jpca.5b00755
J. Phys. Chem. A 2015, 119, 3329−3336

(50) Peterson, K. A. Private communication.
(51) Werner, H.-J.; Knowles, P. J.; Lindh, R.; Manby, F. R.; Schutz, M.; Celani, P.; Korona, T.; Mitrushenkov, A.; Rauhut, G.; Adler, T. B.; et al. *Molpro Quantum Chemistry Package* **2009**, http://www.molpro.net/.
(52) Halkier, A.; Helgaker, T.; Jorgensen, P.; Klopper, W.; Koch, H.; Olsen, J.; Wilson, A. K. Basis-Set Convergence in Correlated Calculations on Ne, N_2, and H_2O. *Chem. Phys. Lett.* **1998**, *286*, 243−252.
(53) Ervin, K. M.; Anusiewicz, I.; Skurski, P.; Simons, J.; Lineberger, W. C. The Only Stable State of O_2^- Is the X $^2\Pi_g$ Ground State and It (Still!) Has an Adiabatic Electron Detachment Energy of 0.45 eV. *J. Phys. Chem. A* **2003**, *107*, 8521−8529.
(54) Ruscic, B.; Pinzon, R. E.; Morton, M. L.; von Laszewski, G.; Bittner, S.; Nijsure, S. G.; Amin, K. A.; Minkoff, M.; Wagner, A. F. Introduction to Active Thermochemical Tables: Several "Key" Enthalpies of Formation Revisited. *J. Phys. Chem. A* **2004**, *108*, 9979−9997.
(55) Ruscic, B.; Pinzon, R. E.; von Laszewski, G.; Kodeboyina, D.; Burcat, A.; Leahy, D.; Montoya, D.; Wagner, A. F. Active Thermochemical Tables: Thermochemistry for the 21st Century. *J. Phys. Conf. Ser.* **2005**, *16*, 561−570.
(56) NIST Chemistry WebBook, webbook.nist.gov/chemistry/.

DOI: 10.1021/acs.jpca.5b00755
J. Phys. Chem. A 2015, 119, 3329−3336

Paper II

Microwave Assisted Laser-Induced Breakdown Spectroscopy at Ambient Conditions

by
Jan Viljanen, Zhiwei Sun, and Zeyad T. Alwahabi
Spectrochimica Acta Part B: Atomic Spectroscopy 118, 29-36 (2016)

Spectrochimica Acta Part B 118 (2016) 29–36

Contents lists available at ScienceDirect

Spectrochimica Acta Part B

journal homepage: www.elsevier.com/locate/sab

Microwave assisted laser-induced breakdown spectroscopy at ambient conditions

Jan Viljanen [d], Zhiwei Sun [b,c], Zeyad T. Alwahabi [a,b,*]

[a] School of Chemical Engineering, The University of Adelaide, S.A. 5005, Australia
[b] Centre for Energy Technology, The University of Adelaide, S.A. 5005, Australia
[c] School of Mechanical Engineering, The University of Adelaide, S.A. 5005, Australia
[d] Optics Laboratory, Tampere University of Technology, FIN-33101 Tampere, Finland

ARTICLE INFO

Article history:
Received 7 July 2015
Accepted 2 February 2016
Available online 6 February 2016

Keywords:
Laser-induced breakdown spectroscopy
Microwave signal enhancement
Copper Detection

ABSTRACT

Signal enhancements in laser-induced breakdown spectroscopy (LIBS) using external microwave power are demonstrated in ambient air. Pulsed microwave at 2.45 GHz and of 1 millisecond duration was delivered via a simple near field applicator (NFA), with which an external electric field is generated and coupled into laser induced plasma. The external microwave power can significantly increase the signal lifetime from a few microseconds to hundreds of microseconds, resulting in a great enhancement on LIBS signals with the use of a long integration time. The dependence of signal enhancement on laser energy and microwave power is experimentally assessed. With the assistance of microwave source, a significant enhancement of ~100 was achieved at relatively low laser energy that is only slightly above the ablation threshold. A limit of detection (LOD) of 8.1 ppm was estimated for copper detection in Cu/Al_2O_3 solid samples. This LOD corresponds to a 93-fold improvement compared with conventional single-pulse LIBS. Additionally, in the microwave assisted LIBS, the self-reversal effect was greatly reduced, which is beneficial in measuring elements of high concentration. Temporal measurements have been performed and the results revealed the evolution of the emission process in microwave-enhanced LIBS. The optimal position of the NFA related to the ablation point has also been investigated.

1. Introduction

With the attractive characteristics of no or minimal sample preparation, stand-alone capability, information richness and ability to measure gas, liquid and solid phase, laser-induced breakdown spectroscopy (LIBS) has become a popular spectroscopic technique. LIBS is also a simple technique in which radiation emitted by a focused laser pulse induces plasma which is then detected and spectrally analysed. In principle, the elemental composition of the sample can be resolved from the LIBS achieved with a single laser pulse and a spectral detector. LIBS has been applied on multiple disciplines such as mining, pharmaceuticals and space exploration [1]. Despite these great features, LIBS has few drawbacks, for example relatively low sensitivity and pulse-to-pulse repeatability, which make LIBS fall behind other techniques for quantitative or qualitative analysis of elements.

To increase the sensitivity of LIBS, several methods have been proposed [1]. Among these methods, double-pulse LIBS, where two laser pulses are used to create the plasma, is the most popular technique and has attracted much interest both in research and in applications; see [1–3] and references therein. Besides, LIBS signal can also be enhanced through space confinements, e.g. [4–9], with the use of resonant laser sources, e.g. [10–13] and by coupling external energy source. The basic idea of the use of an external source may be understood as that the plasma created by the first laser is sustained and/or enhanced by the absorbed power of the second source. This additional power can be provided by a long pulse laser [14], a spark discharge [15–17], a microwave source [17–21], and even a stable flame [22] and a simple micro torch [23]. The combination of two assisted techniques has also been demonstrated, e.g. [24,25].

The enhancement of LIBS signal by the use of microwave (MW) radiation has shown promising results. The external MW power is coupled in laser induced plasma to sustain emissions as well as increase the plasma volume. A laser-assisted microwave plasma spectroscopy (LAMPS) system was reported [18] which applies electric field to the laser induced plasma by enclosed MW cavity. The presence of the MW radiation extends the plasma lifetime and increases the plasma size, resulting in a very promising improvement in sensitivity by a factor of 10 to 1000 times depending on the sample type. The LAMPS technique was also reported by Efthimion [26], where an enhancement of 200 times was achieved. Liu et al. applied a MW cavity system to examine ceramics and soil sample, demonstrating an enhancement factor of up to 33 for sodium detection [19,20]. Another way to deliver the microwave power into the laser generated plasma is the use of an antenna. In gaseous samples, Ikeda et al. studied the characteristics of laser- and spark-induced plasmas with an external antenna-coupled MW

* Corresponding author.
E-mail address: zeyad.alwahabi@adelaide.edu.au (Z.T. Alwahabi).

http://dx.doi.org/10.1016/j.sab.2016.02.002
0584-8547/

power, where a 15 times enhancement for Pb spectra of LIBS was reported [17]. Antenna-coupled MW enhanced LIBS on solid samples was recently introduced by Khumaeni et al. at lower pressure in enclosed cavity environments [27]. A loop antenna was used to deliver MW radiation close to laser ignited plasma and a 32 times enhancement of Gd lines was observed. The authors also found that enhancement was weak from near atmospheric pressure to 6.67 kPa. With the use of a similar loop antenna, Tampo et al. had achieved a 50-fold enhancement of Gd lines at a low pressure of 0.6 kPa [21]. These studies mentioned above have demonstrated that MW assisted LIBS (MW-LIBS) is an attractive technique for trace element determination with high sensitivity.

However, MW-LIBS working at atmospheric pressure and ambient air conditions without employing an enclosed cavity has not yet been demonstrated. Indeed, with the aim of in situ sample analysis in ambient air, a more flexible MW-LIBS set-up has to be developed to avoid the complex process of sample loadings and be applied as conventional LIBS. This consequently enhances the time- and spatial-resolved abilities of MW-LIBS, which is greatly beneficial in practical applications. Therefore, in the present work, a new MW-LIBS working at atmospheric pressure is demonstrated, in which the external MW is coupled into the plasma via a novel and simple near-field applicator (NFA). This paper starts with the demonstration of the technique through copper detections in solid samples of Cu/Al_2O_3. Then temporal evolution measurements were performed to reveal the evolution of emission spectra and to understand the process of MW-LIBS. After that the influences of experimental parameters (including laser energy, microwave power and the position of the NFA) on the MW-LIBS signal intensity have been studied.

2. Experimental set-up

2.1. LIBS setup

The experimental arrangement is schematically illustrated in Fig. 1. The output from the second harmonic of a Q-switched Nd:YAG laser (Surelite II) was used to provide the light source. The pulse width was ~6 ns with a wavelength of 532 nm and a 10 Hz repetition. A half-wave plate (HWP) combined with a Glan-laser polarizer (P) was used to control the ablating pulse energy. The laser energy used in the measurements was measured with a power meter. The laser beam was led to the sample surface by the use of a dichroic mirror (DM) with a high reflectivity in the 500–550 nm spectral region and then was focused using a fused silica lens (L1, with f = 100 mm). The elemental emission lines in this study are around 325 nm, therefore the use of the dichroic mirror enabled the use of the focusing lens (L1) also for signal collection. This design made it easier to load sample and align optics. The spot size obtained at the focal spot was estimated to be 100 μm, while the propagation of laser beam was normal to the sample surface.

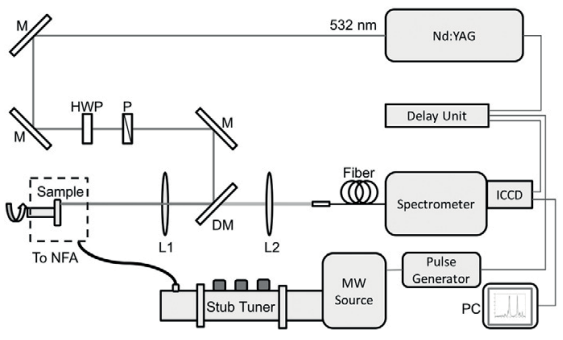

Fig. 1. Schematic presentation of the experimental setup.

LIBS signals were collected with the lens L1 and then focused into a bifurcated fibre bundle (Thorlabs, BFY400HS02) using another lens (L2), with f = 50 mm. The fibre bundle has a core size of 400 μm and a transmission range of 250–1200 nm. The spectrometer (Andor Shamrock 500i) with gratings of 2400 lines/mm installed has a spectral resolving power of 10,000, i.e., the spectral resolution is 0.031 nm in the spectral region of 320–332 nm. The dispersed emission signals were recorded by an intensified CCD camera (Andor, iStar), which was synchronized with the laser and the microwave generator with an external signal delayed box (Princeton Technologies). Different gate widths and delay times were used for the camera during measurements, which will be clarified with results.

2.2. MW source and near-field applicator

The pulsed microwave radiation, at 2.45 GHz, was generated by a water-cooled 3000 Watt (W) Sairem microwave system shown in Fig. 1. The system consists of a generator coupled to an isolator equipped with a crystal detector to monitor the microwave reflected power. The microwave radiation is directed, via a WR340 waveguide, to a 3-stub impedance tuner and then to a waveguide-to-coaxial adaptor (WR340RN), after having passed a quartz window. The waveguide-to-coaxial adaptor was connected to a 1 m flexible coaxial cable (50 Ω NN cable) with 0.14 dB @ 2.45 GHz. The end of the coaxial cable was then connected to a semi rigid cable (RG402/U). One end of the semi rigid cable was stripped off to expose ~25 mm of the inner silver plated copper steel core. The end of the core was sharpened to a point with an angle of ~45° to form a NFA, as shown in Fig. 2. The NFA is designed to generate a strong electrical field near the tip without emitting microwave radiation. The strength of microwave radiation near the tip was measured by a microwave survey meter (Sairem IFP 05 C). The reading at 30 mm away from the tip was 2.4 mW/cm^2, when the microwave source was operating at 1200 W. It is worth noting that the waveguide-to-coaxial adaptor is designed to operate with microwave power up to 300 W in CW mode. However, it was possible to couple higher power, e.g. 1500 W, when operated in a pulsed mode.

The NFA was located about 1 mm above the sample surface and 0.5 mm horizontally away from the ablation spot. This NFA position was chosen by achieving the maximum coupling efficiency of microwave power to plasma. The coupling efficiency was approximately 70%, as estimated from the reflected MW power. The samples were placed on a rotating stage to ensure that each laser shot ablated on a fresh surface. It must be noted that since the NFA is made of copper, which was also used as the measuring element in the present work,

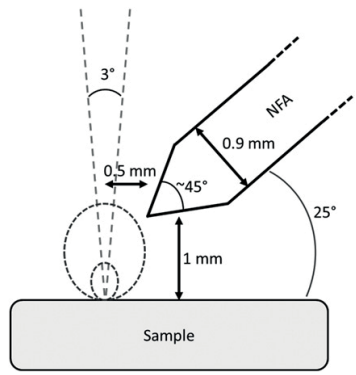

Fig. 2. Schematic presentation of the shape of the near-field applicator and its location related to sample in measurements. Small and large dashed circles represent the time-averaged size of plasma formed in conventional LIBS and MW-LIBS, respectively, which were measured by a digital camera.

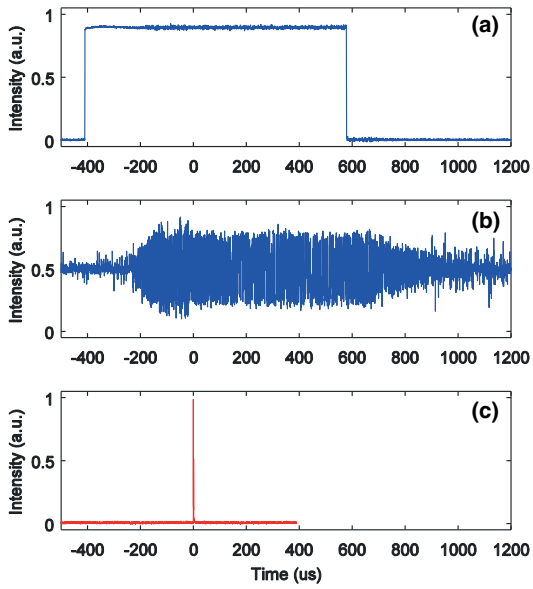

Fig. 3. The timing relation of (a) microwave driving signal, (b) microwave output and (c) laser pulse working for MW-LIBS.

interference from the NFA to LIBS signals had been carefully checked. No copper emission signal at the wavelength of 324.75 nm had been found in a solid copper-free sample neither in MW-LIBS nor in conventional LIBS.

The power and duration of the microwave pulse were controlled with an analogue signal from a pulse generator (Aim-TTi). Fig. 3 presents the timing relations between the microwave controlling signal, the microwave output and the laser pulse. After the microwave output reached the maximum value, the laser pulse was triggered, i.e., near field microwave was formed prior to the ablation process. After the laser pulse, the microwave output lasted ~650 μs and then decayed to zero slowly. Note that the typical persistence time of conventional LIBS signals is around 10 μs, which is much less than the duration of the microwave power (~650 μs).

2.3. Samples

An Australian 20 cent coin, which has a content of 75% copper and 25% nickel, was used as the sample to assess the nature of microwave enhancement on LIBS signals at atmospheric pressure and ambient air. Besides, to assess the linearity and the detection limit (for Cu I) of the proposed technique, several calibration samples with different copper concentrations were fabricated by wet impregnation from Al_2O_3 and $Cu(NO_2)_3{\cdot}3H_2O$. Samples with 0.2–1.2% (by weight) of copper were fabricated and further diluted with Al_2O_3 to the concentrations used for calibrations. Calibration sample powder was then set to a sample mold and was bounded with commercial sprays.

Table 1
Summary of Cu I spectral lines in the present work.

Wavelength (nm)	Transition probability (s^{-1})	Lower level energy (cm^{-1})	Upper level energy (cm^{-1})	Lower level J_i	Upper level J_k
324.75	1.395×10^8	0	30,783.697	1/2	3/2
327.40	1.376×10^8	0	30,535.324	1/2	1/2
327.98		13,245.443	43,726.24	3/2	5/2
330.79		40,909.16	71,130.68	9/2	11/2

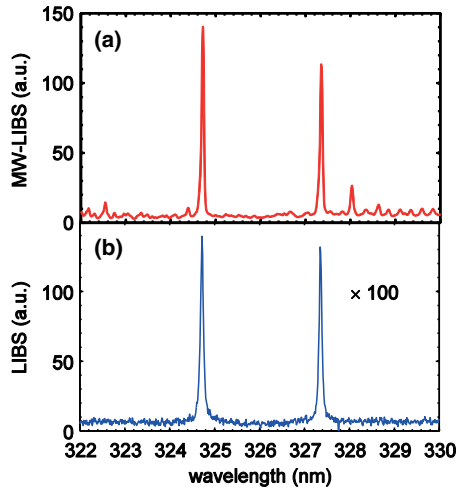

Fig. 4. Spectra of solid sample of containing 3000 mg·kg^{-1} of Cu (i.e., 0.3% by weight) in (a) MW-LIBS and (b) conventional LIBS. The laser energy was 0.8 ± 0.1 mJ/pulse and the microwave power was 1.2 kW. The delayed time and gate width were 500 ns and 800 μs in recording (a), respectively, while they were 300 ns and 10 μs in recording (b). The spectra were accumulated over 300 laser shots. Note that the spectrum recorded in LIBS has been multiplied with a factor of 100. The two spectra are shown in the same intensity scale.

3. Results and discussions

3.1. Spectral information

Spectral emissions from the range of 320–332 nm were recorded in LIBS with and without microwave. Table 1 summarizes the four spectral lines used in the present work [28,29]. In the following sections, the discussions will be focused on the two strong lines at 324.75 nm and

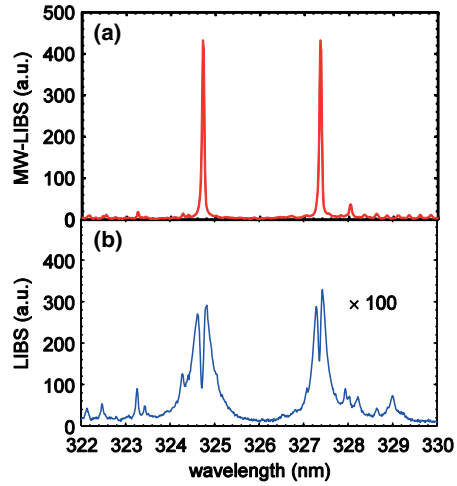

Fig. 5. Spectra of an Australian coin with 75% copper and 25% nickel recoded in (a) MW-LIBS and in (b) conventional LIBS. The laser energy was 0.8 ± 0.1 mJ/pulse and the microwave power was 1.2 kW. The delayed time and gate width of the camera were set as 500 ns and 800 μs in recording (a), respectively, while they were 300 ns and 10 μs in recording (b). The spectra were accumulated over 300 laser shots. Note that the spectrum recorded with LIBS has been multiplied with a factor of 100. The two spectra are shown in the same intensity scale.

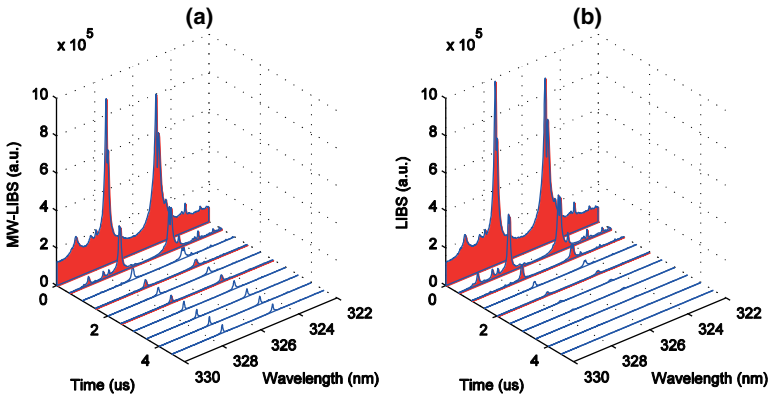

Fig. 6. Temporal evolutions of spectra within 5 μs in the range of 322–330 nm (a) in MW-LIBS and (b) in conventional LIBS. The sample was an Australian coin with 75% copper and 25% nickel. The laser energy was 0.8 ± 0.1 mJ/pulse and the microwave power was 1.2 kW. The gate width of the camera was kept as 500 ns and was delayed with steps of 500 ns. Each spectrum was accumulated over 300 laser shots.

327.40 nm; while the two relatively weaker lines at 327.98 nm and 330.79 nm were used to estimate the change of the electron temperature during plasma evolutions (see Fig. 9).

3.2. Examples of LIBS signal

Fig. 4 presents two LIBS spectra recorded in MW-LIBS and conventional LIBS, respectively. The concentration of Cu in the sample is 0.3% by weight and the laser energy was 0.8 mJ/pulse, which is slightly above the ablation threshold. A significant enhancement of ~100 can be clearly seen for both of the two Cu I lines at 324.75 nm and 327.40 nm. Weak background can be seen in both of spectra, in which the system background had already been subtracted. In addition, some few weak spectral structures appeared at around 322.5 nm and 328–330 nm in the MW-LIBS spectra. These emission lines, given rise by the effect of microwave enhancement, are attributed to other species and can be significantly reduced with the use of a longer delayed time (>500 ns), while a negligible decrease is caused to the Cu I line intensity. This will be shown in the following section of temporal evolution investigations. No clear difference was found in the line width of the spectral lines, which may be due to the limited spectral resolution of the present set-up. Also note that the third strongest spectral line in Fig. 4a is at 328.05 nm, which cannot be identified as the Cu I line at 327.98 nm. However, the source of this line is unclear to the authors.

The two Cu I lines shown in Fig. 4 correspond to the transitions from the upper levels to the ground state and, therefore, are potentially influenced by the self-absorption effect. This is confirmed by the intensity ratios of the two lines in Fig. 4, which are much less than the theoretical value of 2 (estimated via the factor of $2J_k + 1$, where J_k is the total angular momentum quantum number as shown in Table 1). Fig. 4 also reveals that the application of MW slightly reduces the self-absorption effect, since the ratio in the MW-LIBS spectra (Fig. 4a) is slightly greater. This may indicate the homogeneous temperature emitting zone expanded with the assistance of microwave.

Besides signal enhancement and self-absorption reduction as shown in Fig. 4, MW-LIBS is also beneficial in reducing the self-reversal effect which causes a spectral dip to generally appear around the central part of the emission line bounded by the ground state, e.g. [30, 31]. Fig. 5 presents the spectra of an Australian coin made of 75% copper and 25% nickel by weight. In Fig. 5a, with MW the spectrum has sharp line profiles with negligible background, while Fig. 5b shows significant self-reversed profiles in the two spectral lines. No self-reversal profile has been found in the MW-LIBS in Fig. 5a (as well as MW-LIBS recorded with other laser energy), however, the two spectral lines are still significantly influenced by the self-absorption, due to the high concentration of Cu in the sample. The reduction of self-reversal effect in MW-LIBS is beneficial in quantitative measurements, especially when the concentration of targeted species is high, as Cu in the coin. While more work is needed to assess the physical mechanisms for the reduced self-reversal effect, a potential reason is that with the assistance of microwave the plasma expanded significantly and the emitting zone with homogeneous temperature became much larger than in conventional LIBS. More detailed discussion will be performed in the following section of temporal evolution investigations.

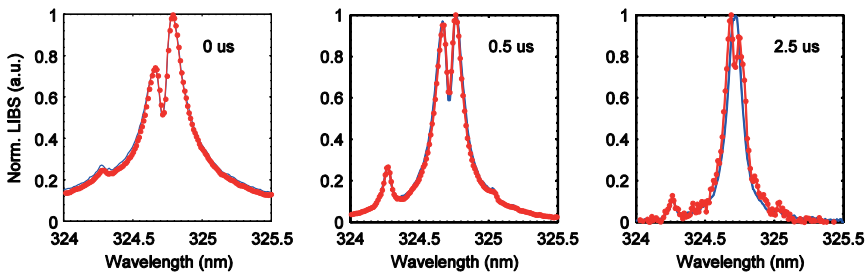

Fig. 7. Line profiles of Cu I emission at 324.75 nm at three delay times in MW-LIBS (blue lines) and in conventional LIBS (red lines). The experimental conditions are as the same as stated in Fig. 6.

3.3. Temporal evolution measurements

Fig. 6 presents the temporal evolutions of the spectra within 4.5 μs after the laser pulse in MW-LIBS and conventional LIBS. The sample is an Australian coin with 75% Cu by weight. The gate width of camera was kept at 500 ns and was delayed with a gate step of 500 ns from the prompt detection. The most significant difference between Fig. 6a and b is that the Cu I emissions could be sustained for 4.5 μs in MW-LIBS, while in conventional LIBS they rapidly decayed and became too weak to be detected after 3 μs. Contrarily, the spectra were similar in MW-LIBS and conventional LIBS within 1.5 μs. This may be because the microwave cannot be efficiently absorbed by the prompt plasma due to the fact that the initial electron density is higher than 7×10^{10} cm^{-3} [20]. In Fig. 6a, Cu I emissions in MW-LIBS decreased slowly after 2 μs, which will be discussed in a following section, where temporal evolution measurements were performed within a whole cycle of 800 μs.

Fig. 7 presents the normalized spectral profiles of Cu I line at 324.75 nm at three delayed times, i.e., 0, 0.5 and 2.5 μs. In both MW-LIBS and conventional LIBS, the line width of emission decreased quickly with time, indicating a rapid decrease of the electron density N_e in the plasmas. The self-reversal effect was significant at 0 and 0.5 μs with almost the same profiles in both measurement sets. This further indicates that interaction between initial plasma and microwave is weak, or even negligible, within 0.5 μs. Spectral profiles were clearly different at 2.5 μs. While the spectrum in the conventional LIBS was still significantly self-reversed, that in MW-LIBS was weaker and no spectral dip was found. This may reveal that with the assistance of MW the laser-induced plasma became more thermally homogeneous than that in conventional LIBS.

To understand the evolution of the Cu I emission with the assistance of MW, temporal evolution measurement was then extended to 20 μs. Fig. 8 presents the measured temporal evolutions under the same experimental conditions as stated in Fig. 6. The emission intensities of the two Cu I lines were nearly constant from 4 μs to 20 μs, indicating that with MW the lifetime of plasma became much longer that in LIBS without MW (Fig. 6b). Therefore, the MW-LIBS signal integrated over hundreds of microseconds was much stronger than that obtained in conventional LIBS, as shown in Fig. 4, even though the instantaneous signal was not as strong as in the initial plasma. This may be the main mechanism of signal enhancement in MW-LIBS.

Fig. 9a presents the corresponding line profiles recorded in the temporal evolution measurement shown in Fig. 8. The same line width in the spectra recorded at 8 μs and 18 μs is owing to the limited spectral resolution of the detection instrument. Nevertheless, the line width at 8 μs was much narrower than that at 2 μs, when the conventional LIBS signal had already decayed significantly (see Fig. 6b). This reveals that the electron number density kept decreasing in the MW assisted plasma. Meanwhile, the temporal evolution of electron temperature was also qualitatively characterized with assumption of Local Thermodynamic Equilibrium through the intensity ratio of Cu I emissions at 327.98 nm and 330.79 nm emitting from the upper energy levels of 43,726.24 cm^{-1} and 71,130.68 cm^{-1}, respectively. With the choice of the emission lines not to be transitioned to ground state, the effect of self-absorption is made negligible. Fig. 9b presents the line intensity ratio as a function of time, as well as a fitting curve to trace the scattering points. A decrease trend can be found in Fig. 9b, albeit the ratios fluctuate due to the weak intensities of the two lines. Because the intensity ratio between the lines emitting from 43,726.24 cm^{-1} and 71,130.68 cm^{-1} became weak with time, it can be concluded that the electron temperature also decreases with time in MW-LIBS. It should be noted that the effect of reheating-up plasma in MW-LIBS had been reported in [21,27] and was also observed by us in the detection of indium in an aqueous solution using the same Microwave system setup [32]. The different behavior of the electron temperature in MW-LIBS may be due to the different experimental parameters applied in experiments, e.g. laser fluence and microwave power.

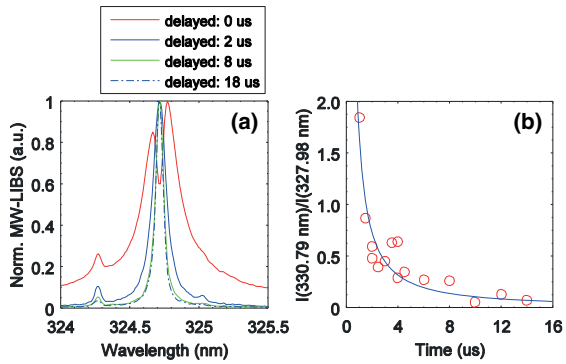

Fig. 9. (a) line profiles of Cu I emission at 324.75 nm at four delayed times, i.e., prompt, 2 μs, 8 μs and 18 μs in MW-LIBS. The integrated time was 2 μs. (b) the intensity ratio of Cu I two lines emitted from two different upper energy levels as a function of time.

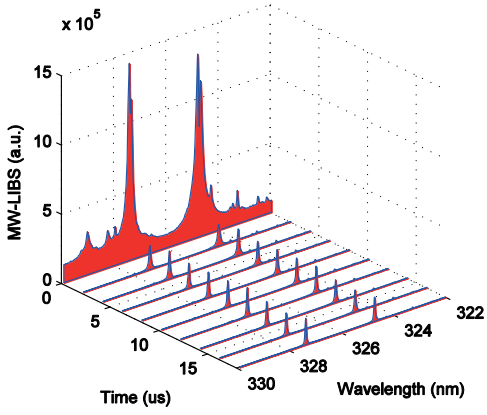

Fig. 8. Temporal evolutions of MW-LIBS spectra within 20 μs. The gate width was kept as 2 μs and was delayed with steps of 2 μs. Each spectrum was accumulated over 300 laser shots.

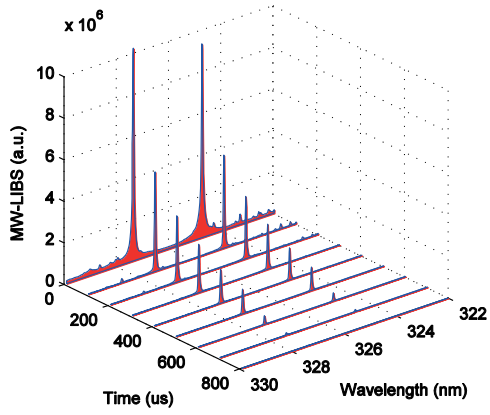

Fig. 10. Temporal evolution of MW-LIBS spectra within 800 μs. The gate width was kept to be 100 μs and was delayed with steps of 100 μs. Each spectrum was accumulated over 300 laser shots.

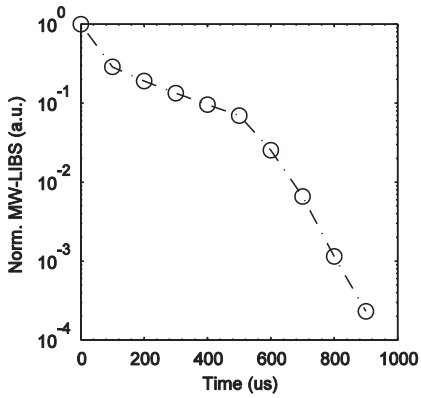

Fig. 11. Intensity of Cu I line at 324.75 nm in MW-LIBS as a function of time.

Measurement was then extended to 800 μs to characterize the evolution of the MW-LIBS signal within a whole cycle. The gate width was 100 μs and was delayed with steps of 100 μs. The results in Fig. 10 show that Cu I emissions can be sustained for 600 μs, which is much longer than that of 2–3 μs in conventional LIBS (see Fig. 6b). The signals also decayed with time, which is clearly seen in such a long delay time. Fig. 11 presents the intensities of the Cu I line at 324.75 as a function of the delay time, where a logarithm scale is employed for the intensity. Three main regimes were identified within a cycle. Signal decays rapidly from 0 to 100 μs and then decays slowly from 100 to 600 μs before decreasing abruptly after 600 μs in the absence of the MW. This trend is consistent with the variation of the microwave power supply as shown in Fig. 3, indicating that the MW-LIBS signal is dependent on the microwave power.

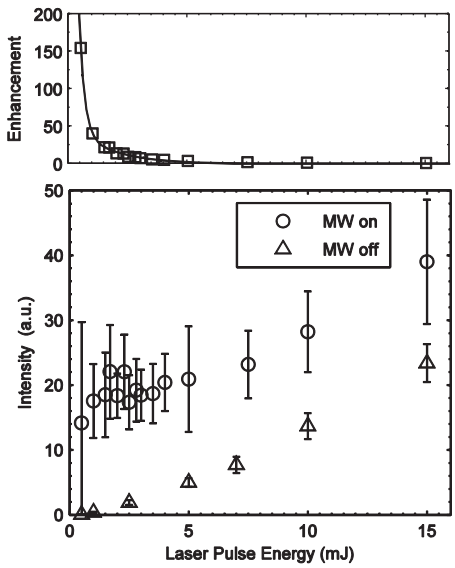

Fig. 12. Signal intensity as a function of laser energy in conventional LIBS and MW-LIBS, as well as the corresponding signal enhancements. The microwave power was 1.2 kW. The measurements were performed in the calibration sample with 0.3% copper by weight. A common gate width of 800 μs was used in conventional and MW-LIBS, while the gate was delayed 0.5 μs and 1 μs, respectively. All intensities were averaged over 100 single-shot measurements and the error bars were the standard deviations.

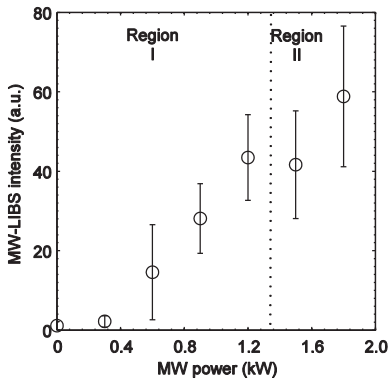

Fig. 13. Signal intensity as a function of the supplied microwave power in MW-LIBS. The laser energy was 2.5 mJ and the sample was slightly away from the focus of the laser beam, ensuring that the power fluence was consistent in this work. Other experimental parameters are as the same as stated in Fig. 12.

3.4. Dependence of MW-LIBS on experimental parameters

In this section, the dependence of the MW-LIBS signal intensity on laser energy, microwave power and the NFA position is investigated, with aims to optimize the MW-LIBS signal and to find its suitable applications.

Fig. 12 presents the signal intensities for the 324.75 nm line as a function of laser energy in LIBS with and without MW power, respectively, as well as the corresponding signal enhancements. While the conventional LIBS signals increased near linearly with the laser energy, those of MW-LIBS showed a nonlinear dependence. At low laser energy of <5 mJ, the signals in MW-LIBS were much stronger than those in LIBS, but only slightly increased with the laser energy. When the laser energy was further increased, i.e., >5 mJ, signals in MW-LIBS showed a similar linear trend as those in conventional LIBS. Clearly, it is attractive to use MW-LIBS when low laser energy has to be applied. As shown in Fig. 12, the enhancement of signal level can be more than 100 times, which is consistent with the results shown in Section 3.2. Also found in Fig. 12 are the larger error bars appearing MW-LIBS compared to conventional LIBS. This is due to the unstable coupling efficiency of MW with the plasma. The large error bar in MW-LIBS at the lowest laser energy (~0.5 mJ) is because the initial plasma was also unstable. Nevertheless, Fig. 12 shows that the signal enhancement decreases exponentially with the increase of laser energy.

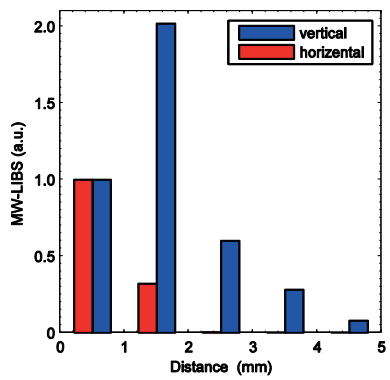

Fig. 14. The dependences of MW-LIBS signal intensity on the vertical distance of the NFA above the place and the horizontal distance to the laser propagation. The signals have been normalized to that at the closest location (0.5 mm). The laser energy was 2.5 mJ.

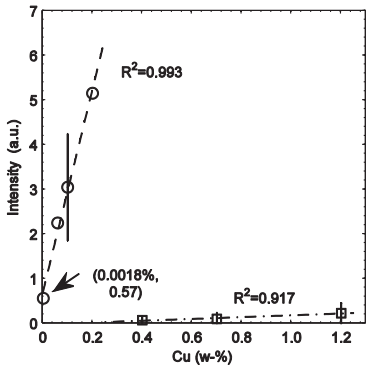

Fig. 15. Calibration curves of the Cu I 324.75 nm line in MW-LIBS (circles) and conventional LIBS (squares). The laser energy was 2.5 mJ and the microwave power was 1.2 kW. The gate width was 800 μs and 10 μs in MW-LIBS and conventional LIBS, respectively, while with the same delay time of 1 μs. The results were averaged over 300 single-shot measurements. Typical standard deviations are shown.

Fig. 13 presents the dependency of the Cu intensity on microwave power supplied. The coupling efficiency of MW to plasma was monitored by the reflected MW power. It was noted that in the region *I* the MW coupling efficiency maintained constantly around 70% level, however, when the MW source power was increased over 1.2 kW (the region *II*) the coupling efficiency to plasma started to vary and decreased. In Fig. 13, it can be clearly seen that the MW-LIBS signal increases with MW power supplied. This may be explained by the decay rate of the plasma in MW-LIBS being dependent on the microwave power, as shown in Fig. 11. However, for a more clear interpretation, further investigations are needed to understand the dependences of electron temperature and electron number density on MW power.

Fig. 14 presents the variations of signal intensity in MW-LIBS with the distance between the NFA and the ablation point. When the NFA position was changed vertically, the horizontal distance was kept as 1 mm. While when it was moved in the horizontal direction, its height was kept as 1 mm above the sample surface. It can be seen that the MW-LIBS signal is more sensitive to the horizontal distance than that in the vertical direction. When the NFA was at 3.5 mm above the sample surface, LIBS signal was still enhanced; even though the magnitude was weaker than that at the optimum distance of ~1 mm above the sample surface. When the NFA was moved horizontally away from the ablation point, the MW-LIBS decreased rapidly within 2 mm. This may be because the shape of the initial plasma shape was biased to the laser beam propagation direction which was vertical. When the NFA was vertically 0.5 mm close to the sample surface, it intruded on the initial plasma; therefore the signal was weaker than that when the NFA was at 1.5 mm, as shown in Fig. 14.

To assess the analytical performance of conventional LIBS and MW-LIBS using the aforementioned setup, calibration curves for the Cu I line at 324.75 nm were measured using the calibration samples of Cu/Al_2O_3. This assessment was also needed to verify the linear relation between signal and elemental concentration in MW-LIBS. Fig. 15 presents the results measured in conventional LIBS and MW-LIBS. A good linear response of the signal to the Cu concentration can be found in MW-LIBS; even though the standard deviation of intensity is relatively large, which is mainly due to the microwave coupling process. Note that the calibration curve measured with MW-LIBS is biased not to pass the concentration axis due inaccuracy in the low concentration copper samples. The limits of detection (LODs) were estimated by applying equation of $LOD = k \cdot s_i / b$, where k is the desired confidence level, s_i is the standard deviation of blank measurement and b is the slope of the calibration curve [1]. The LODs were found to be 754 ppm and 8.1 ppm in conventional LIBS and MW-LIBS, respectively, i.e., a 93-fold improvement in the LOD using MW-LIBS. Reduced noise s_i, i.e. improved signal to noise ratio, leads to higher improvement factor of LOD than that expected from signal enhancement alone, which for 2.5 mJ laser energy was about 10-fold as shown in Fig. 12.

Table 2 presents the comparisons of the current MW-LIBS with other reported methods in which MW was also used as the additional power but coupled with LIBS in different ways. Even though that direct comparison is difficult owing to different experimental setups and parameters (e.g., laser power and duration, focusing, sample matrix) being utilized, MW-LIBS employing an NFA for power coupling has demonstrated its advantages both in signal enhancement and high LOD. A similar enhancement of ~100 fold in LOD was also achieved for other species detection in our experiment. Additionally, the method using an NFA can be applied to an open environment, which is greatly beneficial in in-situ applications.

4. Conclusions

Microwave assisted LIBS has been demonstrated for the first time at ambient conditions employing a novel near field applicator and working without the requirement of an enclosed cavity. The detailed temporal evolution measurements showed that the persistence of the emission was extended to hundreds of microseconds; therefore, signal enhancements can be achieved with the use of a long integration time. An improvement of about 100 folds in the limit of detection has been achieved for the Cu detection using the 324.75 nm line. The magnitude of signal enhancement is sensitively dependent on the laser energy, which shows that the technique has great potential applications in LIBS with weak laser energy. In addition, a high microwave power can increase the MW-LIBS signals. The technique is also attractive in significantly reducing the self-reversal effect, which is beneficial when LIBS is applied for high concentration element detections.

Table 2
Comparison with the reported MW-LIBS methods.

Sample	Laser energy (mJ)	Pressure (atm)	Method of MW interaction	Enhancement factor	LOD (ppm by weight)	Ref.
Cu I in soil	10	1	Enclosed cavity	23	30	19
Ag I in soil	10	1	Enclosed cavity		23.3	19
Na I in ceramic	1.5–61	1	Enclosed cavity	33		20
Ca I in ceramic	1.5–61	1	Enclosed cavity	22		20
Mg I in ceramic	1.5–61	1	Enclosed cavity	16		20
Al I in ceramic	1.5–61	1	Enclosed cavity	11		20
Ba II in ceramic	1.5–61	1	Enclosed cavity	5		20
K I in ceramic	1.5–61	1	Enclosed cavity	5		20
Gd II in Gd_2O_3	5	0.006	Enclosed/antenna	50		21
Eu II in Gd_2O_3	5	0.006	Enclosed/antenna	12.5	40	21
Gd II in Gd_2O_3	5	0.0027	Enclosed/antenna	32	2	27
Cu I in Al_2O_3	2.5	1	Open/near field applicator	93	8.1	This work

Acknowledgments

The financial support from the Institute for Mineral and Energy Resource (IMER) and the Faculty of Engineering, Computer & Mathematical Science (ECMS) of the University of Adelaide (SRI 2014 University of Adelaide Grant 13114264) is gratefully acknowledged. The first author acknowledges the support by ARVI research program coordinated by CLEEN Ltd., funded by the Finnish Funding Agency for Technology and Innovation, Tekes.

References

[1] D.W. Hahn, N. Omenetto, Laser-induced breakdown spectroscopy (LIBS), part II: review of instrumental and methodological approaches to material analysis and applications to different fields, Appl. Spectrosc. 66 (2012) 347–419.
[2] V.I. Babushok, F.C. DeLucia Jr., J.L. Gottfried, C.A. Munson, A.W. Miziolek, Double pulse laser ablation and plasma: laser induced breakdown spectroscopy signal enhancement, Spectrochim. Acta Part B 61 (2006) 999–1014.
[3] F. Colao, V. Lazic, R. Fantoni, S. Pershin, A comparison of single and double pulse laser-induced breakdown spectroscopy of aluminum samples, Spectrochim. Acta Part B 57 (2002) 1167–1179.
[4] Z. Wang, Z. Hou, S.-l. Lui, D. Jiang, J. Liu, Z. Li, Utilization of moderate cylindrical confinement for precision improvement of laser-induced breakdown spectroscopy signal, Opt. Express 20 (2012) A1011–A1018.
[5] P. Yeates, E.T. Kennedy, Spectroscopic, imaging, and probe diagnostics of laser plasma plumes expanding between confining surfaces, J. Appl. Phys. 108 (2010) 093306.
[6] A.M. Popov, F. Colao, R. Fantoni, Spatial confinement of laser-induced plasma to enhance LIBS sensitivity for trace elements determination in soils, J. Anal. At. Spectrom. 25 (2010) 837–848.
[7] A.M. Popov, F. Colao, R. Fantoni, Enhancement of LIBS signal by spatially confining the laser-induced plasma, J. Anal. At. Spectrom. 24 (2009) 602–604.
[8] R. Hedwig, T. Jie Lie, M. On Tjia, K. Kagawa, H. Kurniawan, Confinement effect in enhancing shock wave plasma generation at low pressure by TEA CO_2 laser bombardment on quartz sample, Spectrochim. Acta Part B 58 (2003) 531–542.
[9] X.K. Shen, J. Sun, H. Ling, Y.F. Lu, Spatial confinement effects in laser-induced breakdown spectroscopy, Appl. Phys. Lett. 91 (2007) 081501.
[10] D. Cleveland, R.G. Michel, Quantitative analysis by resonant laser ablation with optical emission detection: resonant laser-induced breakdown spectroscopy, Microchem. J. 95 (2010) 120–123.
[11] W.L. Yip, N.H. Cheung, Analysis of aluminum alloys by resonance-enhanced laser-induced breakdown spectroscopy: how the beam profile of the ablation laser and the energy of the dye laser affect analytical performance, Spectrochim. Acta Part B 64 (2009) 315–322.
[12] S.L. Lui, N.H. Cheung, Resonance-enhanced laser-induced plasma spectroscopy for sensitive elemental analysis: elucidation of enhancement mechanisms, Appl. Phys. Lett. 81 (2002) 5114–5116.
[13] J.D. Wu, N.H. Cheung, Resonance-enhanced laser-induced plasma spectroscopy for multielement analysis in laser ablative sampling, Appl. Spectrosc. 55 (2001) 366–370.
[14] D.K. Killinger, S.D. Allen, R.D. Waterbury, C. Stefano, E.L. Dottery, Enhancement of Nd:YAG LIBS emission of a remote target using a simultaneous CO_2 laser pulse, Opt. Express 15 (2007) 12905–12915.
[15] O.A. Nassef, H.E. Elsayed-Ali, Spark discharge assisted laser induced breakdown spectroscopy, Spectrochim. Acta Part B 60 (2005) 1564–1572.
[16] W. Zhou, K. Li, Q. Shen, Q. Chen, J. Long, Optical emission enhancement using laser ablation combined with fast pulse discharge, Opt. Express 18 (2010) 2573–2578.
[17] Y. Ikeda, R. Tsuruoka, Characteristics of microwave plasma induced by lasers and sparks, Appl. Opt. 51 (2012) B183–B191.
[18] B. Kearton, Y. Mattley, Laser-induced breakdown spectroscopy: sparking new applications, Nat. Photonics 2 (2008) 537–540.
[19] Y. Liu, B. Bousquet, M. Baudelet, M. Richardson, Improvement of the sensitivity for the measurement of copper concentrations in soil by microwave-assisted laser-induced breakdown spectroscopy, Spectrochim. Acta Part B 73 (2012) 89–92.
[20] Y. Liu, M. Baudelet, M. Richardson, Elemental analysis by microwave-assisted laser-induced breakdown spectroscopy: evaluation on ceramics, J. Anal. At. Spectrom. 25 (2010) 1316–1323.
[21] M. Tampo, M. Miyabe, K. Akaoka, M. Oba, H. Ohba, Y. Maruyama, I. Wakaida, Enhancement of intensity in microwave-assisted laser-induced breakdown spectroscopy for remote analysis of nuclear fuel recycling, J. Anal. At. Spectrom. 29 (2014) 886–892.
[22] L. Liu, S. Li, X.N. He, X. Huang, C.F. Zhang, L.S. Fan, M.X. Wang, Y.S. Zhou, K. Chen, L. Jiang, J.F. Silvain, Y.F. Lu, Flame-enhanced laser-induced breakdown spectroscopy, Opt. Express 22 (2014) 7686–7693.
[23] L. Liu, X. Huang, S. Li, Y. Lu, K. Chen, L. Jiang, J.F. Silvain, Y.F. Lu, Laser-induced breakdown spectroscopy enhanced by a micro torch, Opt. Express 23 (2015) 15047–15056.
[24] Z. Hou, Z. Wang, J. Liu, W. Ni, Z. Li, Combination of cylindrical confinement and spark discharge for signal improvement using laser induced breakdown spectroscopy, Opt. Express 22 (2014) 12909–12914.
[25] L.B. Guo, W. Hu, B.Y. Zhang, X.N. He, C.M. Li, Y.S. Zhou, Z.X. Cai, X.Y. Zeng, Y.F. Lu, Enhancement of optical emission from laser-induced plasmas by combined spatial and magnetic confinement, Opt. Express 19 (2011) 14067–14075.
[26] P.C. Efthimion, Advances in Laser Assisted Microwave Plasma Spectroscopy (LAMPS), Imaging and Applied Optics Technical Papers, Optical Society of America, Monterey, California 2012, p. ATu1A.2.
[27] A. Khumaeni, T. Motonobu, A. Katsuaki, M. Masabumi, W. Ikuo, Enhancement of LIBS emission using antenna-coupled microwave, Opt. Express 21 (2013) 29755–29768.
[28] A. Kramida, Yu. Ralchenko, J. Reader, NIST ASD Team, NIST Atomic Spectra Database (ver. 5.3)[Online]. Available National Institute of Standards and Technology, Gaithersburg, MD, 2015 (http://physics.nist.gov/asd [2016, January 17]).
[29] A.G. Shenstone, The first spectrum of copper (Cu I), philosophical transactions of the Royal Society of London A: mathematical, Phys. Eng. Sci. 241 (1948) 297–322.
[30] R. Wester, R. Noll, Heuristic modeling of spectral plasma emission for laser-induced breakdown spectroscopy, J. Appl. Phys. 106 (2009) 123302.
[31] R.C. Issac, S.S. Harilal, C.V. Bindhu, G.K. Varier, V.P.N. Nampoori, C.P.G. Vallabhan, Anomalous profile of a self-reversed resonance line from Ba^+ in a laser produced plasma from $YBa_2Cu_3O_7$, Spectrochim. Acta Part B 52 (1997) 1791–1799.
[32] M. Wall, Z. Sun, Z.T. Alwahabi, Quantitative detection of metallic traces in water-based liquids by microwave-assisted laser-induced breakdown spectroscopy, Opt. Express 24 (2016) 1507–1517.

Paper III

In-Situ Laser Measurement of Oxygen Concentration and Flue Gas Temperature Utilizing Chemical Reaction Kinetics

by

Jan Viljanen, Tapio Sorvajärvi, and Juha Toivonen

Optics letters 42(23), 4925-4928 (2017)

In-situ laser measurement of oxygen concentration and flue gas temperature utilizing chemical reaction kinetics

J. VILJANEN[1,*], T. SORVAJÄRVI[1], AND J. TOIVONEN[1]

[1] *Tampere University of Technology, Laboratory of Photonics, P.O. Box 692, FI-33101 Tampere, Finland*
[*] *Corresponding author: jan.viljanen@tut.fi*

Compiled November 14, 2017

Combustion research requires detailed localized information on the dynamic combustion conditions to improve the accuracy of the simulations and hence improve the performance of the combustion processes. We have applied chemical reaction kinetics of potassium to measure local temperature and O_2 concentration in flue gas. Excess of free atomic potassium is created into the measurement volume by photofragmenting precursor molecule such as KCl or KOH that are widely released from solid fuels. The decay of the induced potassium concentration is followed with an absorption measurement using a narrow linewidth diode laser. The temperature and O_2 concentration are solved from the decay curve features using equations obtained from calibration measurements in temperature range of 800-1000 °C and in O_2 concentrations of 0.1-21 %. Local flue gas temperature and O_2 concentration were recorded in real time during devolatilization, char burning and ash cooking phases of combustion in single particle reactor with 5 Hz repetition rate. The method can be further extended to other target species and applications where the chemical dynamics can be disturbed with photofragmentation.

OCIS codes: (120.1740) Combustion diagnostics; (120.6780) Temperature; (280.1545) Chemical analysis; (280.4788) Optical sensing and sensors; (300.1030) Absorption;

http://dx.doi.org/10.1364/ao.XX.XXXXXX

Laser spectroscopy allows authentic nonintrusive analysis of combustion chemistry. Various methods based on absorption spectroscopy have shown to be simple and effective for chemical analysis in combustion environment. Wavelength modulation spectroscopy (WMS) and tunable diode laser absorption spectroscopy (TDLAS) have been used to analyze multiple different major combustion gas components O_2 [1], CO_2[2], H_2O[3], NO[4], CO[4] and temperature [2, 3, 5] as well as trace gas species such as gaseous potassium [6]. However, these methods have not been able to deliver localized information on flame temperature or O_2 concentration. Multiple methods, in addition to conventional probe method [7], have been proposed to provide the desired localized temperature information on combustion flames and some of these techniques have also shown capability to map O_2 concentrations. Planar laser induced fluorescence (PLIF) has been used to obtain 2-dimensional single pulse measurement on temperature contours in flames [8] as well as do imaging of O_2 concentration [9]. Phosphorescence effect has also been used for temperature mapping by seeding the flame with thermographic phosphors [10]. Also use of scattering techniques has been introduced to temperature and molecular concentration mapping in flames [11].

Concern of environmental aspects and increasing price of fossil fuels are driving power production towards renewable and CO_2 neutral fuels, such as biomass. Biomass fuels contain alkali and chloride species whose fate in combustion processes has been under interest due their problematic nature in combustion boilers [12]. Monitoring of the alkali species has been tackled with absorption methods. Simultaneous measurement of potassium (K), potassium hydroxide (KOH) and KCl has been introduced with collinear photofragmentation and atomic absorption spectroscopy (CPFAAS) [13, 14].

In this letter, temporal behavior of flue gas temperature and O_2 concentration during combustion of biomass are measured using calibrated reaction dynamics of atomic potassium after a photofragmentation event. The measurement arrangement is analogous to CPFAAS [14]. It exploits the presence of the potassium chloride (KCl) and potassium hydroxide (KOH) in the flue gas. The excess of atomic potassium is created with a photofragmenting UV laser pulse, and the reaction rate back to the equilibrium is followed by absorption measurement of atomic potassium using a narrow linewidth continuous wave laser. Thus the method provides information from volume of fragmenting laser beam that contains KCl or KOH compounds in the gas phase. Calibration of the reaction parameters was carried out with KCl vapor in an oven, and the method was further applied in a single particle combustion reactor during black liquor droplet combustion. The technique provides temporal profiles of the flue gas temperature and O_2 concentration showing expected temporal behavior finally settling on the predefined furnace values. The short measurement path length of about 1 cm and fine temporal resolution indicates that this method can be utilized for temporal analysis of local parameters

in gas phase where photofragmentation can be induced.

Under lean combustion conditions reaction

$$\mathrm{K} + \mathrm{O_2} + \mathrm{M} \underset{k_{-1}}{\overset{k_1}{\rightleftharpoons}} \mathrm{KO_2} + \mathrm{M} \quad (1)$$

plays an important role in determining the dynamics of atomic potassium [15–17]. In stable conditions, Eq. 1 is in equilibrium state in which the forward and reverse reaction rates are equal. This equilibrium state is described by an equilibrium constant that can be defined using the minimum of Gibbs′s free energy

$$\ln K_{eq} = -\Delta G/RT. \quad (2)$$

The equilibrium constant determines the ratio of partial pressures of reactants and products for Eq. 1 with relation

$$K_{eq} = \frac{[\mathrm{KO_2}]p^0}{[\mathrm{K}]_0^{res}[\mathrm{O_2}]}, \quad (3)$$

when ideal behavior of Eq. 1 is assumed. Addition of atomic potassium with photofragmentation from KCl or KOH leads the reaction to proceed forward with reaction rate k_1 to revert to the equilibrium state. Generally, the concentration of the induced potassium $[\mathrm{K}]_0$ decays exponentially

$$[\mathrm{K}] = [\mathrm{K}]_0 \exp(-k_1 t). \quad (4)$$

The reaction rate k_1 has been found to be function of temperature and O_2 concentration with the relation $k_1 = 1.2417 \times 10^{-9}[\mathrm{O_2}]T^{-0.733}$ cm^3 K molecules^{-1} s^{-1} in temperature range of 477-1050 °C [15]. However, in temperatures over 800 °C the atomic potassium concentration decays in double exponential manner. In the first phase k_1 potassium forms reversibly potassium superoxide (KO_2) as described above. In the second phase k_2, that is in range of two orders of magnitude slower decay than k_1, the intermediate and/or the reactant diffuses irreversibly away from the volume of the fragmenting beam and the potassium concentration settles back to the initial surrounding equilibrium [15]. The second phase follows exponential

$$[\mathrm{K}] = [\mathrm{K}]_0^{res} \exp(-k_2 t), \quad (5)$$

where $[\mathrm{K}]_0^{res}$ is the potassium concentration at the equilibrium of Eq. 1. As Eq. 1 is considered to be the only fast decay path for potassium, the concentration of induced KO_2 can be written as $[\mathrm{K}]_0 - [\mathrm{K}]_0^{res}$. It suggests that measurement of the reaction rate and the equilibrium concentration of the potassium atoms in Eq. 1 enables solving the temperature and O_2 concentration in the measurement volume.

The atomic potassium population was deviated from the steady state by photofragmenting KCl or KOH molecules that induced potassium atoms to the measurement volume. The precursor molecules, KCl or KOH, were fragmented using pulsed UV lasers emitting at 266 nm (FQSS 266-200, CryLas GmbH) or at 320 nm (NT342/1/UVE, Ekspla Ltd.), respectively. The evolution of potassium concentration was followed with a narrow linewidth distributed feedback diode laser (Nanoplus GmbH) having emission wavelength locked to the potassium D2 absorption line at 766.5 nm using a reference potassium cell (SC-K-19 75-Q-W, Photonics Technologies). The probe beam was aligned using dichroic mirrors to overlap with the fragmenting beam in the desired measurement volume so that the relative potassium concentration changes due the fragmentation and the relaxation kinetics can be recorded as varying transmission of the probe beam. The temporal intensity of the probe beam was measured

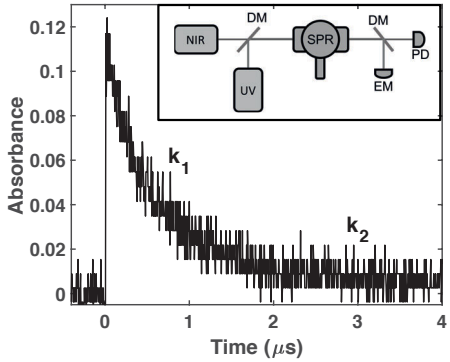

Fig. 1. Temporal evolution of probe laser absorbance. k_1 is the decay constant of the first phase and k_2 the decay constant of the second phase of the decay. Schematic presentation of used measurement arrangement is presented in the inset: Probe laser, NIR; fragmenting laser, UV; dichroic mirrors, DM; single particle reactor, SPR; energy meter, EM; photodiode, PD.

using amplified photodetector (PDA10A, Thorlabs) and a 12-bit oscilloscope (HDO6054, LeCroy).

The obtained PD-voltage curves were converted to absorbance and further to concentration c by applying Beer-Lambert law

$$\alpha L = \sigma c L = -\ln[I(t)/I(t<0)]. \quad (6)$$

However, note that the absolute concentration is not important as only relative change in concentration is considered and, hence, also line broadening effects can be neglected. Figure 1 shows an example of temporal absorbance curve. The fragmenting UV pulse is launched at $t = 0$ resulting a rapid increase in absorbance. The peak of the curve indicates the initial induced potassium atom population $[K]_0$ in the measurement volume. In the obtained absorbance curve, the decay constant k_1 is equivalent to reaction rate k_1 and can be determined through fitting an exponential function to the first phase of the measured decay curve. The equilibrium concentration $[\mathrm{K}]_0^{res}$ of potassium in the predominant conditions is determined by fitting an exponential function to the second phase of the decay curve and extrapolating it to $t = 0$.

The theoretical dependencies were validated with calibration measurements using a quartz tube furnace. KCl powder was set inside the sample cell in 10 cm long glazed combustion boat. The atmosphere in the sample tube was controlled using a mass flow controller (5850S, Brooks Instruments) diluting dry synthetic air with nitrogen. The tube was flushed for 5 min before each measurement with desired gas mixture. The gas flow was closed 2 min before the measurement to let the gaseous KCl partial pressure reach its equilibrium. The precursor molecule was chosen to be KCl due its easy behavior even in high temperatures. KOH reacted strongly with the sample tube which interfered the measurements. Few successful measurements with KOH showed that the reaction path of the free gaseous potassium does not depend on the precursor molecule and therefore the calibration done with KCl can be also used for temperature and O_2 concentration measurement in flue gas using KOH molecules.

The factor $-\Delta G/R$ of Eq. 2 was measured by varying the temperature with fixed O_2 concentration to determine the tem-

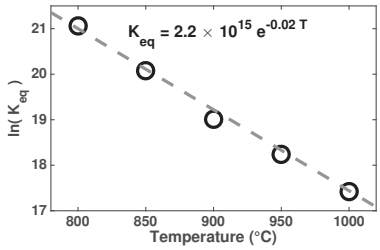

Fig. 2. Logarithm of the equilibrium constant K_{eq} measured in 21 % of oxygen in temperature range of 800-1000 °C

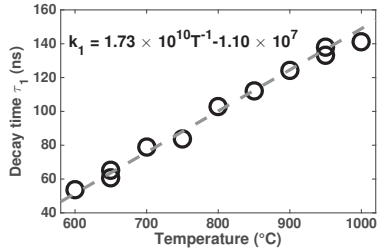

Fig. 3. Decay time of induced potassium concentration $\tau_1 = 1/k_1$ as function of temperature measured in 21 % of O_2.

perature dependency of the equilibrium constant. The obtained graph is shown in Fig. 2 with K_{eq} being defined by Eq. 3. In temperatures lower than 800 °C, Eq. 1 does not yield to large enough equilibrium concentration $[K]_0^{res}$ that would be detectable with the arrangement used in these experiments. This causes the equilibrium measurement to focus only to high temperature conditions. Fitted function for equilibrium constant as a function of temperature was $K_{eq}(T) = 2.2 \times 10^{15} \exp(-0.02T)$. This also confirms the theoretically anticipated relation between K_{eq} and T.

Temperature and O_2 concentration dependencies of the reaction rate constant k_1 are presented in Fig. 3 and in Fig. 4. In the calibration measurements, the reaction rate constant k_1 shows linear behavior against inverse of the temperature with $k_1 = 1.73 \times 10^{10} T^{-1} - 1.10 \times 10^7$ at the range of 600-1000 °C. Also, the reaction rate k_1 behaves linearly as function of O_2 concentration in partial pressures over 10^{-3}. In lower partial pressures the reaction between potassium and O_2 becomes slow enough to other decay mechanisms to affect to the measured decay constant diverting the measured points off from the linear curve. The linear fit $7.48 \times 10^7 [O_2] - 1.95 \times 10^{-9}$ in O_2 partial pressures over 10^{-3} was used due the uncertainty of the decay processes in lower partial pressures. Effect of major combustion gases CO_2 and H_2O to the potassium decay curve was also studied but no change in the curve features were found. The obtained calibration functions are compiled into a pair of equations to solve temperature and O_2 concentration utilizing potassium kinetics

$$\begin{cases} \frac{([K]_0 - [K]_0^{res})p^0}{[K]_0^{res}[O_2]} = 2.2 \times 10^{15} \exp(-0.02T) \\ 1.73 \times 10^{10} T^{-1} - 1.10 \times 10^7 = 7.48 \times 10^7 [O_2]. \end{cases} \quad (7)$$

The obtained pair of equations was applied to solve the temporal behavior of temperature and O_2 concentration of flue gas in a single particle reactor. The reactor is a quartz glass tube with tube diameter of 5 cm placed inside an electrically heated oven [18]. The fragmenting laser beam and the probe beam were aligned through the front and back view ports of the reactor as shown in the inset of Fig 1. Black liquor (570) droplet was used as sample fuel. The sample droplet placed to a platinum hook was inserted from the side port and set to the center of the reactor. Laser beams were aligned to pass the fuel 7 mm above the droplet where the interaction length of laser beam with released KCl and KOH was approximated to be 1 cm corresponding the size of the flame. The gas flow rate was set to 220 (standard)L/h and the combustion gas components N_2 and O_2 were blended with Bronkhorst mass flow controllers. The O_2 concentration in

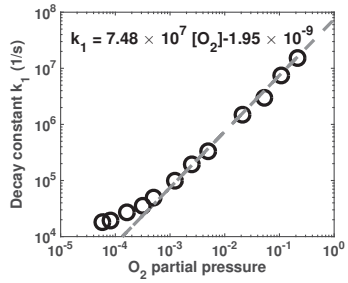

Fig. 4. Decay constant of induced potassium concentration k_1 as function of O_2 partial pressure is linear in pressures over 10^{-3}. The measurement was done in furnace temperature of 600 °C.

the combustion gas was measured with gas analyzer (AO2020 ABB) to be 11.13 %. KOH was used as precursor molecule to induce the atomic potassium to the measurement volume in the single particle reactor measurements due its availability in black liquor flue gas throughout the measurement. The time traces of temperature and O_2 concentration recorded during devolatilization, char burning and ash cooking phases in combustion temperature of 950 °C are shown in Fig 5. The method is validated in temperature range from 800 °C to 1000 °C with the calibration measurements done in tube furnace. The measured time traces are within this range through char burning and ash cooking providing well resolved temporal local information. During ash cooking phase, the temperature in measurement volume recovers close to the level of set furnace temperature averaging on 961 °C with standard deviation of 9 °C. Also the O_2 concentration recovers to the set level averaging at 11.6 % with standard deviation of 0.4 %. The obtained measures agree well with the set values of the reactor. The systematic deviation in temperature measurement might originate from different locations of furnace controlling thermocouple measurement points and different temperature profiles in the two furnaces. Also, the furnace O_2 concentration is measured from exhaust gas so the measurement location is far away from the flame zone and may lead to a small difference in the results. During devolatilization, the flue gas temperature rises above the calibrated range. However, measured temperature agrees well on surface temperature measurements done for a black liquor droplet [19]. The obtained curves in Fig 5 proposes the methods potential to measure temperature and O_2 concentration in dynamic combustion environment.

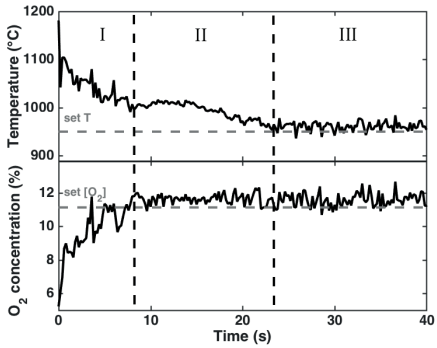

Fig. 5. Temporal behavior of temperature and O_2 concentration measured from black liquor (570) flue gas in single particle reactor. The set temperature of the reactor was 950 °C and the set O_2 concentration in combustion gas was 11.13 %. Dashed lines divide the different phases of combustion: I devolatilization, II char burning and III ash cooking.

The demonstration in single particle reactor shows the applicability of chemical reaction kinetics based temperature and O_2 concentration measurements. By altering the beam path configuration of the lasers from collinear to intercepting, the measurement method can provide localized temperature and O_2 concentration data as the obtained absorption signal is formed only in the beam overlapping volume. In this work, the method was applied to a flue gas flow that was 1 cm wide but by increasing the fragmenting laser pulse energy, the interaction length of absorption can be further shortened. This allows spatially more specified measurements in larger combustion environments. The perpendicular laser beam configuration has already been demonstrated in tube furnace by Sorvajärvi et al. [15]. The range of measurement targets can also be extended by choosing different precursor molecules for the fragmentation, e.g. metal halides [20] and halogenated carbon molecules [21]. Metal halides are relatively easy to fragment due their accessible fragmentation energy and their volatility in reasonable temperatures. Another interesting type of chemical species for photofragmentation are the metal hydroxides [13, 22]. The presented method offers a tool for simultaneous concentration, temperature and O_2 monitoring for example NaOH that is used in many industries as chemical base. It is beneficial to have precursor molecule from which one of the fragments would be atomic since this allows use of strong atomic absorption. In conditions where the induced atomic concentration reaches an equilibrium state with the surrounding, the temperature and reactive compound concentrations can be measured using similar method as presented in this letter.

In conclusion, a novel approach for in-situ flue gas temperature and O_2 concentration measurements using chemical reaction kinetics is introduced. The potassium reaction kinetics with the ambient oxygen was calibrated in temperature range of 800-1000 °C and in O_2 concentrations of 0.1-21 %. The method was applied to measure temperature and O_2 concentration in flue gas released from black liquor droplet and it showed good agreement with the reference values within the calibration range and also in temperatures up to 1100 °C. Alkali compounds are widely present in many solid fuels used for power production [12, 23], therefore, with the spatial scalability and ability to measure in dynamic environment, the proposed method can be used in many combustion applications to obtain localized information on temperature and O_2 concentration. The method has also great potential to be used with other types of precursor molecules and applications, which opens new possibilities in different fields of industry and science.

Acknowledgments. This work has been partly carried out within CLIFF (2014-2017) as part of the activities of Tampere University of Technology.

REFERENCES

1. H. E. Schlosser, J. Wolfrum, V. Ebert, B. A. Williams, R. S. Sheinson, and J. W. Fleming, Proceedings of the Combustion Institute **29**, 353 (2002).
2. A. Farooq, J. B. Jeffries, and R. Hanson, Applied Physics B **90**, 619 (2008).
3. Z. Qu, R. Ghorbani, D. Valiev, and F. M. Schmidt, Optics express **23**, 16492 (2015).
4. R. M. Mihalcea, D. S. Baer, and R. K. Hanson, Measurement Science and Technology **9**, 327 (1998).
5. X. Zhou, J. Jeffries, and R. Hanson, Applied Physics B **81**, 711 (2005).
6. Z. Qu, E. Steinvall, R. Ghorbani, and F. M. Schmidt, Analytical chemistry **88**, 3754 (2016).
7. D. Bradley and K. Matthews, Journal of Mechanical Engineering Science **10**, 299 (1968).
8. J. M. Seitzman, G. Kychakoff, and R. K. Hanson, Optics letters **10**, 439 (1985).
9. W. Koban, J. Schorr, and C. Schulz, Applied Physics B **74**, 111 (2002).
10. A. Omrane, P. Petersson, M. Aldén, and M. Linne, Applied Physics B **92**, 99 (2008).
11. P. Nooren, M. Versluis, T. H. van der Meer, R. Barlow, and J. Frank, Applied Physics B **71**, 95 (2000).
12. H. Nielsen, F. Frandsen, K. Dam-Johansen, and L. Baxter, Progress in energy and combustion science **26**, 283 (2000).
13. T. Sorvajärvi, N. DeMartini, J. Rossi, and J. Toivonen, Applied spectroscopy **68**, 179 (2014).
14. T. Sorvajärvi, J. Saarela, and J. Toivonen, Optics letters **37**, 4011 (2012).
15. T. Sorvajärvi, J. Viljanen, J. Toivonen, P. Marshall, and P. Glarborg, The Journal of Physical Chemistry A **119**, 3329 (2015).
16. A. J. Hynes, M. Steinberg, and K. Schofield, The Journal of chemical physics **80**, 2585 (1984).
17. R. Carabetta and W. Kaskan, The Journal of Physical Chemistry **72**, 2483 (1968).
18. N. Demartini, E. Monedero, P. Yrjas, and M. Hupa, TAPPI JOURNAL **9**, 30 (2010).
19. W. L. Saw, G. J. Nathan, P. J. Ashman, Z. T. Alwahabi, and M. Hupa, Combustion and Flame **157**, 769 (2010).
20. J. Maya, IEEE Journal of Quantum Electronics **15**, 579 (1979).
21. W. H. Pence, S. L. Baughcum, and S. R. Leone, The Journal of Physical Chemistry **85**, 3844 (1981).
22. B. L. Chadwick, P. G. Griffin, and R. J. Morrison, Applied spectroscopy **51**, 990 (1997).
23. L. L. Baxter, T. R. Miles, B. M. Jenkins, T. Milne, D. Dayton, R. W. Bryers, and L. L. Oden, Fuel processing technology **54**, 47 (1998).

Paper IV

Real-Time Release of Na, K and Ca During Thermal Conversion of Biomass Using Quantitative Microwave-Assisted Laser-Induced Breakdown Spectroscopy

by
Jan Viljanen, Haibo Zhao, Zhi-Hao Zhang,
Juha Toivonen, and Zeyad T. Alwahabi
Spectrochimica Acta Part B: Atomic Spectroscopy 149, 76-83 (2018)

Spectrochimica Acta Part B 149 (2018) 76–83

Contents lists available at ScienceDirect

Spectrochimica Acta Part B

journal homepage: www.elsevier.com/locate/sab

Real-time release of Na, K and Ca during thermal conversion of biomass using quantitative microwave-assisted laser-induced breakdown spectroscopy

J. Viljanen[a], H. Zhao[b], Z. Zhang[b], J. Toivonen[a], Z.T. Alwahabi[c,*]

[a] Laboratory of Photonics, Tampere University of Technology, FIN-33101 Tampere, Finland
[b] Key Laboratory of Thermal Science and Power Engineering of Ministry of Education, Department of Thermal Engineering, Tsinghua University, 100084 Beijing, China.
[c] School of Chemical Engineering, The University of Adelaide, S.A. 5005, Australia

ARTICLE INFO

Keywords:
LIBS
Combustion
Microwave
Flame
Calibration

ABSTRACT

Power production with thermal conversion has met new challenges due the global pressure to use CO_2 neutral and renewable fuels, e.g. recycled fuel and biomass. Many of these fuels contain high concentrations of elements, such as alkali metals and chlorine, that together are harmful for boiler structures and may cause operational problems. Therefore, detailed quantitative information on release behaviour of the problematic elements, potassium and sodium, is required. For this, a new burner, which allows linear calibration of laser induced breakdown spectroscopy (LIBS) measurement towards higher concentrations relevant for the release studies during thermal conversion of biomass, was designed. The analytical performance of conventional LIBS measurement is significantly improved by introducing microwave radiation to the laser-induced plasma. An enhancement of linearity and up to 60-fold improvement of limit of detection (LOD) was observed with microwave-assisted LIBS (MW-LIBS) in comparison to conventional LIBS. The LOD of Na, K and Ca were 10 ppb, 19 ppb and 16 ppb, respectively. In-flame MW-LIBS measurement was applied to record time-traces of K, Na and Ca during thermal conversion of a poplar pellet. This is the first demonstration of Microwave near-field applicator injected MW-LIBS for gas phase measurement. With broad dynamic measurement range, the proposed method can be applied to extensive research of elemental release behaviour of different fuels. In addition to combustion studies, the MW-LIBS method can be extended to study trace-elements in gas phase in different fields of industry and science.

1. Introduction

Concern of environmental aspects and the increasing price of fossil fuels are driving the power production towards renewable and CO_2 neutral energy sources. This has increased the interest on using low quality fuels, such as communal waste and biomass, for power production. However, these fuels are problematic for combustion boiler operation due to high release rate of alkali compounds [1]. KCl and NaCl have been found to cause severe slagging and fouling in the boiler structures that may lead to operational problems and unplanned shutdowns [2]. Detailed information on the release behaviour of the alkaline compounds is required and it has been under extensive research.

Multiple online methods are used to study the metal species in reactive flows and are extensively reviewed by Monkhouse. [3] Atomic absorption techniques, atomic absorption spectrometry (AAS) [4], differential optical absorption spectrometry (DOAS) [5], and their applications [5,6,7], offer element or molecule specific information but are limited to their specific species present in gas phase. In many combustion applications, it would be in interest to measure the total concentration of an elemental specie. This can be achieved with atomic emission methods, such as excimer laser-induced fragmentation fluorescence (ELIF) [8] or laser-induced breakdown spectroscopy (LIBS) [9] that, however, have limited operational range due the difficulties in calibration for broad measurement range.

LIBS has become one of the leading online elemental analysis techniques. Its ability to provide multi-element analysis, requirement of minimal or even no sample preparation, applicability to solid, liquid, and gas phase, and stand-off capability are the clear advantages of LIBS [11] when compared to other elemental analysis techniques, such as inductively coupled plasma (ICP) analysis methods and X-ray fluorescence (XRF) technology [12]. In recent years, LIBS technique has been widely applied in field of combustion diagnostics. For instance,

* Corresponding author.
E-mail address: zeyad.alwahabi@adelaide.edu.au (Z.T. Alwahabi).

https://doi.org/10.1016/j.sab.2018.07.022
Received 24 December 2017; Received in revised form 18 June 2018; Accepted 17 July 2018
Available online 21 July 2018
0584-8547/

equivalence ratios in laminar premixed flame [13,14], non-premixed flame [14,15], and turbulent partially premixed flame [14,16] were all measured by LIBS. Besides the laboratory flames mentioned above, LIBS has also been utilized for equivalence ratio measurements in spark-ignited engines [17,18]. In addition of the equivalence ratio detection, LIBS was employed for in situ measurement of temperature in partially premixed flame [19].

Measurement of alkali metals in high temperature gases has been under extensive study. Molina et al. [20] studied the effect of the ambient gas to the LIBS signal and found that significant attenuation of the alkali metal LIBS signal occurred, when the stoichiometry of the gas surrounding the spark changed from fuel lean to fuel rich. He et al. [21] have been studying the effect of O_2 and CO_2 to the temporal behaviour of alkali metal release from coal particles and Zhang et al. [22] have recorded the potassium release during combustion of pine wood using LIBS. The LIBS results have also been applied in modelling of the alkali release from biomass fuels [23]. However, in the reported studies the calibration ranges have been limited to concentration of approximately 10 ppm [10,21,22] and this has been hindering extensive alkali release measurements from biomass fuels with more abundant alkali concentrations. Therefore, in order to make the in-flame LIBS detection of alkali metals more accurate and reliable, new LIBS calibration methods, which are able to provide linear calibration curves covering the practical high alkali metal concentration ranges in flame, are urgently needed.

The calibration of laser induced plasma emission signal is associated on the curves of growth, i.e. calibration curves. The curves are expressed to describe the relation between the intensity of the emission and the analyte number density in the plasma [11]. Ideally the calibration curve shows linear relation between the wavelength-integrated emission line intensity and the analytic concentration, and indeed, this is the case in optically thin environment, i.e. when self-absorption is negligible. In optically thick conditions, the linear dependency of the emission on analyte number density is lost due to self-absorption. In the most extreme case the collected analyte emission line is deteriorated by self-reversal effect. Compromises in the analytical performance have to be done to overcome these problems causing the nonlinearities in the curve of growth. Self-absorption either forces to focus on low concentration conditions or leads to a choice of another analyte emission line that is less prone to self-absorption [24]. The lines that are less influenced by the self-absorption usually originate from higher energy levels and therefore the use of these lines for the detection compromises the limit of detection (LOD) in conventional LIBS measurements. Recent development on microwave-assisted LIBS (MW-LIBS) has shown that, in addition to improvement of LOD, microwave assistance is capable to reduce the self-reversal and self-absorption in the plasma plume [25]. This is highly beneficial when measuring high elemental concentration samples that are prone to self-absorption.

The calibration of LIBS signal is not alone affected by the elemental absorption properties but also the calibration sampling plays an important role. The complex nature of interaction between laser and sample and between plasma and sample leads to undesirable matrix-effects. These effects cause variations in plasma properties that are dependent on sample material properties and laser characteristics [11]. Therefore, the calibration sample properties have to match with the actual sample and this may be very difficult to achieve without extensive sample preparation, which would cut down one of the LIBS's advantages. The calibration sample arrangement is not as difficult in the case of gas phase, as it is in solid phase, as the measurement configuration parameters, e.g. lens-to-sample distance and the sample homogeneity, are easy to maintain. However, most elements, e.g. alkali metals and alkaline earth metals, are not commonly found in gas phase and therefore reliable calibration of metallic analytes to high concentration levels have found to be challenging. Controlled gas phase concentrations have been produced by evaporating salt compound containing the desired analyte letting the vapour pressure reach equilibrium [26]. Even though the equilibrium method can produce considerable concentration of the analyte into the gas phase, it requires very stable atmosphere to reach the equilibrium. Therefore, this method is rarely suitable for LIBS applications. The salt can be also seeded into the measurement volume as aerosol. Aerosol is produced with nebulizer and carried with gas flow into a heated measurement volume where the aerosol is vaporized [10]. However, in the seeding method demonstrated by Hsu et al. [10] the aerosol is carried to the flame by the combustion gas that limits the ability to vary the amount of aerosol injected into the flame. High concentration calibration would require high number of aerosol droplets injected into the flame. In the former design variation in the carrier gas flow would lead variation in the flame properties that would compromise the validity of the calibration. On the other hand, changing the analyte concentration in the nebulized solution affects to the efficiency of nebulization, hence, may lead to nonreliable calibration of the measurement.

This paper addresses the issues in quantitative LIBS calibration related to combustion studies by using novel approach for analyte seeding. This was achieved by introducing aerosol containing the analye to centre of the flame only using novel burner design. The analytical performance was further improved introducing microwave-assistance to the laser induced plasma with a microwave near-field applicator (NFA) [27]. NFA injected MW-LIBS has previously been applied to solid [25] and liquid [28] phase measurements. This study is the first demonstration of NFA in gas phase measurement. MW-LIBS has the ability to reduce self-absorption in high concentration conditions and improve LOD [25]. LIBS and MW-LIBS performances are compared in terms of LOD and linearity of the calibration curves for K, Na, and Ca. The obtained calibration curves are applied to measure temporal release curves of K, Na, and Ca during thermal conversion of poplar pellet inside the flat flame to demonstrate the applicability of the method in a biomass combustion environment.

2. Experimental set-up

2.1. Calibration sample seeding and burner design

Fig. 1. shows a Hencken style flat flame burner with a single seeding tube in the centre. The burner was designed to provide a well-controlled combustion environment and suitable quantitative seeding of alkali salt solutions to the flame. The flat flame burner consists of an inner brass tube and an outer brass tube with the inner diameter of 23.4 mm and 40.5 mm, respectively. The inner brass tube is divided into two parts and connected by a fringe in the bottom part. The burner can be divided into four main parts, namely fuel jets, air co-flow, N_2 shroud flow, and seeding flow. There are 58 stainless steel hypodermic tubes with the diameter of 1 mm, which are fixed evenly on a stainless-steel disk in the connecting fringe. CH_4 is fed through a packed bed into all the tubes to ensure a uniform fuel flow in each tube. These tubes convey CH_4 to the outlet of the burner and emerged as the fuel ports on the surface of the honeycomb. The combustion air flows into the inner brass tube via side tubes and is conveyed upstream through a packed bed and a stainless-steel honeycomb, forming the co-flow. Each fuel jet is directly adjacent to 6 hexagonal air co-flows to form the uniform flat flame. The shroud N_2 flow is fed into the outer brass tube via side tubes and through a packed bed and a stainless-steel honeycomb to stabilize the inner flat flame. The central tube with a diameter of 1 mm was used to seed the salt droplets into the flame in the LIBS calibration system.

The seeding was realized using salt solutions that were nebulized and carried into the flame. An ultrasonic nebulizer was employed to produce a fog of droplets from different salt compound (KCl, NaCl or $CaCl_2$) solutions in a sealed tank. A flow of pre-mixed CH_4 and air passing through the tank carried the nebulized droplets via the central hypodermic tube that was drilled through the bottom of the inner brass tube into the centre part of the flat flame. The droplets were vaporized by the heat when injected into the flame. By changing the flow rate of

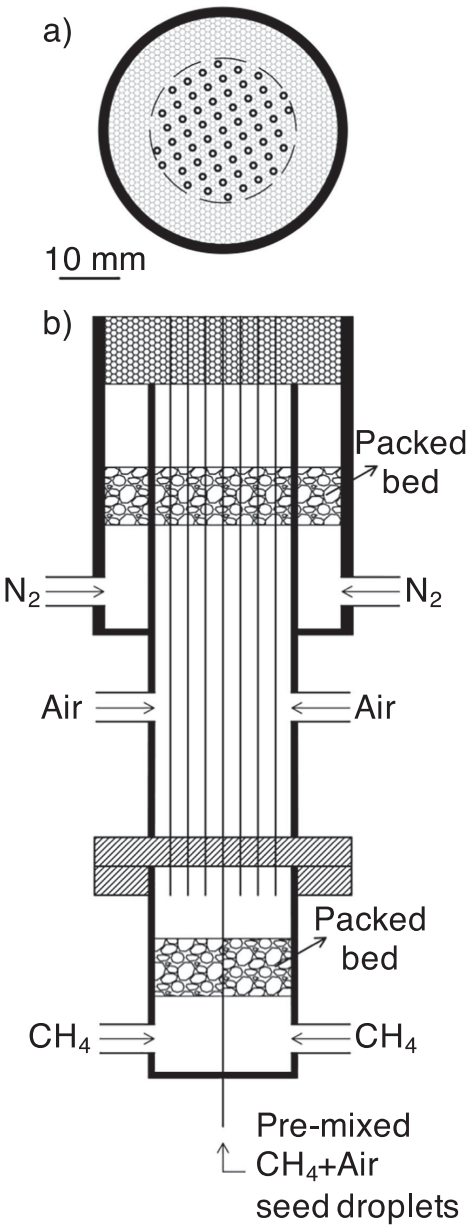

Fig. 1. The sketch of the flat flame burner. a) Top view, b) cross-section view.

the carrier gas, the seeding rate of the droplets of the solutions into the flame could be precisely controlled. Thermal mass flow controllers (MFCs) from Bronkhorst High-Tech were used to determine the separate flows of CH_4, air and nitrogen.

In order to make the flat flame working in the lean and temperature stable condition in the LIBS calibration experiment, the flow rate of the air and fuel CH_4 were set to be 5.0 L/min (STP) and 410.0 mL/min (STP), respectively. Therefore, the equivalent ratio was about 0.78. The equivalent ratio of the seeding flow was also set to be 0.78. The flow rate of the seeding flow was controlled in the range from 10 to 180 mL/min (STP) for this study.

A gravimetric approach was used to determine the mass flow of salts into the flame. The nebulizer tank was weighted before and after a seeding period of 12 h on an analytical balance to evaluate the rate of mass loss. The concentrations of the NaCl, KCl and $CaCl_2$ solutions in the nebulizer tank were 100 g/L that was found to be close to the maximum to maintain nebulizer operation constant and to avoid blockage of pipes. It was observed that the droplet generation by the nebulizer was much faster than the seeding depletion up to flow rate of 110 mL/min after which the droplet density started to decrease in the reservoir tank. Thus, it is assumed that the number density and droplet size in the nebulizer tank did not change when the seeding CH_4 flow rate changed in range of 10 to 100 mL/min. As a result, the liquid mass consumption rates between the seeding flow rate of 10 mL and 100 mL/min were calculated by interpolation, and the seeding rate of the alkali compound into the flat flame could be given

$$SR_a = A \cdot Q_{neb} \cdot SC \quad (1)$$

where SR_a is the seeding rate (g/min) of the alkali compound into the flat flame, A is the mass loss constant for the solution, Q_{neb} is the seeding flow rate (mL/min), and SC is the alkali compound solution concentration (g/mL) in the nebulizer tank.

2.2. MW-LIBS arrangement

A schematic presentation of the optical measurement arrangement is shown in Fig. 2. Laser induced plasma was achieved by focusing a frequency doubled Nd:YAG laser pulse with wavelength of 532 nm, 8 ns pulse width, 10 Hz repetition rate and 70 mJ pulse energy (Quantel YG) 22 mm above the burner surface. The laser pulse energy was tuned with a Glan laser polarizer and a half-wave plate to provide stable and repeatable plasma in the measurement conditions used in the study. With 70 mJ the laser induced plasma plume size was sufficiently small to avoid contact and, hence, contamination from the NFA. A plano-convex lens with 100 mm focal length was used to focus the laser in the centre of the flame. The plasma emission was collected with a perpendicular collection arrangement using two plano-convex lenses with 100 mm and 50 mm focal length to collect the plasma emission in to an optical fibre having 1 mm core diameter (Thorlabs). The emission was separated into a spectrum using Andor Shamrock monochromator (SR-500) equipped with 2400 g/mm and 1200 g/mm gratings. The spectral resolution of the spectrometer, with the 2400 lines/mm grating, is 0.031 nm at ~325 nm, with a resolving power of 10,000. The spectra were recorded with Andor iStar ICCD camera.

Pulsed microwave radiation with 1.5 ms pulse width and 600 W peak power was generated with Sairem microwave system. The radiation was coupled into a coaxial cable (50 Ω NN cable) with attenuation of 0.14 dB @ 2.45 GHz using a waveguide-to-coaxial adaptor. The maximum power level was chosen to be 600 W to avoid overheating in the adaptor when using microwave pulses with duration over 1 ms. This, however, was not limiting significantly the enhancement effect as the enhancement factor saturates when microwave power is increased [25,28]. Radiation was delivered to the laser induced plasma using specially designed NFA [27]. The NFA was placed 0.5 mm away from the laser induced plasma in perpendicular orientation in respect to laser pulse propagation. The microwave pulse was launched 300 μs before laser pulse to ensure that microwave power reaches the maximum level when the initial plasma plume is ignited by the laser pulse. However, the microwave radiation is not absorbed to the plasma instantly after its ignition due the high electron density in the early state of the laser induced plasma. The initial plasma electron density was approximated to be 7×10^{18} cm^{-3} using the stark broadening of hydrogen emission line at 656.27 nm [29]. Microwave radiation can penetrate the plasma surface when the plasma electron density is sufficiently decayed. The electron density of microwave-maintained plasma was approximated to be 8×10^{15} cm^{-3}. More detailed description of the interaction between

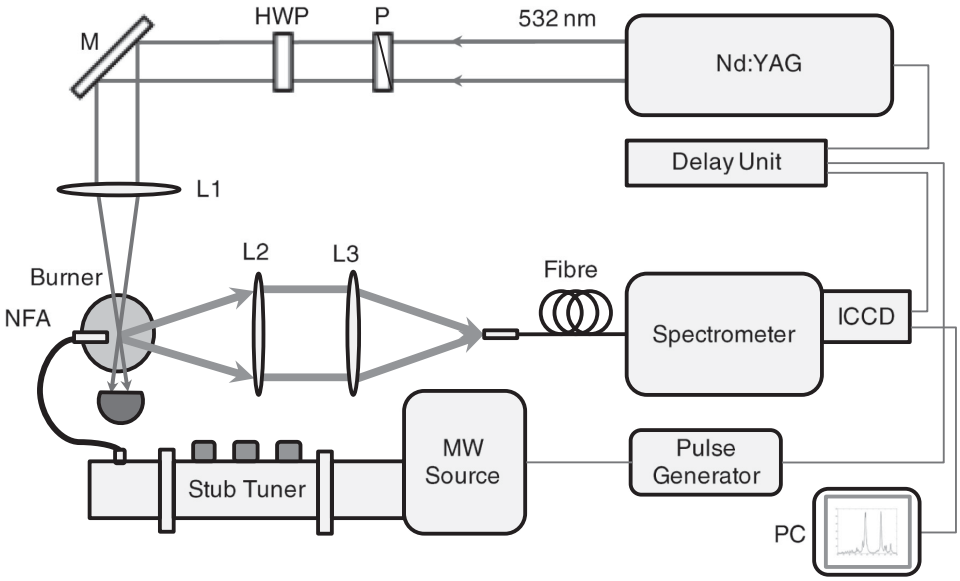

Fig. 2. The experimental arrangement used for Na, K and Ca detection during biomass combustion: polarizer, P; half-wave plate HWP; mirror, M; lens, L; near-field applicator, NFA.

NFA injected microwave radiation and plasma is a topic of another research.

3. Results and discussions

3.1. Burner and seeding characteristics

The radial temperature profile of the flame in used biomass thermal conversion conditions is shown in Fig. 3. The temperature was measured with an R-type thermocouple and corrected for radiation. It is seen from Fig. 3 that the radial temperature profile of the flame is spatially uniform (< 80 K) within the radius of 4 mm at the LIBS measurement height of 22 mm from the burner surface. At 22 mm above the surface burner, the flame has the maximum temperature of 1497 ± 60 K at the centre line.

The average concentration of the analyte species inside the flat flame could be calculated with knowledge of the alkali compounds

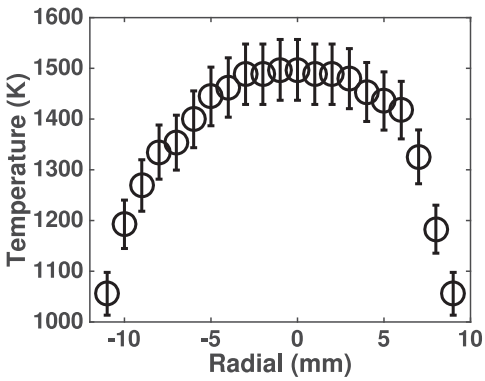

Fig. 3. Radial flame temperature, at 22 mm above the burner surface, with equivalence ratio of 0.78.

seeding rate, as presented in Eq. 1, the flow rate of the fuel and air, and the seeding flow rate. The horizontal average of analyte concentration (volume of the alkali elements per volume of the gas) is given by the following equation

$$C_a = \left(\frac{n \bullet SR_a}{MW_a}\right) \Big/ \left((Q_{fuel} + Q_{air} + Q_{neb}) \cdot \frac{P}{RT}\right) \bullet 10^6 \quad (2)$$

where C_a is the average analyte concentration (ppm) on a horizontal plane of the flat flame at any height above the burner surface, n is the atomic number of the target atomic element in the compound, MW_a (g/mmol) is the molecular weight of the analyte compound, Q_{fuel} is the flow rate of the fuel CH_4, Q_{air} is the flow rate of the air, P is the atmospheric pressure, R is the universal gas constant, and T is the temperature in standard condition.

However, the distribution of analyte species in the flame is influenced by the seeding rate. To obtain the actual concentration of the seeded analyte in the measurement spot, the average value from Eq. 2 has to be corrected using a distribution function. The relative lateral distribution of the analyte concentration on the measurement height of 22 mm with different flow rates were measured using LIBS measurement. Sodium was used as a target analyte in this measurement and it was seeded as NaCl into the flame. The measured distributions are presented in Fig. 4. The measured emission intensities of sodium D1 line were fitted with Gaussian distribution function that was assumed due diffusion behaviour of molecular species. Using these distribution functions, the average analyte concentration in the flame obtained with Eq. 2 was corrected to correspond the concentration in the centre of the flame that was used as the measurement point.

3.2. Spectral profile correction

The acquired LIBS emission line spectrum is affected by the absorption to the atomic population in the surrounding flame, in addition to the self-absorption familiar from previous LIBS studies [10], as Molina et al. have noted [20]. A theoretical correction is applied to the recorded spectrum to circumvent the nonlinear relation between the concentration and signal intensity caused by self-absorption, both in

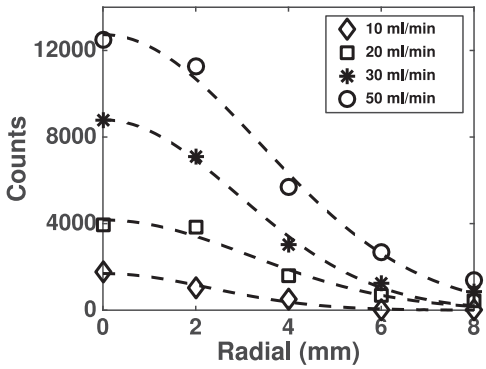

Fig. 4. Concentration profile in the flame on different seeding flow rates. The measurement points are fitted with Gaussian curves that were assumed due diffusion behaviour of molecules.

plasma and in the surrounding flame. The recorded spectrum S(ω) is a product of two optical processes, namely, emission from the excited atoms H(ω) and absorption by the atoms at the ground state G(ω)

$$S(\omega) = H(\omega)G(\omega) = \frac{I}{1+\left(\frac{2(\omega-\omega_0)}{\gamma}\right)^2} exp\left(-\frac{\alpha L}{1+\left(\frac{2(\omega-\omega_0)}{\sigma}\right)^2}\right) \quad (3)$$

where I is the intensity at the emission maximum, γ and σ are the full width at half maximum of emission and absorption profile, respectively, and αL is the absorbance. The recorded spectrum was fitted with Eq. 3 using nonlinear least squares method with four independent variables, I, αL, γ and σ. Based on the best fit, the value of I is extracted. An example of the fitting process is shown in Fig. 5. The extracted emission intensity profile is then integrated and compared against seeded analyte concentration in the flame to obtain the calibration data and further the desired release information.

As shown in Fig. 6, the integrated H(ω), named self-absorption corrected MW-LIBS signal, has a linear relation to the seeded Na concentration. In contrast, the integral of S(ω) suffers from the self-absorption and the linearity of the calibration is compromised leading to quadratic relation between seeded Na concentration and the signal counts in the calibration range. The extended linear range of the calibration curve compared to previous studies [10,21,22] improves the analytical sensitivity and reliability in high concentration environment

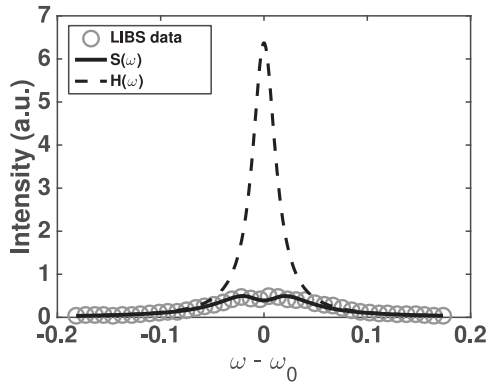

Fig. 5. An example of absorption correction with the fitting method. S(ω) is the fitted line shape to the measured signal marked with circles and H(ω) is the emission profile extracted from the fitted function.

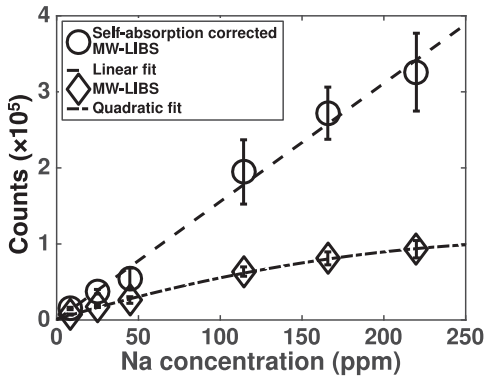

Fig. 6. The effect of self-absorption correction to the calibration curve. Error bars represent the standard deviation of 200 measured laser shots.

and enables use of the method to measure alkali release behaviour from high alkali content fuels. It can also be noted that the relative standard deviation of the measured counts does not significantly increase due the spectral fitting procedure when standard deviations of 200 measured laser shots are compared.

3.3. MW-LIBS calibration

The calibration for Na, K, and Ca was conducted with both LIBS and MW-LIBS methods to establish the performance and response of the system. For LIBS measurement, the optimal gate width and gate delay, in terms of signal to noise ratio (SNR), were determined separately for each analyte element and are listed in Table 1. Measurement of K required much longer delay time to Na and Ca due interfering emission from other species present in the laser induced plasma that decayed in approximately 8 μs and enabled clearer distinction of K emission line. For MW-LIBS measurement the gate delay for each element was the same as in LIBS measurement and the gate width used for all was 1 ms. The ICCD camera gain for LIBS measurements was set on 100 whereas for MW-LIBS measurements the gain was set on 1 to avoid detector saturation in high concentration conditions. Examples of collected MW-LIBS and LIBS single shot K spectra are presented in Fig. 7. The data points used for calibration are averages of 200 laser shots.

The obtained calibration curves for Na, K and Ca are presented in Fig. 8. It was noted that the nebulizers ability to maintain the saturated condition in the sample reservoir was seed molecule dependent. It was visibly observed that with high injection flows the aerosol cloud inside the reservoir became less dense. Also, as the injection flow exceeded the threshold with which the nebulizer could not maintain saturated condition, the calibration curve showed a plateau and therefore calibration range varies between the elements. The measured points are fitted with linear curves. The slopes of the fitted curves are listed in Table 2. The calibration curves for MW-LIBS measurements are significantly steeper than those of LIBS measurements and possessed better linearity in terms of R^2 value. This indicates better sensitivity for MW-LIBS measurements. To compare the performances further, the LOD for LIBS and

Table 1
Elemental emission lines used in measurements and the optimized gating settings.

Element	Wavelength (nm)	A_{ki} [30] (10^7 s^{-1})	E_i [30] (eV)	E_k [30] (eV)	Gate delay (μs)	Gate width (μs)
Na	588.995	6.16	0.00	2.10	2.0	15.0
K	766.490	3.8	0.00	1.62	9.0	8.0
Ca	422.673	2.8	0.00	2.93	0.5	6.0

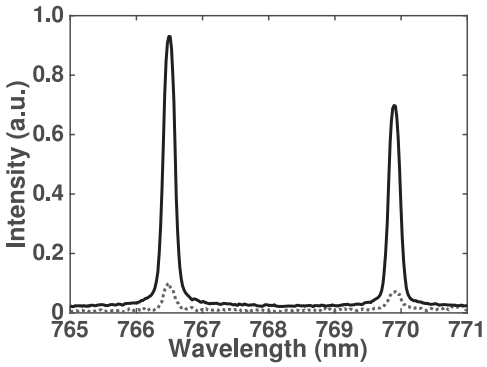

Fig. 7. Typical single shot K D-line spectrum. Spectra acquired with MW-LIBS is presented with solid line and LIBS with dotted line.

MW-LIBS were calculated using

$$LOD = ks_b/b \quad (4)$$

condition where k = 3, s_b is the standard deviation of the background and b is the slope of the calibration curve [11]. The computed LOD's are listed in Table 2. It shows that microwave-assisted LIBS has the ability to extend the detection range in the low concentration cases with up to 60-fold improvement of LOD when compared to conventional LIBS. The achieved LOD's for Na and K are also improved by over 3-fold when compared to the lowest LOD's reported in previous flame studies [10]. The LOD's are significantly lower than those reported for other elements in solid and liquid samples [25,28] due the high-temperature environment where the sample is already vaporized and the energy required to dissociate the alkali containing molecules is reduced. It is worth emphasizing that increasing the detector gain during MW-LIBS measurement would further lower the LOD, however, this would lead to detector saturation in high concentration case that was not desirable in the current application.

3.4. Temporal quantitative measurement of alkali release during thermal conversion of biomass

An application of the measurement technique is demonstrated measuring temporal total elemental release during thermal conversion of biomass samples. The samples were grained and pressed to pellets. Poplar was chosen as the sample to work with due to steady and repeatable behaviour during the conversion. The composition of ash-forming elements in the poplar was studied with chemical fractionation [31] and the results are presented in Table 3. The pellet with inset dimension of 2.5 mm in diameter was set to the centre of the burner 5 mm above the burner surface using platinum wire. The MW-LIBS measurement was conducted at a distance of 14.5 mm above the particle surface. This measurement location was > 5 times the particle dimeter, so that the flame disturbance is minimal as observed previously [10,22]. To be able to use the line fitting method, MW-LIBS spectra were collected with relatively high spectral resolution. The maximum spectral range was ~13 nm which not enough to cover the selected lines of K, Na and Ca at 766.49 nm, 488.995 nm and 422.673 nm, respectively. It was necessary to record the release patterns of different species separately.

The obtained time-traces of Na, K and Ca release are shown in Fig. 9. As expected, the more volatile Na, and K have much higher release rate than the Ca that is known to be mostly left into the bed ash [32]. A slight increase in Ca release rate is recorded during devolatilization phase while during char burning phase Ca MW-LIBS emission signal is hovering close to LOD. The release rate of K towards the end of char burning rises above the calibration range, hence these values

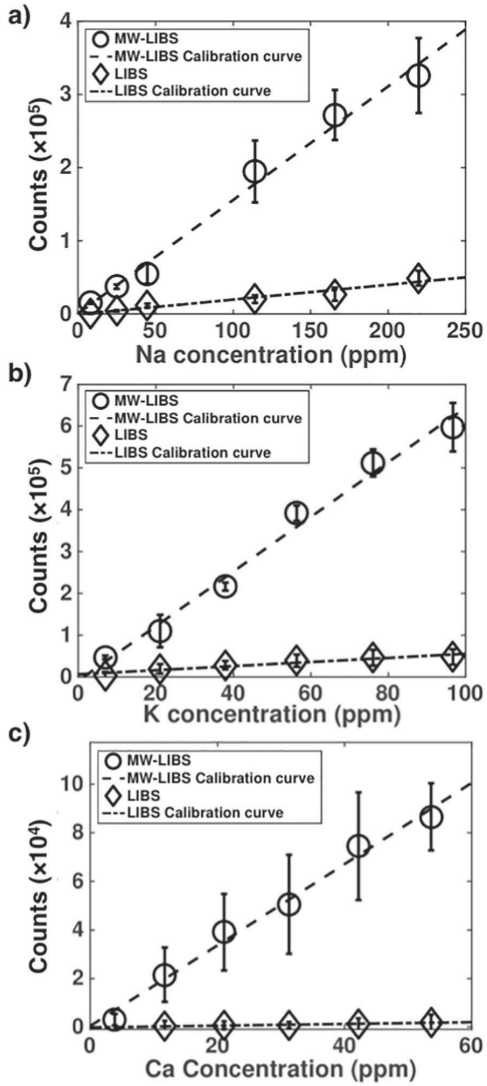

Fig. 8. Calibration curves for a) Na, b) K and c) Ca. Error bars represent the standard deviation of 200 measured laser shots.

Table 2
Elemental calibration slopes and limits of detection achieved in this work and reported in previous flame studies.

	LIBS					MW-LIBS		
Element	Slope (counts/ppm)	R^2	LOD (ppb) this work	LOD (ppb) previous work	Ref.	Slope (counts/ppm)	R^2	LOD (ppb) this work
Na	407.3	0.95	125	29	[10]	3108.8	0.98	10
K	490.8	0.91	408	72	[10]	6536.2	0.99	19
Ca	35.9	0.94	945			1668.6	0.99	16

cannot be considered reliable in terms of quantitative measures. However, the trend is clear that the relative K release is very high in the end of char burning. The release pattern of Na and K follows similar trend as

Table 3
Ash-forming elements in the poplar sample.

Element	Cl	K	Na	Ca	Si	Al	Fe	Mg	Mn	P	S
Mass fraction (mg/kg)	702	2910	39.3	4150	102	31	61	445	4	858	196

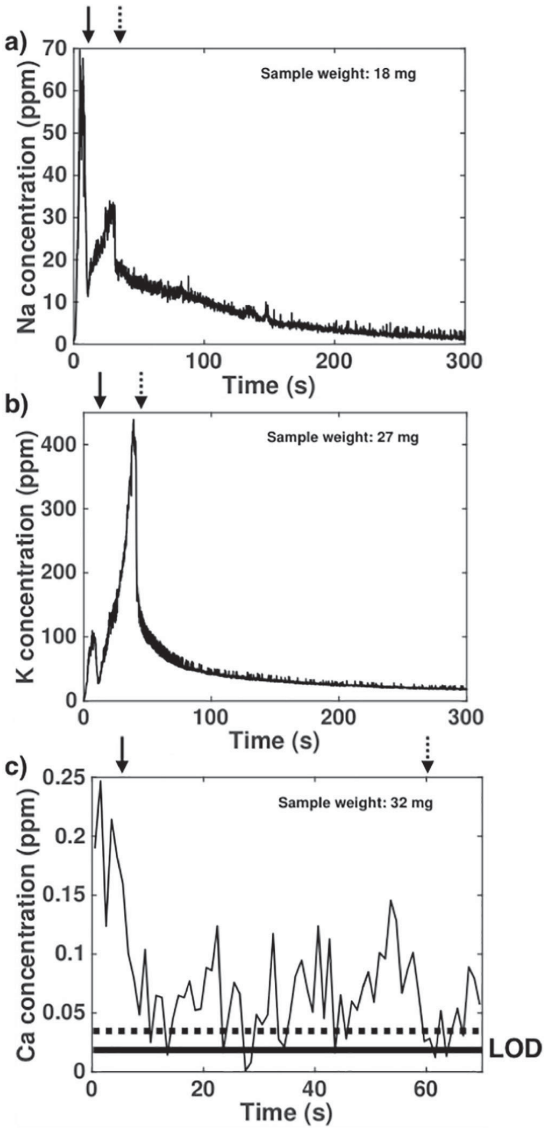

Fig. 9. Temporal release of a) Na, b) K and c) Ca during thermal conversion of poplar with equivalence ratio of 0.79. Time-traces are measured using MW-LIBS and the spectral fitting method to extrapolate the calibration to high concentrations. The time trace of Ca release is averaged over 20 shots, i.e. 2 s, and cut to cover only the devolatilization and char burning to show the release during devoaltilization. The solid arrow marks the end of the devolatilization phase and the dashed arrow marks the end of char burning phase. Solid line in c) depicts the LOD for Ca measurement and the dashed line shows the measurement uncertainty at LOD.

in the previous measurements done for wooden samples [7,10,22]. During devolatilization Na and K are released mostly as alkali chlorides and, as the conversion proceeds, the char associated alkaline atoms are released increasingly as free atoms and hydroxides increasing the total release towards the end of the char burning phase [7,23]. K is showing significantly higher release during the conversion as expected based on the fuel analysis. The strong release during char burning is most likely due to the stoichiometric excess of K and Na to Cl that leaves most of the alkaline to the char after dechlorination during devolatilization.

The release patterns recorded during thermal conversion of poplar shows the potential and applicability of the proposed measurement method for combustion research. The calibration at high concentrations enables measurement targets to be extended to high volatile content fuels while application of MW-LIBS and its improved LODs allows the temporal measurement of trace elements. Hence, the broad dynamic range of the measurement enables more complete analysis of elemental release rates in combustion processes.

4. Conclusions

Novel burner seeding method is presented to achieve broad LIBS calibration range for alkali measurement in combustion flame. The seeding method showed great potential for a linear from low to high concentration seeding limited only by the performance of the nebulizer used to create the seed reservoir. The performance and dynamic range is further improved by adding microwave assistance to the LIBS measurement being the first time when NFA injected MW-LIBS is demonstrated for gas phase measurements. The microwave assistance improved the LODs of the targe elements up to 60-fold. The LOD's for Na, K, and Ca were 10 ppb, 19 ppb and 16 ppb, respectively. The trace element detection is demonstrated with Ca measurement during the biomass conversion. The calibration issues rising from self-absorption were diminished with computational correction that enabled linear calibration to high concentration conditions improving the method's analytical sensitivity and reliability for the alkali release measurements. The proposed method enables temporal alkali release measurements form wide range of biomass samples and therefore provides an important tool for combustion studies. The presented MW-LIBS method enables sensitive elemental analysis of gases also in different areas of industry and science.

Acknowledgements

This work has been partly carried out within CLIFF (2014-2017) as part of the activities of Tampere University of Technology. Other research partners are VTT Technical Research Centre of Finland Ltd., Lappeenranta University of Technology, Aalto University and Tampere University of Technology. Support from the National Technology Agency of Finland (Tekes), Andritz Oy, Valmet Technologies Oy, Amec Foster Wheeler Energia, UPM-Kymmene Oyj, Clyde Bergemann GmbH, International Paper Inc., and Top Analytica Oy Ab is gratefully acknowledged. Dr. Nikolai DeMartini is gratefully acknowledged for providing the samples. J. V. would also like to acknowledge the support by TUT Graduate school.

References

[1] H.P. Nielsen, F.J. Frandsen, K. Dam-Johansen, L.L. Baxter, The implications of chlorine-associated corrosion on the operation of biomass-fired boilers, Prog. Energy Combust. Sci. 26 (2000) 283–298.
[2] S. Enestam, D. Bankiewicz, J. Tuiremo, K. Mäkelä, M. Hupa, Are NaCl and KCl equally corrosive on superheater materials of steam boilers? Fuel 104 (2013) 294–306.
[3] P. Monkhouse, On-line spectroscopic and spectrometric methods for the determination of metal species in industrial processes, Prog. Energy Combust. Sci. 37 (2011) 125–171.
[4] N.H. Bings, A. Bogaerts, J.A. Broekaert, Atomic spectroscopy, Anal. Chem. 78 (2006) 3917–3946.

[5] C. Forsberg, M. Broström, R. Backman, E. Edvardsson, S. Badiei, M. Berg, H. Kassman, Principle, calibration, and application of the in situ alkali chloride monitor, Rev. Sci. Instrum. 80 (2009) 023104.
[6] Z. Qu, E. Steinvall, R. Ghorbani, F. Schmidt, Tunable diode laser atomic absorption spectroscopy for detection of potassium under optically thick conditions, Anal. Chem. 88 (2016) 3754–3760.
[7] T. Sorvajärvi, N. Demartini, J. Rossi, J. Toivonen, In situ measurement technique for simultaneous detection of K, KCl, and KOH vapors released during combustion of solid biomass fuel in a single particle reactor, Appl. Spectrosc. 68 (2014) 179–184.
[8] T. Leffler, C. Brackmann, A. Ehn, B. Kaldvee, M. Aldén, M. Berg, J. Bood, Range-resolved detection of potassium chloride using picosecond differential absorption light detection and ranging, Appl. Opt. 54 (2015) 1058–1064.
[9] M.P. Glazer, N.A. Khan, W. de Jong, H. Splithoff, H. Schürmann, P. Monkhouse, Alkali metals in circulating fluidized bed combustion of biomass and coal: measurements and chemical equilibrium analysis, Energy Fuel 19 (2005) 1889–1897.
[10] L.-J. Hsu, Z.T. Alwahabi, G.J. Nathan, Y. Li, Z.S. Li, M. Aldén, Sodium and potassium released from burning particles of brown coal and pine wood in a laminar premixed methane flame using quantitative laser-induced breakdown spectroscopy, Appl. Spectrosc. 65 (2011) 684–691.
[11] D.W. Hahn, N. Omenetto, Laser-induced breakdown spectroscopy (LIBS), part II: review of instrumental and methodological approaches to material analysis and applications to different fields, Appl. Spectrosc. 66 (2012) 347–419.
[12] Y. Zhang, X.L. Zhang, W.B. Jia, Q. Shan, Y.S. Ling, D.Q. Hei, C. Da, Online X-ray fluorescence (XRF) analysis of heavy metals in pulverized coal on a conveyor belt, Appl. Spectrosc. 70 (2016) 272–278.
[13] A. Michalakou, P. Stavropoulos, S. Couris, Laser-induced breakdown spectroscopy in reactive flows of hydrocarbon-air mixtures, Appl. Phys. Lett. 92 (2008) 081501.
[14] J. Kiefer, J.W. Tröger, Z.S. Li, M. Aldén, Laser-induced plasma in methane and dimethyl ether for flame ignition and combustion diagnostics, Appl. Phys. B Lasers Opt. 103 (2011) 229–236.
[15] A.E. Majd, A.S. Arabanian, R. Massudi, M. Nazeri, Spatially resolved laser-induced breakdown spectroscopy in methane—air diffusion flames, Appl. Spectrosc. 65 (2011) 36–42.
[16] M.S. Mansour, H. Imam, K.A. Elsayed, W. Abbass, Local equivalence ratio measurements in turbulent partially premixed flames using laser-induced breakdown spectroscopy, Spectrochim. Acta. Part B. 64 (2009) 1079–1084.
[17] F. Ferioli, P.V. Puzinauskas, S.G. Buckley, Laser-induced breakdown spectroscopy for on-line engine equivalence ratio measurements, Appl. Spectrosc. 57 (2003) 1183–1189.
[18] F. Ferioli, S.G. Buckley, P.V. Puzinauskas, Real-time measurement of equivalence ratio using laser-induced breakdown spectroscopy, Int. J. Engine Res. 7 (2006) 447–457.
[19] T.-W. Lee, N. Hegde, Laser-induced breakdown spectroscopy for in situ diagnostics of combustion parameters including temperature, Combust. Flame 142 (2005) 314–316.
[20] A. Molina, P. Walsh, C. Shaddix, S. Sickafoose, L. Blevins, Laser-induced breakdown spectroscopy of alkali metals in high-temperature gas, Appl. Opt. 45 (2006) 4411–4423.
[21] Y. He, J. Zhu, B. Li, Z. Wang, Z. Li, M. Aldén, G. Cen, In-situ measurement of sodium and potassium release during oxy-fuel combustion of lignite using laser-induced breakdown spectroscopy: effects of O2 and CO2 concentration, Energy Fuel 27 (2013) 1123–1130.
[22] Z. Zhang, Q. Song, Z.T. Alwahabi, Q. Yao, G.J. Nathan, Temporal release of potassium from pinewood particles during combustion, Combust. Flame 162 (2015) 496–505.
[23] H. Fatehi, Y. He, Z. Wang, Z.S. Li, X.S. Bai, M. Aldén, K.F. Cen, LIBS measurements and numerical studies of potassium release during biomass gasification, P. Combust. Inst. 35 (2015) 2389–2396.
[24] B. le Drogoff, J. Margot, M. Chaker, M. Sabsabi, O. Barthélemy, T.W. Johnson, S. Laville, F. Vidal, Y. von Kaenel, Temporal characterization of femtosecond laser pulses induced plasma for spectrochemical analysis of aluminum alloys, Spectrochim. Acta. Part B 56 (2001) 987–1002.
[25] J. Viljanen, Z. Sun, Z.T. Alwahabi, Microwave assisted laser-induced breakdown spectroscopy at ambient conditions, Spectrochim. Acta. Part B 118 (2016) 29–36.
[26] T. Sorvajärvi, J. Toivonen, Principles and calibration of collinear photofragmentation and atomic absorption spectroscopy, Appl. Phys. B Lasers Opt. 115 (2014) 533–539.
[27] S.J. Chen, A. Iqbal, M. Wall, C. Fumeaux, Z.T. Alwahabi, Design and application of near-field applicators for efficient microwave-assisted laser-induced breakdown spectroscopy, J. Anal. Atom. Spectrom. 32 (2017) 1508–1518.
[28] M. Wall, Z. Sun, Z.T. Alwahabi, Quantitative detection of metallic traces in water-based liquids by microwave-assisted laser-induced breakdown spectroscopy, Opt. Express 24 (2016) 1507–1517.
[29] M.A. Gigosos, M.Á. Gonzáles, V. Cardeñoso, Computer simulated Balmer-alpha,-beta and-gamma Stark line profiles for non-equilibrium plasmas diagnostics, Spectrochim. Acta. Part B. 58 (2003) 1489–1504.
[30] A. Kramida, Y. Ralchenko, J. Reader, NIST ASD Team, NIST Atomic Spectra Database (ver. 5.5.6), [Online]. Available https://physics.nist.gov/asd [2018, April 23] National Institute of Standards and Technology, Gaithersburg, MD, 2018.
[31] A. Pettersson, M. Zevenhoven, B.M. Steenari, L.E. Åmand, Application of chemical fractionation methods for characterisation of biofuels, waste derived fuels and CFB co-combustion fly ashes, Fuel 87 (2008) 3183–3193.
[32] S.V. Vassilev, D. Baxter, L.K. Andersen, C.G. Vassileva, An overview of the composition and application of biomass ash. Part 1. Phase–mineral and chemical composition and classification, Fuel 105 (2013) 40–76.